

**TECHNICAL
TRANSACTIONS**

**CZASOPISMO
TECHNICZNE**

**ENVIRONMENT
ENGINEERING**

ŚRODOWISKO

**ISSUE
1-Ś (13)**

**ZESZYT
1-Ś (13)**

**YEAR
2013 (110)**

**ROK
2013 (110)**



**WYDAWNICTWO
POLITECHNIKI
KRAKOWSKIEJ**

TECHNICAL TRANSACTIONS

ENVIRONMENT
ENGINEERING

ISSUE 1-Ś (13)
YEAR 2013 (110)

CZASOPISMO TECHNICZNE

ŚRODOWISKO

ZESZYT 1-Ś (13)
ROK 2013 (110)

Chairman of the Cracow
University of Technology Press
Editorial Board

Jan Kazior

Przewodniczący Kolegium
Redakcyjnego Wydawnictwa
Politechniki Krakowskiej

Chairman of the Editorial Board

Józef Gawlik

Przewodniczący Kolegium
Redakcyjnego Wydawnictw
Naukowych

Scientific Council

Jan Błachut
Tadeusz Burczyński
Leszek Demkowicz
Joseph El Hayek
Zbigniew Florjańczyk
Józef Gawlik
Marian Giżejowski
Sławomir Gzell
Allan N. Hayhurst
Maria Kuśnierova
Krzysztof Magnucki
Herbert Mang
Arthur E. McGarity
Antonio Monestiroli
Günter Wozny
Roman Zarzycki

Rada Naukowa

Environment Series Editor

Stanisław Kandefer

Redaktor Serii Środowisko

Section Editor

Dorota Sapek

Sekretarz Sekcji

Typesetting

Anna Basista

Skład i łamanie

Native Speaker

Tim Churcher

Weryfikacja językowa

Cover Design

Michał Graffstein

Projekt okładki

Pierwotną wersją każdego Czasopisma Technicznego jest wersja on-line
www.czasopismotechniczne.pl www.technicaltransactions.com

Technical Transactions 1-Ś/2014

Executive Editor:

Andrzej Truty, Cracow University of Technology, Poland

Reviewers:

Stéphane Commend, PhD Ecole Polytechnique Federale de Lausanne, GeoMod ingénieurs conseils SA, Switzerland

Jan Gaszyński, Cracow University of Technology, Poland

Tomisław Gołębiowski, Cracow University of Technology, Poland

Kazimierz Gwizdała, Gdansk University of Technology, Poland

Mihail Lvovich Holmyanskiy, NIIOSP, Russia

Robert Jankowski, Gdansk University of Technology, Poland

Krzysztof Książczyński, Cracow University of Technology, Poland

Mieczysław Kuczma, Poznan University of Technology, Poland

Lumir Miča, Masaryk University, Czech Republic

Vladimir Paramonov, St. Petersburg State University, Russia

Stanisław Pietruszczak, Mc Master University Hamilton, Canada

Marianna Polak, University of Waterloo, Canada

Jerzy Sękowski, Silesian University of Technology, Poland

Vladimir Ulitsky, St. Petersburg State University, Russia

Aleksander Urbański, Cracow University of Technology, Poland

Bogumił Wrana, Cracow University of Technology, Poland

Thomas Zimmermann, Ecole Polytechnique Federale de Lausanne, Switzerland

JAROSŁAW CHEŁMECKI, ARKADIUSZ KWIECIEŃ, BOGUSŁAW ZAJĄC*

THE INERTANCE FUNCTION IN DYNAMIC DIAGNOSIS OF UNDAMAGED AND DAMAGED STRUCTURES

FUNKCJA INERTANCJI W DIAGNOSTYCE KONSTRUKCJI NIEUSZKODZONYCH I USZKODZONYCH

Abstract

The paper introduces basics of a dynamic diagnostic method using the inertance function, in which analysis results are derived from acquisition data obtained from a modal hammer and accelerometers during dynamic testing. The presented examples show the applicability of the method for obtaining conclusions from diagnostic analysis. The proposed method can be used for the analysis of the dynamic response of civil engineering structures and soil.

Keywords: dynamic testing, non-destructive testing, inertance function

Streszczenie

W artykule przedstawione zostało zastosowanie funkcji inetrancji, jako metody analizy wyników pomiarów dynamicznych uzyskanych z młotka modalnego oraz akcelerometrów. Prezentowane przykłady pokazują możliwość zastosowania metody w celu uzyskania wniosków z analizy diagnostycznej. Proponowana metoda może być użyteczna do określania odpowiedzi dynamicznej konstrukcji budowlanych i gruntów.

Słowa kluczowe: badania dynamiczne, badania nieniszczące, funkcja inertancji

* M.Sc. Jarosław Chelmecki, Ph.D. Arkadiusz Kwiecień, Ph.D. Bogusław Zajęc, Institute of Structural Mechanics, Faculty of Civil Engineering, Cracow University of Technology.

1. Introduction

Non-Destructive Testing (NDT) has become a widely developing branch of science in recent decades. These methods allow diagnosing structures and especially for the detection of structural damages. The development of NDT tests in engineering practice has been observed in recent years. The most popular methods are: Flat-Jack tests, Impact Echo, Tomography and methods based on modal analysis [1, 8, 9]. These methods are not fully compatible with each other [10]. These issues are the subject of intense study by the various international teams (e.g. RILEM Committees: TC 216-SAM, TC MCM), and they were presented in many publications [11, 12]. In addition to these methods, a method of dynamic analysis using the inertance function has been developed. It is based on recorded impulse signals of force and acceleration responses in the frequency domain.

2. Inertance function

An inertance function is a special case of a transfer function (1). It is defined in the frequency domain and is expressed by the ratio of the output signal (acceleration response of the structure) to the input signal (impulse excitation with modal hammer) and given by (2). The use of this function is convenient when an acceleration response of structure is measured. Structural response can be also expressed by the flexibility function (with displacement response of a structure) or by the admittance function (with velocity response of a structure).

$$\frac{A_{OUT}}{A_{IN}} = |H(\omega)| \quad (1)$$

$$|I(\omega)| = \frac{|\ddot{X}(\omega)|}{|F(\omega)|} = \frac{1}{|M(\omega)|} \quad (2)$$

$$|F'(\omega)| = \frac{|\ddot{X}(\omega)|}{|I(\omega)|} = |\ddot{X}(\omega)| \cdot |M(\omega)| \quad (3)$$

where:

- $|H(\omega)|$ – transfer function, ratio between output and input signals (frequency domain),
- $|\ddot{X}(\omega)|$ – acceleration frequency characteristic (FFT) of the tested structure,
- $|F(\omega)|$ – excitation force frequency characteristic (FFT) of the modal hammer,
- $|I(\omega)|$ – real inertance frequency characteristic of the tested structure,
- $|F'(\omega)|$ – inertial force frequency characteristic,
- ω – frequency in [Hz].

In the analysis process, recorded signals in the time domain of the impulse excitation and the acceleration response (Fig. 1) are transformed to the frequency domain by the Fast Fourier Transform (FFT). The force frequency characteristics $|F(\omega)|$ and the acceleration frequency characteristics $|\ddot{X}(\omega)|$ are presented in Fig. 2a and 2b respectively. These characteristics allow determining the inertance function module, which determines the apparent mass conversion –

from equation (2). The apparent mass $|M(\omega)|$ indicates the value of the structural mass, which is activated during vibrations. This indicator shows the consistency of the tested structure – the higher the value of $|M(\omega)|$ (lower values of $|I(\omega)|$), the higher is consistency, indicating a high level of the elastic (dynamic) response of a structure.

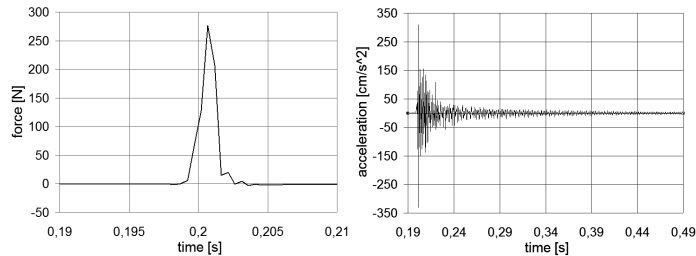


Fig. 1. Impulse force in time domain (a) and acceleration response in time domain (b)

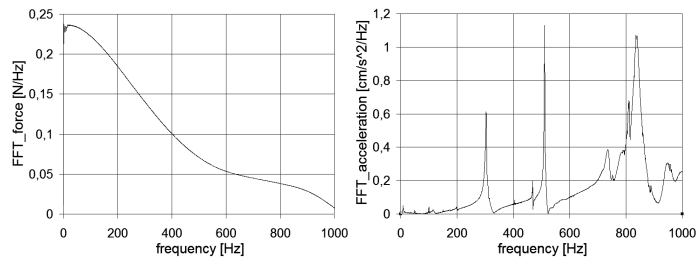


Fig. 2. Impulse force in frequency domain (a) and acceleration response in frequency domain (b)

3. Test on masonry columns

Dynamic tests using the inertance function were performed on masonry columns made of different materials (Fig. 3). One of the tested columns was cut from an existing structure originating from the 20th century (F-9A-2 specimen with cement-lime mortar of low stiffness) and the second one was made in a laboratory (Z-1 specimen with cement mortar of high stiffness). The column with cement-lime mortar was cut from building walls during repair and dismantles. The column with cement mortar was of dimension $250 \times 250 \times 500$ mm³ and consisted of 7 brick layers of the thickness 65 mm, made of the Polish Bonarka bricks (dimension of $65 \times 120 \times 250$ mm³). The columns were tested in a compression and the dynamic response was measured at different load levels.

The considered masonry specimens (fixed between compression plates of an universal testing machine) were excited using a modal hammer. Impulse excitations were generated horizontally in the middle of the tested columns. Dynamic responses of specimens were

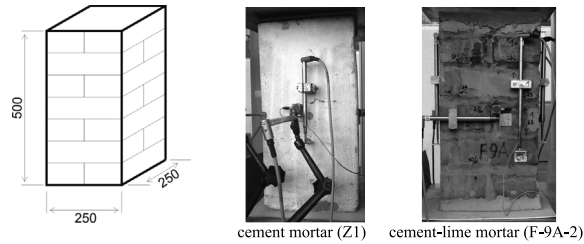


Fig. 3. Tested brick columns

measured in the same direction using two accelerometers. The first one was fixed to the column in the middle of the surface, opposite to the surface excited by the hammer – A1. The second one was used for an additional signal control – A2 (Fig. 4). Compression force was executed on the columns using the monotonic static load generated by the universal testing machine.

The excitation force was realized using the PCB 086D50 modal hammer and the acceleration response was measured using the 356B18 PCB accelerometers during the tests described below. All signals were recorded using the LMS SCADAS MOBILE system with the sample rate of 4096 samples/sec.

It can be observed at least two main resonant frequency bands (lower and higher), visible during analysis of the dynamic response of the samples F9A-2 and Z-1 before the destruction (Fig. 5). The lower frequency band was located in the frequency range of 700–850 Hz. The comparison of this band for both masonry columns indicates that the lower mortar strength, the lower is the response frequency.

It can be concluded from the relationships for the specimen F9A-2 (of lower stiffness) presented in Fig. 5, that the increase of the load level results in the change of the inertance, (manifested by the shift of the frequency to the higher values) and in the slight decrease of the inertance value (indicating the increase of the column consistency). Simultaneously for the Z-1 (of higher stiffness), the increase of the load does not affect significantly on the increase of the frequency, but results in the higher inertance value (Fig. 5). This may indicate on the change of the vibrating masses and on the cracks develop in the tested masonry structure.

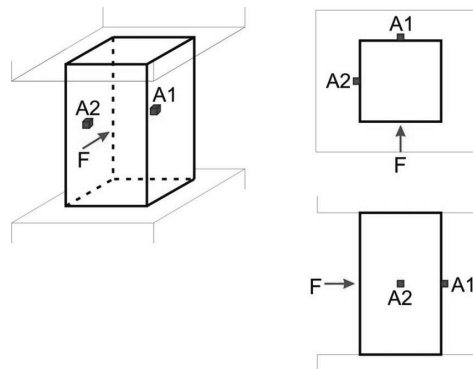


Fig. 4. Location of the impulse force excitation and of accelerometers

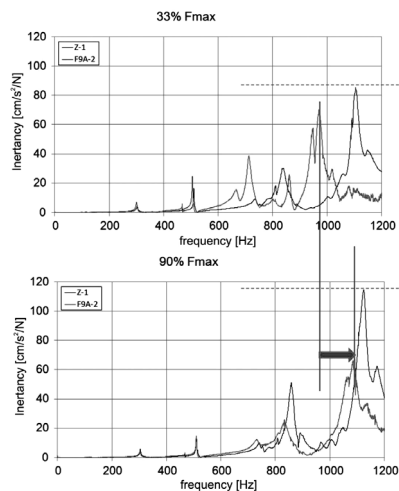


Fig. 5. Inertance functions calculated for the tested masonry columns, presented for two load levels

The sudden change of the inertance characteristic in the lower frequency band is observed just after failure, when the dynamic response of the samples F9A-2 and Z-1 in vicinity of destruction (Fig. 6) is analysed. After crossing of the $F_{max}^?$, the decrease in the frequency and the significant increase of the inertance value appear (indicating the decrease of the column compactness). It happens due to significant cracking of the main masonry columns,

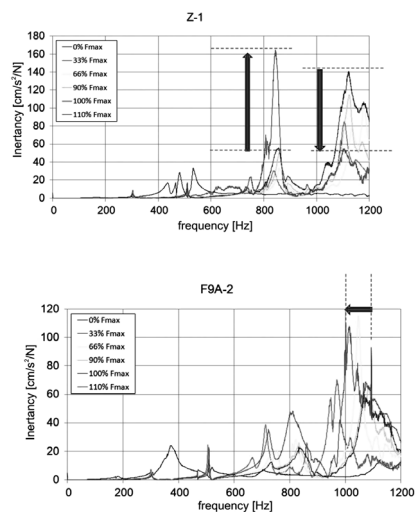


Fig. 6. Change of the inertance function value for the masonry column Z-1 (a) and frequency shift for the masonry column P9A-2 (b)

dividing the specimens into smaller sub-columns (reducing the compactness of the wall). The process of the masonry columns cracking is also visible as the inertance changes in the higher frequency band (Fig. 6), located in the range of 950–1100 Hz. The ongoing process of the structure loosening causes the decrease in the frequency response, but simultaneously brick and mortar particles are again compacted after crushing. It causes the effect of the stress redistribution and the local return to the more consistency of the column materials, visible in the decrease of the inertance value.

The presented results show that failure modes depend on types of the structural materials of the columns. The changes in the destruction process can be observed using the inertance function, but a lot of tests have to be done to validate the presented conclusions.

4. Test of masonry building

Another example of the use of the inertance function in dynamic testing is research on a masonry building. Dynamic tests on the real object destined for demolishing were carried out in Balice. The building made of solid bricks was tested in three phases [5]. Firstly, the undamaged object was investigated (Fig. 7a), next damaged one (Fig. 7b) and finally, repaired one using polymer flexible joints (Fig. 7c).

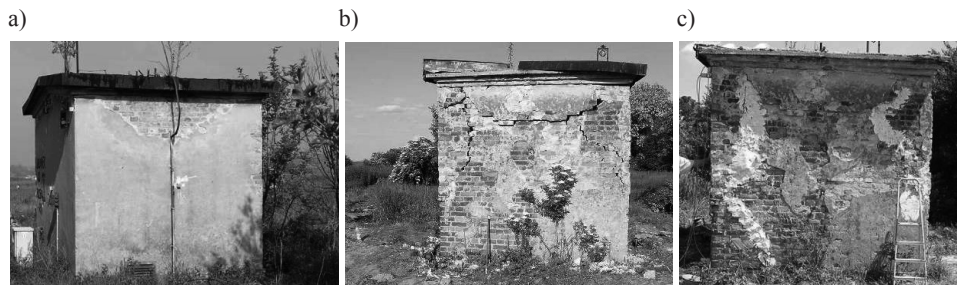


Fig. 7. Tested building in three phases: undamaged (a), damaged (b), repaired (c)

There were installed 17 sensors on the building (Fig. 8), mounted in three directions X, Y and Z. The force was excited using a modal hammer, treated as an input parameter.

During the tests on the building, the excitation force was realized using the PCB 086D50 modal hammer and the acceleration response was measured using the 393B12 PCB accelerometers. All signals were recorded using the ESAM TRAVELLER PLUS system with the sample rate of 4096 samples/sec.

The excitation was generated at the upper corner of the building in three phases. There were determined the inertance functions on the basis of the recorded signals: the force excitation (1y) and the acceleration response (8y). Looking at the obtained results (Fig. 9), it can be seen that the damage to the structure caused the significant increase of the inertance value with the minimal decrease of the frequency. An analogy to the previously discussed masonry columns can be observed. Similarly in both cases, the deterioration of the objects affected the inertance values and the characteristic frequencies. In Fig. 9, the red arrow indicates this

effect. On the other hand, the repair of the building using polymer flexible joints affected the change of the inertance function in the opposite direction (represented by the green arrow).

The presented results indicate that the inertance function can be used as the NDT tool in diagnosis of real structures, but more tests on real structures have to be done to validate the presented method.

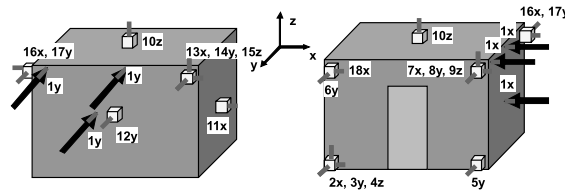


Fig. 8. Sensors installed on the building [5]

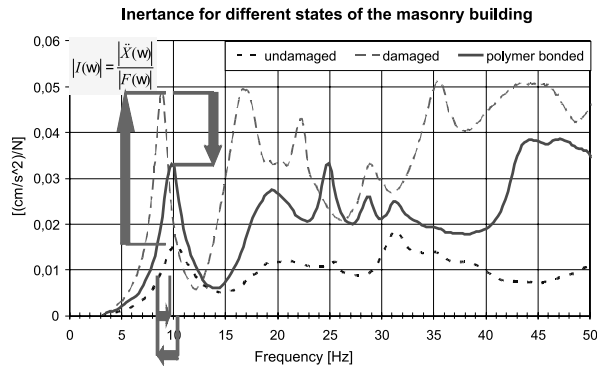


Fig. 9. Inertance of the investigated building [5]

5. Test laboratory floor

The third example of the diagnostic method using the inertance function is a test performed on the laboratory floor [6]. The floor was designed with fields joined by dilatations protecting sensitive laboratory equipments against vibrations. The equipments had to be isolated from any external vibrations, particularly from the self-propelled probe CPT, passing across the lab floor. The designed dilatation was not performed properly, as the result of manufacturing defects. In order to detect these defects and effectiveness of the repair, the inertance function was used and analyzed for three stages of the floor work: without dilatation, with dilatation and after constructing of polymer flexible joint inside the dilatation (Fig. 10).

To perform dynamic diagnostic, the modal hammer was used to generate the excitation force, simultaneously working as the force sensor. Sensors were placed on both sides of the dilatation (Fig. 11) during the tests, whereas the excitation was performed on one side of the dilatation. The measured signals were recorded and the inertance function was calculated on their basis.

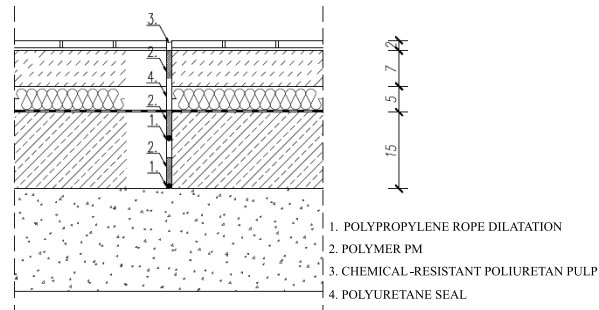


Fig. 10. Construction of the floor with the polymer flexible joint

During tests on the floor, the excitation force was realized using the PCB 086D50 modal hammer and the acceleration response was measured using the 356B18 PCB accelerometers. All signals were recorded using the LMS SCADAS MOBILE system with the sample rate of 4096 samples/sec.

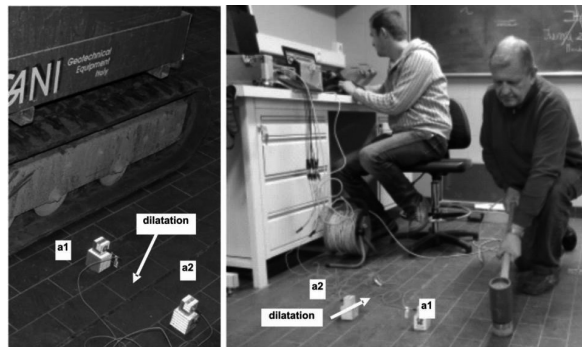


Fig. 11. Sensors installed on the laboratory floor [6]

As the result, the change of the inertance function values can be observed in Fig. 12. Analysis of the results at the first stage showed that the levels of vibration on both sides of the dilatation are similar. A small reduction of the inertance characteristic in the point “a2” (in comparison to the point “a1”) is observed due to different distances between the sensors and the source of vibration. The execution of the empty dilatation resulted in the increase of the vibration level in the point “a1” and in the significant reduction in the point “a2” (at the second stage). The implementation of the flexible polymer joint in the dilatation space retained the low level of vibrations in the point “a2”, simultaneously reducing the vibrations in the point “a1”. Small shifts of the frequency bands were also observed.

The observed changes of the inertance functions allowed for the NDT diagnosis of the problems resulted from the improper construction of the floor and for efficiency checking of the applied repair solutions.

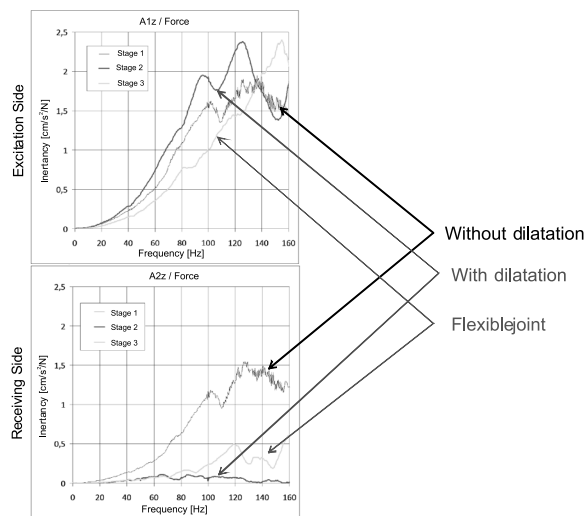


Fig. 11. Changes of the inertance functions for three diagnostic stages

6. Conclusions

the proposed inertance function could be especially useful in the real applications as the non-destructive testing method (NDT) of civil engineering structures, because it allow monitoring changes of the structural behaviour for the various states of work. Using this method, somebody is able to detect the appearance of invisible structural damages (cracks and micro-cracks) and their influence on the structural behavior. Characteristic of the inertance depends on the degree of the structural material effort and of the technical state of the tested object. The proposed diagnostic method is complementary to the previously used NDT methods. Further works are planned on developing of the NDT methods using the inertance function to the demonstrated a practical aspect of it.

References

- [1] Kwiecień A., Chelmecki J., Matysek P., *Non-destructive test of brick masonry columns using change in frequency and inertance response*, Structural Analysis of Historical Constructions SAHC'2012, DWE, Wrocław 2012.
- [2] Tomaževič M., *Research for seismic redesign of historic masonry buildings*, 4th International Seminar on Structural Analysis of Historical Constructions, Padwa 2004.
- [3] Kwiecień A., Zajac B., *Dynamic response of the cracked masonry building repaired with the Flexible Joint Method – an innovative earthquake protection*, 7th International Conference of EASD EURODDYN'2008, Southampton 2008.
- [4] Ramos L.F., Lourenço P.B., DeRoeck G., Campos-Costa A., *Damage identification in masonry structures with vibration measurements*, Structural Analysis of Historic Construction – D' Ayala & Fodde (eds.) Taylor & Francis Group, London 2008.

- [5] Kwiecień A., *Flexible polymer adhesives versus stiff mineral and epoxy adhesives tested dynamically on masonry columns strengthened using of bonded GFRP mesh*, Proceedings of the 8th International Conference on Structural Dynamics, Eurodyn'2011, Leuven 2011.
- [6] Kwiecień A., Zając B., Chelmecki J., Czado B., *Zastosowanie złączy podatnych w dylatacjach posadzek betonowych*, XXV Konferencja Naukowo-Techniczna Awaryjne Budowlane, Międzyzdroje 2013.
- [7] PN-85/B-02170, *Ocena szkodliwości drgań przekazywanych przez podłogę na budynki*.
- [8] Sansalone M.J., Streett W.B., *Impact-echo. Nondestructive evaluation of concrete and masonry*, Ithaca, NY: Bullbrier Press, 1997, 339.
- [9] Binda L., Tiraboschi C.: *Flat-Jack Test: A slightly destructive technique for the diagnosis of brick and stone masonry structures*. International Journal for Restoration of Buildings and Monuments 5.5 (1999): 449-472.
- [10] Maierhofer C., Ziebolz A., Köpp C., (Onsiteformasonry-a European Research Project: *On-site investigation techniques for the structural evaluation of historic masonry*, In Proc. Int. Symp. on Non-Destructive Testing in Civil Engineering. Berlin 2003.
- [11] Binda L., Saisi A., *Knowledge of the building, on site investigation and connected problems*, Eurocode 2008 Perspectives from the Italian Standpoint, Workshop, © 2009 Doppiavoce, Napoli, Italy 213-224.
- [12] Polyzos D., *Dependence of AE parameters on the propagation distance*, Progress in acoustic emission. Proceedings of the 20th international acoustic emission symposium, Japanese society for non-destructive inspection (JSNDI), Kumamoto, Japan. 2010.

MICHAŁ GRODECKI*

INFLUENCE OF A SURCHARGE LINE LOAD ON CANTILEVER SHEET PILE WALL BEHAVIOR

WPŁYW OBCIĄŻEŃ LINIOWYCH NA PRACĘ ŚCIANKI SZCZELNEJ NIEKOTWIONEJ

Abstract

The results of a parametric study of a surcharge line load influence on sheet pile wall behavior are presented in this paper. Results obtained from numerical analysis and classic engineering methods are compared.

Keywords: excavation, sheet pile wall, FEM, line load

Streszczenie

W artykule przedstawiono rezultaty studium parametrycznego wpływu obciążenia liniowego naziomu na pracę ścianki szczelnej niekotwionej stanowiącej zabezpieczenie wykopu. Porównano wyniki uzyskane za pomocą analizy numerycznej i klasycznymi metodami inżynierskimi.

Słowa kluczowe: wykop, ścianka szczelna, MES, obciążenie liniowe

* Ph.D. Michał Grodecki, Department of Geotechnics, Faculty of Environmental Engineering, Cracow University of Technology.

Symbols

ϕ	– internal friction angle [deg]
γ	– soil bulk density [kN/m ³]
c	– cohesion [kPa]
h	– excavation depth [m]
H	– total length of wall [m]
L	– distance from wall to line load [m]
SF	– stability factor [–]
q	– soil pressure [kPa]
Q	– surcharge line load [kN/m]
UX	– horizontal displacement [m]

1. Introduction

The main subject of this investigation is an excavation with depth h , supported by a cantilever sheet pile wall (with total height H), and with a line load Q on the surcharge parallel to the wall (with distance L from the wall). This is of course a simplification of a real situation, where rather strip load exist. But if the load dimension perpendicular to the wall is narrow (in comparison with excavation depth h), such an approach could be used.

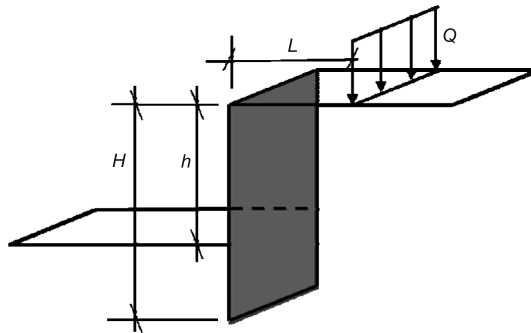


Fig. 1. Analyzed object

The main goal of this paper is to show the surcharge line load influence on sheet pile wall behavior (stability, bending moment and displacements).

Such an object can be analyzed in different ways. Three approaches can be used: ultimate soil pressure theory, elastic soil pressure theory and numerical analysis (based on elasto – plastic soil model).

1.1. Ultimate soil pressure caused by surcharge line load

Solution of the ultimate soil pressure caused by surcharge line load problem one can find for example in Polish code PN-83/B-03010 [3]. It shows that additional pressure caused by

surcharge line load starts acting with the value of q_{int} at depth $L \cdot \text{tg}(\phi)$ under the surcharge while the sum of this pressure and soil active pressure is uniform, as shown in Fig. 2.

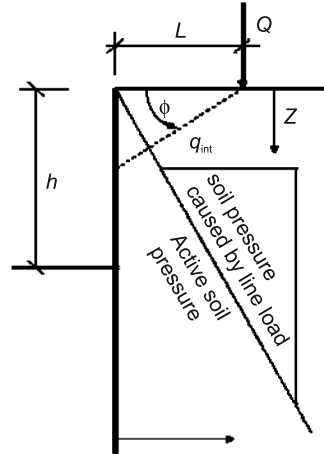


Fig. 2. Ultimate soil pressure caused by surcharge line load

Value of q_{int} can be calculated from equation:

$$q_{int} = \sqrt{2\gamma Q K_a^{1.5}} \quad (1)$$

where:

$$K_a = \text{tg}^2 \left(45^\circ - \frac{\phi}{2} \right) \quad (2)$$

Distribution of such additional soil pressure depends on soil parameters (especially on internal friction angle). One can see that soil pressure distribution in this case is discontinuous, which raises question of whether or not it is a good representation of the real soil behavior.

1.2. Elastic (intermediate) soil pressure caused by surcharge line load

Solution of the elastic (intermediate) soil pressure caused by surcharge line load problem one can find in Polish code PN-83/B-03010 or in US Guidelines EM 1110-2-2504 [1].

It shows that additional pressure caused by the surcharge line load is acting on the whole wall and does not depend on soil properties. Values of this pressure at depth z under the surcharge could be calculated from equations:

$$q = \frac{1.27 \cdot Q \cdot L^2 \cdot z}{(L^2 + z^2)^2} \quad \text{for } L > 0.4 h \quad (3)$$

$$q = \frac{0.203 \cdot Q \cdot h^2 \cdot z}{(0.16h^2 + z^2)^2} \quad \text{for } L < 0.4 h \quad (4)$$

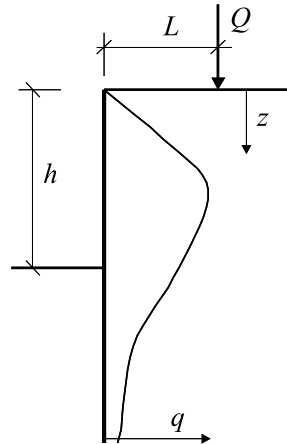


Fig. 3. Elastic (intermediate) soil pressure caused by surcharge line load

1.3. Numerical simulation with stage construction algorithm

Numerical simulation with a stage construction algorithm can also be used to deal with aforementioned problem. Two different stage construction schemes can be taken into account – first with line load added before inserting the wall (simulation of the excavation in the vicinity of existing load), second with line load added after inserting the wall and excavation (simulation of the influence of the added later line load on existing excavation support). In the second approach, an ultimate load analysis can be performed (line load could be increased to obtain loss of stability of the structure). In this case, special attention should be paid to distinguish between two possible failure mechanisms, loss of stability of the excavation support (which is the topic of this paper) or subsoil bearing capacity (like for direct foundation problem, which is out of the scope of this paper).

2. Numerical experiment

The numerical experiment was performed in order to assess the influence of the surcharge line load on sheet pile cantilever wall (acting as excavation support) behavior. Walls with a total height $H = 6$ m supporting excavation with depth $h = 3$ m embedded in soils with different properties were analysed. Soil properties were selected to obtain the stability factor $SF = 1.35$ for situation without surcharge load (which is reasonable margin of stability). In the numerical analysis, the following initial assumptions were used:

- plane strain conditions,
- Coulomb – Mohr elasto – plastic model for soil, with tensile “cut-off” condition (no tension),
- elastic model for the wall,
- contact elements with no friction between the wall and soil,
- stage construction algorithm with partial unloading,
- stability analysis based on c-fi reduction algorithm (described in details in [5]),
- to prevent the construction from failure from subsoil load capacity loss (which is not the topic of this paper) a small area of soil under the line load was modeled as an elastic one.

All numerical simulations were performed with the use of the FEM system ZSoil v 12 (which is described in details in [4–6]). A full description of methodology used can be found

in [2]. Obtained results were compared with results from of simplified methods. Ultimate load in the case of use of simplified methods were identified as load for which moment of soil pressure acting on retained side of the wall (it means moment caused by active soil pressure and additional pressure produced by line load) is equal to the moment acting on dredge side (caused by passive soil pressure).

3. Obtained results

The ultimate load analysis shows that it is possible to calculate ultimate load Q_{\max} of the structure with the use of simplified methods, but with some limitations. The elastic pressure approach yields reasonable results (comparable with those obtained from numerical simulations) if the line load is located closer to the wall then excavation depth. For loads located a larger distance from the wall, this approach leads to underestimating the ultimate load, which is especially visible for walls embedded in soils with small cohesion. The ultimate soil pressure approach can only be used for soils with small cohesion. For soils with high values of cohesion, this approach leads to significant underestimation of the ultimate load.

Relationships between the obtained values of ultimate load and distance L for walls embedded in different soils, obtained with three described before approaches, are presented on the graphs below.

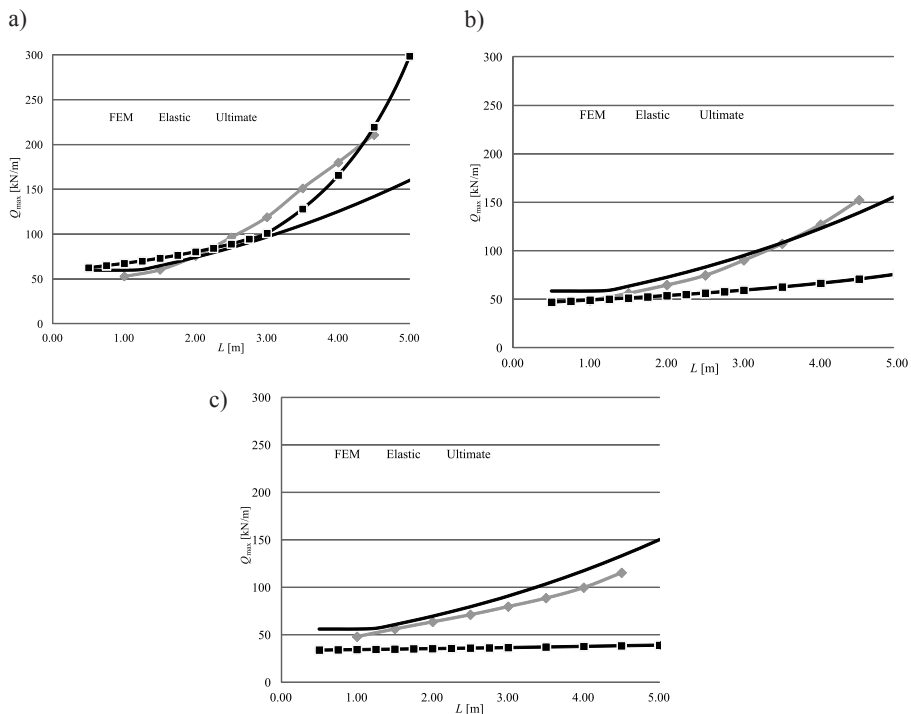


Fig. 4. Ultimate load as a function of line load location, for soils with different strength parameters: a) soil with small cohesion ($c = 4$ kPa, $\phi = 30^\circ$), b) soil with intermediate cohesion ($c = 10$ kPa, $\phi = 20^\circ$), c) soil with high cohesion ($c = 17.5$ kPa, $\phi = 8^\circ$)

Plots of additional soil pressure produced by a line load are presented in graphs below. One can see that a decrease of the soil pressure on the retained side of the wall at the part of the wall under the excavation bottom is obtained in the numerical simulations. It is due to rotational movement of the wall, which reduces soil pressure to the ultimate one. Such an effect is not observed in simplified calculations methods.

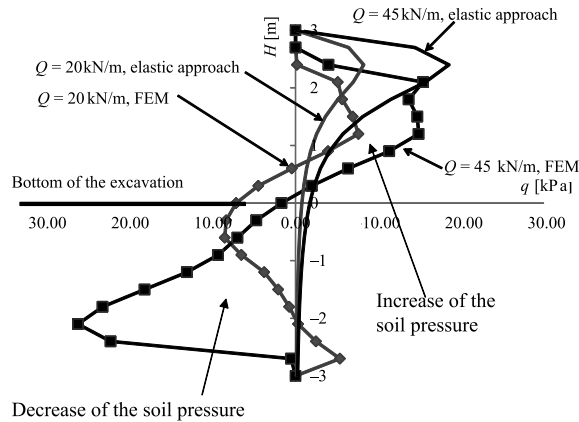


Fig. 5. Additional soil pressure produced by line load – FEM simulations results vs elastic approach

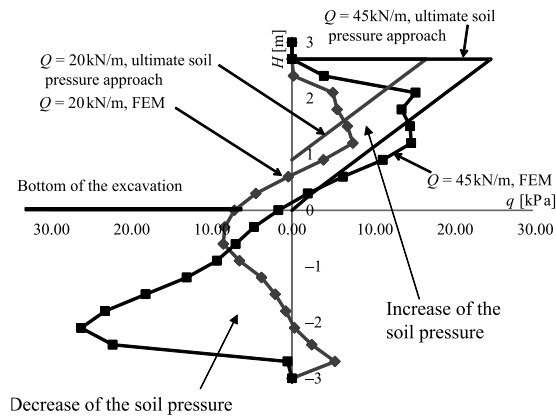
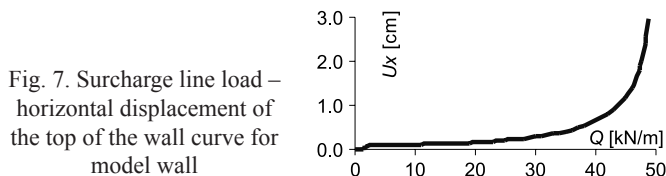


Fig. 6. Additional soil pressure produced by line load – FEM simulations results vs ultimate soil pressure approach

Discrepancies in the obtained additional soil pressure distributions show that simplified approaches could not be used in the bending analysis of the wall. It would result in obtaining an unrealistic distribution of the bending moment.

The staging scheme does not affect the stability of the wall or bending moment. Displacements obtained in the case with load added after excavation are a bit bigger than in the case with load added before wall inserting.

Load – displacements curves obtained in numerical analyses are strongly nonlinear, especially when the line load is close to the ultimate one.



4. Final remarks

The analysis described above shows that simplified approaches can be used for stability analysis of the cantilever wall with some line load on the surcharge, but with some limitations. The elastic approach yields results consistent with those obtained from FEM simulations for non-cohesive soils or for cohesive soils but with limitation to $L < h$. The ultimate soil pressure approach can be used for the stability analysis. but only for soils with small cohesion. Both simplified approaches fail to represent bending behavior because of discrepancies in additional soil pressure distributions.

References

- [1] Design of *sheet* pile walls. Engineer Manual 1110-2-2504, Department of the Army, U.S. Army Corps of Engineers, Washington 1994.
- [2] Grodecki M., Truty A., Urbański A., *Modelowanie numeryczne ścian szczelnych*, Górnictwo i Geoinżynieria, Kwartalnik AGH, Rok 27, zeszyt 3-4, 2003.
- [3] PN-83/B-03010 Ściany oporowe. Obliczenia statyczne i projektowanie.
- [4] Podleś K., Truty A., Urbański A., *Analiza zagadnień geotechnicznych w systemie Z_SOIL*, X Jubileuszowa Konferencja Naukowa „Metody Numeryczne do Projektowania i Analizy Konstrukcji Hydrotechnicznych”, Korbilów 1998, 100-108.
- [5] Truty A., Urbański A., Grodecki M., Podleś K., *Komputerowe modele zagadnień osuwiskowych oraz ich zabezpieczeń*, Zeszyty Naukowo-Techniczne Stowarzyszenia Inżynierów i Techników Komunikacji Rzeczpospolitej Polskiej w Krakowie nr 88 (zeszyt 144), 2009.
- [6] *Z_Soil.PC, Theoretical Manual*, ZACE Services Ltd., Lozanna 2000.

RYSZARDA IWANEJKO*

RISK CALENDAR AS A SUPPLEMENT OF A BASIC RISK ANALYSIS IN A WATER SUPPLY SYSTEM

KALENDARZ RYZYKA JAKO UZUPEŁNIENIE PODSTAWOWYCH ANALIZ USZKADZALNOŚCI SIECI WODOCIĄGOWEJ

Abstract

During the research work, a failure analysis in the water supply systems was performed with respect to different time scale. The results of such analyses provide information on failures' distribution over time, occurrence of the so called 'black series' (i.e. series of days with numerous failures) or days without failures. Therefore, they may be useful in the validation of a number of maintenance schemes and the selection of the optimal time for the necessary maintenance actions and pre-scheduled repairs of the water supply system. They may also be of a substantial practical value for the operator, while preparing the so called risk calendar.

Keywords: water distribution system, system failures

Streszczenie

W artykule przeprowadzono analizy uszkodzeń sieci wodociągowej w odniesieniu do różnych jednostek czasu. Wyniki takich analiz dostarczają informacji o rozkładzie uszkodzeń w czasie, o występowaniu tzw. czarnych serii (czyli kolejnych dób z dużą liczbą uszkodzeń) czy dób bezuszkodzeniowych. Mogą więc być przydatne przy weryfikacji liczby brygad remontowych, przy praktycznym wyborze okresów optymalnych dla przeprowadzania koniecznych prac konserwacyjnych i remontów planowych sieci wodociągowej. Dlatego mogą posłużyć do sporządzenia tzw. kalendarza ryzyka i mieć dla eksploatatora sieci duże znaczenie praktyczne.

Słowa kluczowe: sieć dystrybucji wody, uszkodzenia sieci

* Ph.D. Ryszarda Iwanejko, Institute of Water Supply and Environmental Protection, Faculty of Environmental Engineering, Cracow University of Technology.

1. Introduction

Water supply systems have become the subject of many research works and analyses. They look at them both from the perspective of reliability of function (early seventies of the 20th century) and from the safety and risk perspective (middle 90s). The history of these works is summarized in the paper [1]. Initially, the scope of the reliability analysis of the water supply systems was very limited due to a low development level of the field and a lack of satisfactory failure data. The data was collected for specific municipal services rather than for a broader applicable reliability analysis. However, in recent years, a growing number of water utilities began to appreciate the availability of the 'at source' information during management and planning processes. The utilities apply widely available computer techniques and generate huge databases. The basic measure used to estimate water system conditions is its failure rate λ_0 . This parameter is defined as a number of failures within the water system per time unit and length unit (usually per 1 km and 1 year). In the literature [1, 2] there are values of λ_0 that cannot be exceeded. The range and degree of detail in a contemporary analysis of water system failures depends not only on the scope and the accuracy of the information gathered by the operator, but also on the creativity and knowledge of the analyst. The most common are general analyses, which determine the parameter λ_0 for the entire system, in consecutive years, or just for some particular sections, taking into account their functions (mains, distribution lines, connections) or material (cast iron, steel, PVC, etc.) together with variability analyses. Additionally, the possibility of generation of risk maps came to light [3]. They provide information on the spatial distribution of failures. The final outcome of all activities combines the information on failures that reflect on the actual water system conditions, not only at a particular utility, but also at a nationwide scale [2, 4].

It is known that failures occur in a dynamic way [5] and the process parameters change in time. Therefore, the paper presents mostly results of a water system failure analysis function over time that may be useful while making a risk calendar. The key parameter in this analysis is not a relative failure rate λ_0 , calculated per time and length units, but a number of failures k related to different time units, only (year, month and day). Such analyses, though cannot help to compare failures in different water systems nor to check the limiting criterion λ_0 , may still have a practical meaning for the operators. They may be useful during the validation of a maintenance team size and during the actual selection of the optimal periods for necessary maintenance actions and pre-scheduled repairs of the water system. Particularly important may be the knowledge on: the probability of occurrence of the so-called extreme days (with a large number of failures); probability of occurrence of 'black series' (series of days with a large number of failures); the probability of occurrence of failure-free days. The parameters determined in this paper are empirical. Assuming that an operation mode or climate conditions will not change substantially, a similar pattern of failures may be expected in future.

2. Short characteristic of the system

Further analyses will be conducted for the water distribution system located in one of the cities of Southern Poland. Municipal Water and Sewage Works (MWSW) of this city provides water for over 850 thousand inhabitants. Water is supplied to the consumers through

a complex distribution system. The total length of the system in 2010 was almost 2037 km and consisted of: transit pipes and mains of 350–1200 mm diameter (11% of the total system length in 2010), distribution lines of 325–80 mm diameter (ca. 64%) and household connections of 100–25 mm (ca. 25%). Most of the pipes have been made of steel (ca. 30.4% of all pipes), cast iron (ca. 26%) and plastic (PVC 21.6%, PE 18.6%). The rest of the pipes (ca. 3.4%) are made of asbestos cement or lead. About 15% of pipes have been used for less than 10 years while 18% for 11–20 years; a large number of pipes (67%) has been in operation for at least 20 years, including some that are no less than 50 years old (ca. 7%).

Data obtained from the MWSW of the city provided the grounds for a more detailed analysis [6]. Operational reports, which were used for further research, were collected in a MS-Excel database. In this database, recorded failures were completed with information on the date of repair, the name of the street where the pipe is located, the failures item (pipe, connection, hydrant, gate, etc.), the pipe diameter, the material (cast iron, steel, etc.) and the repair action (replacement, cut, tightening, etc.). It is worth noting that it is the dates of repairs that are noted rather than the dates of the failure occurrence. Recorded water system failures are dealt with as soon as possible – their repair could not be postponed. Breakdowns of the highest priority must be repaired quickly. Those that are less important and of lower priority, even if reported on a day preceding a holiday, could be taken care of after several days, especially when all maintenance teams are occupied. However, in such circumstances repairs may be delegated to third party companies. When delays occurred, the reasons were objective such as e.g. difficult access to the site. There have surely been cases of less important or complex failures being repaired much later after having been reported, but it did not result in water shortages or pose any danger or difficulties for consumers. It can be assumed that the analysis of repaired failures instead of occurrences does not significantly influence the accuracy of the final conclusions related to water supply availability. Therefore, the number of repairs shall hereinafter be considered equal to the number of occurred failures.

The following database analysis is not yet complete through it contains information on failures repaired by the third parties. In the database, in certain records, some information such as the type of materials used or the pipe's diameter are missing. Also some given data are insufficient – e.g. in case of overlapping diameters of distribution lines and household connections (80–100 mm). Additional information should be added on which pipes failed. There are following reasons for missing data:

- 1) failure of fittings,
- 2) failure at connection points (change of a pipe diameter),
- 3) repair involved tightening (sealing),
- 4) data is gathered during failure occurrence i.e. in different weather conditions and with a time pressure. As a result, complete and highly reliable analysis cannot be conducted.

3. Analysis of the number of water system damages in time

In 2006–2011 the number of recorded and repaired failures k was subject to increasingly detailed analysis, relating to years, months or days. However, in the text only the most interesting data, graphs and results have been presented.

3.1. Yearly analyses

Figure 1 shows the changes in the number of failures in particular years. On average, $k = 1354$ failures were repaired per year. In the years 2008 and 2011, the lowest number of failures was recorded, whereas the highest was reported in 2006. Pipes were the most often damaged items (ca. 89.9% of the total number of failures), while damage of gates constituted about 7.4% and hydrants ca. 2.5%. The rest, ca. 0.2%, was described as ‘others’ (drains, hand pump, valve, etc.).

The length of the system itself was growing relatively slowly (20–40 km/year on average – during the analysis, it gained almost 110 km, that is 6% comparing to 2006) and quite comparable to the average failure rate λ_0 (Fig. 1). The average failure rate was $\lambda_0 = 0.7$ [1/km × year] and was never higher than 1 [1/km × year], which is the figure considered as acceptable by western experts [1]. During the last three years, one can notice the decrease of the failure rate λ_0 . Unfortunately, because of the incomplete database it was not possible to analyze the changes in the failure rates of mains distribution lines and household connections separately.

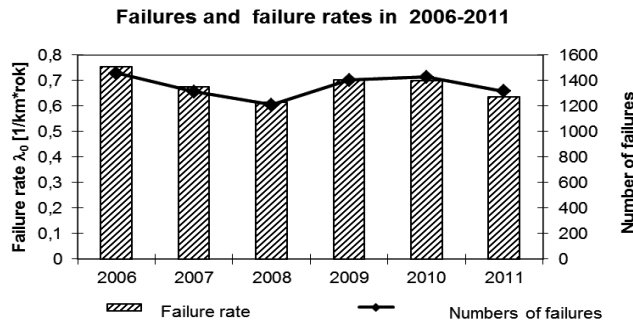


Fig. 1. Failure rates λ_0 and number of failures k in the city water supply system (2006–2011)

3.2. Monthly analyses

It has been observed that the number of failures depends on the month, or more to the point on the seasons. (Fig. 2). As it could have been expected, in winter time (January, December) the number of failures is almost twice as high as in summer. The highest monthly failure rate was observed in January (0.088 [1/km × month]) and December (0.086 [1/km × month]), whereas the lowest was observed in May and June (0.04 [1/km × month]). If the failure rate stays at the same level during the whole year as it does in the winter, it would exceed the acceptable value of $\lambda_0 = 1$ [1/km × year] and according to western standards, the system would be qualified as one that requires renovation.

A question which arises is whether there is a connection between the type of pipe material and the time of year. As it has been mentioned, there is significant information missing in the collected data. For example, in May 2008 in 67.5% cases (50 out of 74 breakdowns) the

material was not indicated, while at the turn of 2009 and 2010 ca. in 43% of cases, there was no information on the construction material. Because of the incomplete maintenance services records, general data analysis is quite difficult, nonetheless, it still may lead to interesting conclusions. When taking into account all the data (Fig. 3a) as well as when excluding incomplete records (no information on the pipe material, Fig. 3b), it may be concluded that cast iron pipe failures were the most common in the winter (up to even 60% of the total failures), whereas in the summer, it was the steel pipe failure (up to 50% of all failures). About 23% of records were ignored because of them being incomplete (from 13.9% to 31.1%, depending on the month), which is a significant part of the database. The analysis was conducted despite the missing information. The case was then analyzed, failures with missing pipe material records were distributed between all materials, proportional to the actual material structure of the system. The results differed only slightly (by few percent) from the results obtained when such failures were ignored. Additionally, a substantial predomination of failures of cast iron pipes in winter and steel pipes in summer was true, in all cases.

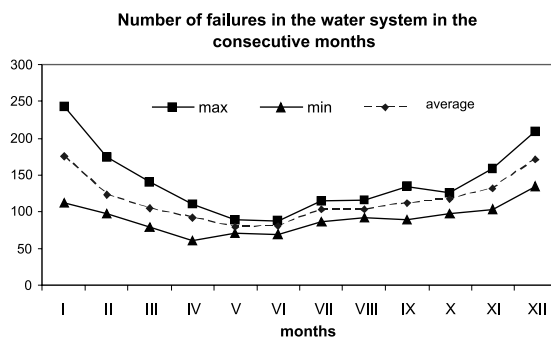


Fig. 2. Number of failures k in the water supply system in consecutive months

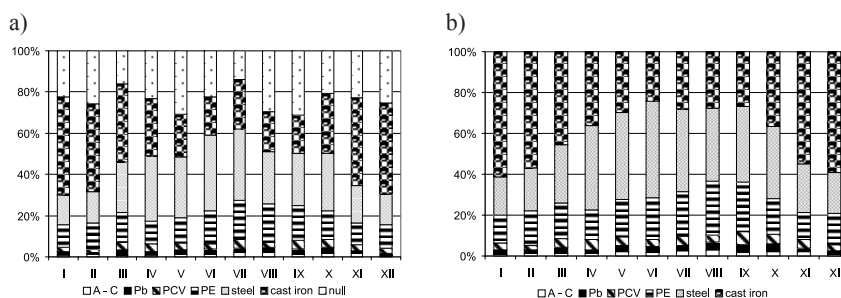


Fig. 3. Failures distribution of in the X water distribution system as a function of the month and pipe material: a) all the data b) incomplete information on the material is ignored

In the data base, a number of cast iron pipe sections have been identified (with a diameter < 100 mm), which broke more often in winter; for instance, one of the sections broke five times in winter while only once in summer. Failures may be caused by shallow pipe placement, severe and snow-less winters and low water velocities at night. Cast iron pipes

showed the highest failure rate λ_0 . Although due to missing information in the database, precise calculations were not possible, some additional research was carried out.

The results for cases where failures with the missing material information have been distributed between all other materials proportionally to the system material structure, are presented in Fig. 4. The values λ_0 determined in subsequent years indicate a decreasing trend for cast iron due to system renovations, replacement of pipes with PVC/PE pipes and seals. On the other hand, failures rates for steel, PE and PVC do not undergo any substantial changes.

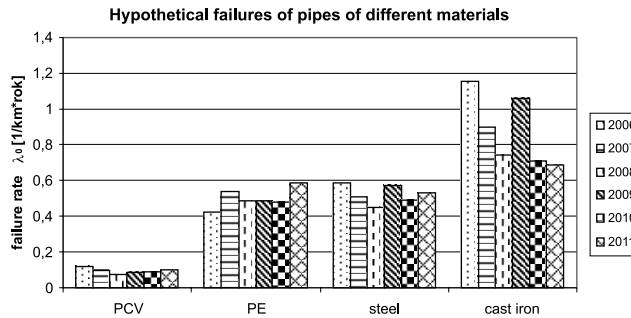


Fig. 4. Failure rates in the water supply systems of different materials – incomplete data distributed proportionally to the material structure of the X system

Because of the missing information, a similarly complex situation occurred when analyzing the relationship between the number of failures for different pipe diameters and the actual season. In this case, incomplete data was only 10.5% of all the records in the database (8–16%, depending on month, Fig. 5), which is almost twice less than in the previous category. Research has been conducted both by including all available data and by excluding incomplete records. In both cases, it has been established that the largest number of failures (ca. 60%) occurred on small diameters (25–100 mm), i.e. on household connections and some distribution lines. Moreover, in the summer, a bigger number of failures occurred on the

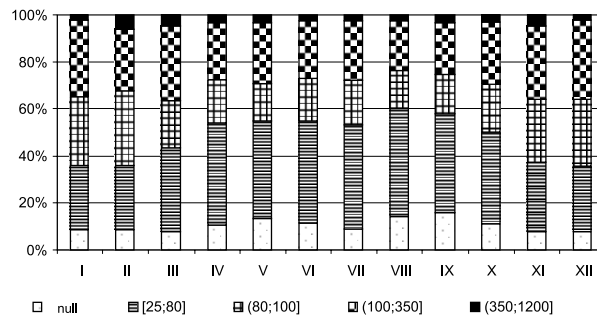


Fig. 5. Percentile distribution of a number of failures in the X water supply system as a function of month and diameter (all data included)

smallest diameters (25–80 mm); the results of both analyses differ by only a few percent. For instance, in winter, 25–30% of all damages concerned pipes of 25–80 mm diameter whereas between April and September it was 42–53%. Such an outcome may result from the fact that the data base does not differentiate between the real failures and general and preventive repairs carried out in summer time. Although based on this data it is possible to draw the general conclusion, these particular examples show how important it is to gather complete information, without which, it is difficult to make a correct judgment.

3.3. Daily analyses

The number of failures (repaired) changes also on the daily basis. The largest number of system failures, 18 failures/day, were repaired on January 9th, 2009 (Fig. 6). It is also noticeable that there were several days when at least 10 failures were repaired.

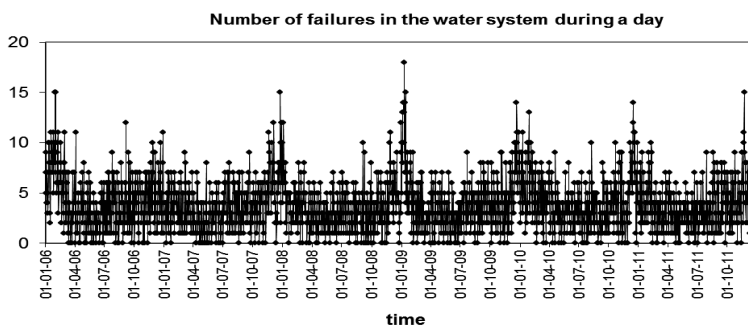


Fig. 6. The number of failures in the *X* water distribution system that were repaired in the subsequent days (2006–2011)

The maximum number of daily failures in every month has been illustrated in Fig. 7. However, in every month there were days when no single failure was repaired. The lowest variability and the lowest number of failures were recorded in the summer (May, June and July), whereas the highest variability was found in the winter (particularly in January).

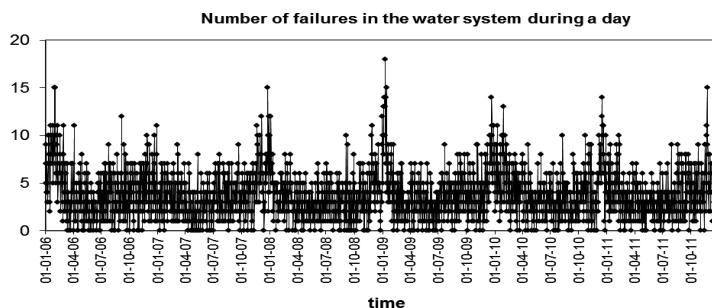


Fig. 7. The maximum number of failures repaired in water distribution system per day (2006–2011)

What may be important for the operator is information about the occurrence of the so-called extreme days (with the lowest or the highest number of failures). Information on the water system leads to the conclusions that 3 repairs per day was the most common result during the year (annual average, 60 days with 3 repairs. A lower number of failures ($k = 0, 1, 2$) occurred rarely – on average 25, 42 and 53 days per year. In the winter, however, the most common daily result was 4–5 repairs per day (in January and December, there were 9 days with such an average). Also in winter, a smaller number of failures ($k = 0, 1, 2, 3$) occurred rarely – on average once, 3, 5 and 7 times per year (Fig. 8).

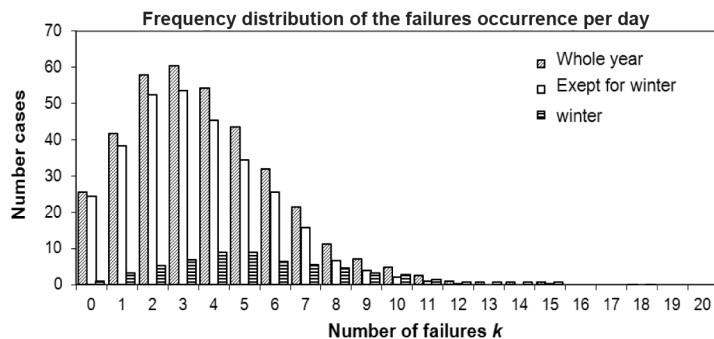


Fig. 8. Distribution of the number of failures in the water system over 1 day (2006–2011)

Taking into account the length of the selected time periods, one can determine the empirical probability of occurrence, and then an empirical probability of exceeding the given number of failures per day (Fig. 9). The probabilities of occurrence of over 5 failures per day are quite similar for a whole year and for the months from February to November. They are 0.226 and 0.185 respectively, while during the winter it reaches 0.44. This indicates that during 44% of the winter (almost 27 days), more than 5 failures were repaired daily. By analogy, the probability of exceeding $k = 10$ per day can be assessed. They are 0.016 during the whole year, 0.073 in winter and only 0.004 in the other months. It means that the number of days when at least 10 failures were repaired were: 5.3 days – average year, 4.5 days – winter and 1.3 days during the rest of the year.

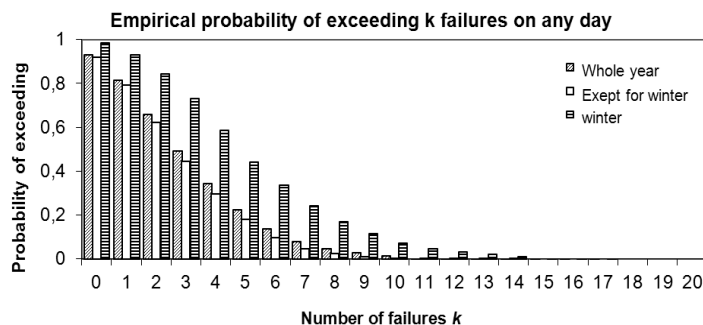


Fig. 9. Empirical probability of exceeding the failure number in the X 's water system on any day

Distribution of days with a significant number of repairs does not yet include the information on the occurrence of so-called ‘black series’ (series of days with a high number of failures). What may be important for the operator is the information if in previous years there had been such series and what was the duration of the longest one. Regarding the analyzed system (Fig. 10), the most common were days when at least 5 failures were repaired ($k \geq 5$) and on days preceding and following, fewer failures were fixed. On average, 34.5 such series ($k \geq 5$) of length $i = 1$ per year were recorded. A similar series of $i = 2$ occurred on average 13 times a year; a series of $i = 10$ was recorded once during the 6-year period.

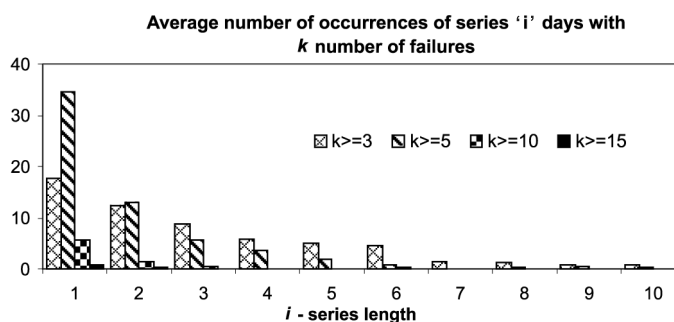


Fig. 10. Average number of occurrences of series – i -days per year, when at least k failures in the X 's water system were repaired

The empirical probability of series duration is illustrated in Fig. 11. It shows that, for example if on any day $k \geq 15$ failures are fixed (the empirical probability of such an event is $p_{k \geq 15} = 0.00273$), the probability that on the following day also at least 15 failures would need repairing is $p_{k \geq 15, k \geq 15} = 0.2$. Although such series probabilities are high, it has to be remembered that these are conditional probabilities. An actual unconditional probability of occurrence of two subsequent days, when at least 15 failures are repaired is only $p_{k \geq 15} \times p_{k \geq 15, k \geq 15} = 0.00273 \times 0.2 = 0.00055$. More useful is an analysis of series of days when at least 5 failures were repaired ($k \geq 5$). The probability (conditional) that the length of such a series would be $i = 1$ is about $p_{k \geq 5} = 0.57$, while the probability that a series length (if any) would be $i = 2$ or $i = 3$ is 0.21 and 0.09, respectively. Unconditional empirical probabilities of such series are respectively 0.465, 0.138 and 0.031.

Fig. 11 only presents the results for series of $i \leq 10$. However, also exceptionally long series may occur.

The longest are those in which small numbers of failures were repaired daily (e.g. for $k \leq 1$, the maximum length of a series is $i_{\max} = 137$, for $k \leq 2$ is $i_{\max} = 56$, and for $k \leq 3$ $i_{\max} = 37$). The latter result indicates that during the evaluated period, the longest period, when at least 3 failures per each following day were repaired, was 37 days. Similarly, over 25 days, at least 5 failures/day were repaired and over 6 days, 10 failures/day (Fig. 12). The longest series and those with the highest number of failures occurred most often during winter. The longest series when no failures were repaired ($k = 0$) was recorded in April and May (maximum length $i = 3$).

On average, there were almost 25 days per year, when no failures were repaired – the highest number of such days was recorded in May (4.2 days), April, June and November

(Fig. 13). The maximum number of consecutive failure-free days ($k = 0$) was $i = 3$ (series of failure-free days). Assuming that no repairs means no failures to be fixed, other actions (maintenance, pre-scheduled repairs) could be set for these months. However, as it can be easily predicted, the smallest number of failure-free days was recorded in the winter (January, December).

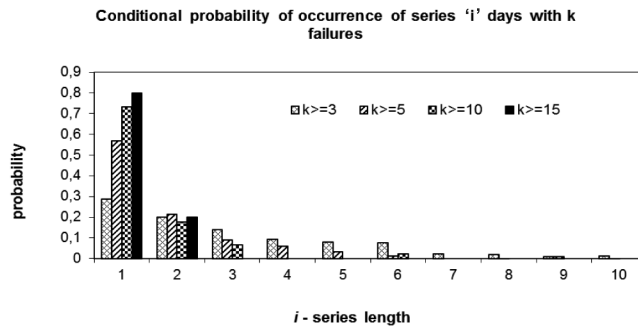


Fig. 11. Distribution of the probability of occurrence of series of i days, during which at least k failures occurred.

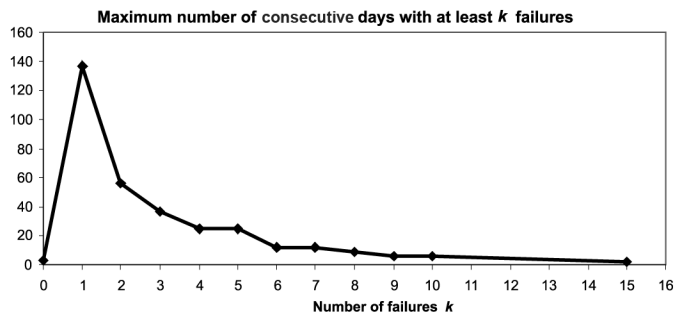


Fig. 12. The maximum number of consecutive days when the number of repaired failures in the X water system was at least k

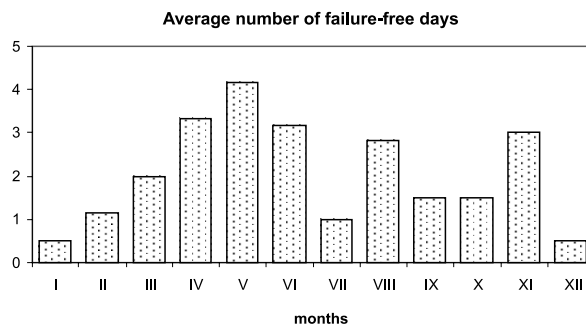


Fig. 13. Failure-free days in the X 's water system

On Mondays, maintenance teams are charged with twice as many tasks as on Saturdays and Sundays (Fig. 14). Also, in the winter, the number of failures requiring repair in the following days of the week is on average, twice as high as in other months.

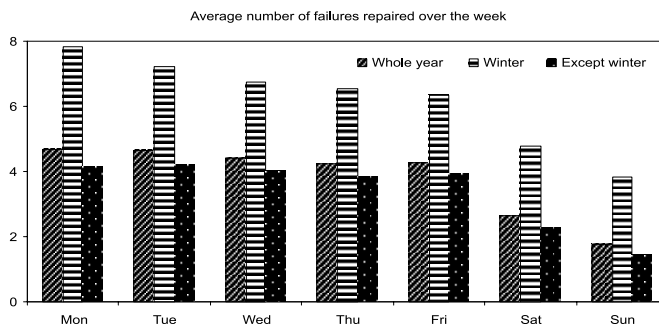


Fig. 14. Distribution of the failures repaired on particular days of the week in the X water system

The analysis leads to the following conclusions. The number of failures k , and the average failure rate λ_0 , show a significant time dependency. This is a strong argument for performing deeper analyses, with more emphasis on yearly, monthly and daily results. Properly conducted research allows for identifying trends, seasonal variations or daily distributions of failures in different times of the year. It is obvious that the more precise the database, the more detailed the analyses and the more reliable results one may expect.

The presented results are only used as examples to suggest how water system failure calendars should be created. Similar analyses could be conducted for particular regions or zones of large dwellings. An analysis should also try to identify reasons for extremely high numbers of failures per day or for series of failure (e.g. extreme weather phenomenon or system operation at high pressure, etc.).

4. Conclusions

- Comprehensive analysis of water system failures should be based on complete databases with distinguished records on occurred and repaired failures.
- Analyses of failures over time can be conducted for consecutive years, months and days – to generate a risk calendar.
- Nowadays, gathering complete and sufficiently detailed information on occurred and repaired failures does not pose problems of a technical or organizational nature. The reasons for poor databases are often the lack of conviction of their suitability or low staff competences. They can be easily dealt with by the operator and do not generate high costs.
- Incomplete databases make it difficult to draw right conclusions. On the other hand, ignoring their incompleteness would result in false conclusions.
- For process analyses, no particular programs are required – the above results were obtained with EXCEL and a few simple macros. Although discussion of results should be assigned to an analyst, in many water utilities, well-trained personnel may do this job.

- Results from analyses originally conducted to help in the creation of a 'risk calendar' may also prove useful for the optimal management of water system operation or better work planning (maintenance, pre-scheduled repairs). The analyses help to identify whether or not there is a seasonal dependence in failure rates to determine the average number of failures in a particular period of time (year, month, day), the probability of exceeding a given number of failures or the probability of 'black series' occurrence.
- In general, the numbers of repaired failures on consecutive days may not be independent. The dependence, over short periods of time, is due to the fact that not all reported failures are fixed immediately. That is the case especially for low priority failures reported at the end of the week and/or on days preceding holidays. Such conditions may also occur during severe winters without snow, when on a few consecutive days there are numerous failures and not enough maintenance teams. Then also, the repair time is longer than average. The lack of independence in longer periods of time is the a result of the seasons' influence on failure occurrence (seasonality).
- The data reliability depends on a complete data base. Additionally, a lack of a clear distinction between random failures and preventive and general repairs causes an increase in the failure rate λ_0 . It may also lead to false conclusions i.e. more work on small diameter pipes in summer results not from a higher failure rate, but from the fact that most new connections are carried out in summer.

The scientific work was financed from funds for research into a self-development project No N R14 0006 10 entitled 'Development of comprehensive methodology for the assessment of the reliability and safety of water supply to consumers'.

References

- [1] Kwietniewski M., Rak J., *Niezawodność infrastruktury wodociągowej i kanalizacyjnej w Polsce*, Komitet Inżynierii Lądowej i Wodnej PAN, Studia z zakresu inżynierii nr 67, Warszawa 2010, 27-32.
- [2] Rak J., *Podstawy bezpieczeństwa systemów zaopatrzenia w wodę*, Monografie Komitetu Inżynierii Środowiska PAN, vol. 28, Lublin 2005, 113-119.
- [3] Tchórzewska-Cieślak B., Wybraniec A., *Metoda wyznaczania obszarów ryzyka awarii w podsystemie dystrybucji wody*, INSTAL 10/2008, 99-101.
- [4] *Wodociągi i kanalizacja w Polsce. Tradycja i współczesność*, red. Dymaczewski Z., Sozański M., Polska Fundacja Ochrony Zasobów Wodnych, Poznań–Bydgoszcz 2002, 367-422.
- [5] Iwanejko R., *Dynamiczne ryzyko związane z niesprawnością sieci wodociągowej*, Aktualne zagadnienia w uzdatnianiu i dystrybucji wody, Gliwice 2011, 297-306.
- [6] *Dane o uszkodzeniach sieci wodociągowej uzyskane z MPWiK miasta X. 2012.*

GRZEGORZ KACPRZAK, PAVEL KRAVCHENKO, WAWRZYNIEC SMOLAK*

COMPARISON OF CPRF MODELING STUDIES RESULTS TO THEORETICAL ONES IN SOIL WITH A LOW BEARING CAPACITY

PORÓWNANIE WYNIKÓW BADAŃ MODELOWYCH FUNDAMENTU PŁYTOWO-PALOWEGO POSADOWIONEGO NA PODŁOŻU SŁABONOŚNYM Z WYNIKAMI TEORETYCZNYMI

Streszczenie

W artykule przedstawiono porównanie wyników badań modelowych fundamentu płytowo-palowego posadowionego na podłożu słabonośnym z wynikami teoretycznymi otrzymanymi przy wykorzystaniu procedury obliczeniowej Poulos'a. Przedstawiono zastosowany model laboratoryjny z interpretacją wyników w postaci zależności obciążenie-osiadanie oraz procentowego udziału pali w przenoszeniu obciążenia.

Słowa kluczowe: badania modelowe fundamentu płytowo-palowego, teoretyczne określenie udziału pali w przenoszeniu obciążenia

Abstract

The paper summarizes the results of modeling studies of combined pile-raft foundation (CPRF) built on soil with a low bearing capacity to theoretical results obtained by using the design procedure by Poulos. Laboratory model used for investigation as well as interpretation of results in form of load-displacement relationship and percentage of load carried by piles were characterized.

Keywords: modeling studies of piled raft foundation, theoretical determination of pile contribution in load transfer

* Ph.D. Grzegorz Kacprzak, Instytut Dróg i Mostów, Wydział Inżynierii Lądowej, Politechnika Warszawska.

** M.Sc. Eng. Pavel Kravchenko, M.Sc. Eng. Wawrzyniec Smolak, Wydział Mostów i Tuneli, Petersburski Państwowy Uniwersytet Komunikacyjny.

Symbols

- V – total vertical applied load
 V_A – applied load at which pile capacity is mobilized
 V^{pu} – ultimate capacity of piles (single pile or block failure mode, whichever is less)
 V_{ru}^{pu} – ultimate capacity of raft
 K_{pr} – axial stiffness of piled raft system
 K_r – axial stiffness of raft
 K_p – axial stiffness of pile group
 β_p – proportion of load carried by piles

1. Introduction

The subject of Combined Pile-Raft Foundation (CPRF) was previously discussed by Zeevaert [20], Davis and Poulos [3], Hooper [9, 10], Burland et al. [4], Sommer et al. [16], Price and Wardle [15], Franke [6], Bartolomey et al. [1], Gandhi and Maharaj [7], Borel and Combarieu [2], Kurillo et al. [12], Tejchman et al. [17], Ulickiy et al. [19], Fioravante and Jamiolkovski [5], Mirsayapov and Artemev [13] and others authors. Despite this studies and theoretical analyses it is difficult to define the part of the load carried by the elements of CPRF. In Russia and Poland there is no proper branch guidance that encourages engineers engaged in the designing process of CPRF enabling them to take into account the transfer of the load to the raft and to the piles simultaneously.

Due to the three-dimensional nature of the problem, a detailed analysis of CPRF is very complex and compels to conduct numerical simulations or laboratory tests. Hence, trying to point out the existing cooperation between elements of CPRF, the authors of this article present some laboratory results of CPRF model built on loose silty sand typical to the soil condition in the region of Petersburg, Russia. Further, the theoretical results obtained by using the design procedure by Poulos were compared to laboratory ones using the load-displacement relationship as well as the percentage of load carried by piles.

2. Practical design procedure for CPRF [14]

Poulos and Davis developed a simplified hand calculation method for constructing the overall load-settlement curve until the failure of CPRF was reached. The elastic solution is used for determination of the initial stiffness of the piled raft and of the raft itself. In consequence a three-linear load-settlement relationship is obtained reflecting the work of the main elements of piled-raft foundation. It should be underlined that only perfectly rigid or perfectly flexible rafts can be considered.

Randolph developed the convenient approximate equations for the stiffness of a piled raft system and the load sharing between the piles and the raft. The method is restricted to linear behaviour of the piled raft system i.e. the initial portion of the load-settlement curve. Other approaches with similar concept were presented by Franke et al. and van Impe and de Clerq. In the latter case, the piled raft is represented by a series of pile-raft segments

having a circular cap. The various interactions are modeled using elastic theory, and the piled behaviour is given by a modification of the analysis by Randolph and Wroth. Although the resulting equations need to be solved using a computer, the calculation process is simple and does not require specialised software. The approach is limited to perfectly flexible or perfectly rigid raft.

A method which combines and extends the approaches by Poulos and Davis and Randolph is described below. It includes the following aspects:

- estimation of the load sharing between the raft and the piles, using the approximate solution of Randolph
- hyperbolic load-deflection relationship for the piles and for the raft, thus providing a more realistic overall load-settlement response for the piled raft system than the three-linear approach by Poulos and Davis.

Figure 1 shows diagrammatically the load-settlement relationship for the piled raft. Point A represents the state at which the pile capacity is fully mobilised when the total vertical load V_A is applied. Over this point, both the piles and the raft share the load. The settlement (S) can be expressed as follows:

$$S = \frac{V}{K_{pr}} \quad (1)$$

Beyond point A, additional load must be carried by the raft, and the settlement is given by:

$$S = \frac{V_A}{K_{pr}} + \frac{V - V_A}{K_r} \quad (2)$$

The load V_A can be estimated from:

$$V_A = \frac{V_{pu}}{\beta_p} \quad (3)$$

One can use the approximate expression described by Randolph for K_{pr} in equation (1) and β_p in equation (3), namely:

$$K_{pr} = XK_p \quad (4)$$

$$X \approx \frac{1 - 0,6(K_r / K_p)}{1 - 0,64(K_r / K_p)} \quad (5)$$

$$\beta_p = \frac{1}{1 + \alpha} \quad (6)$$

$$\alpha \approx \frac{0,2}{1 - 0,8(K_r / K_p)} \left(\frac{K_r}{K_p} \right) \quad (7)$$

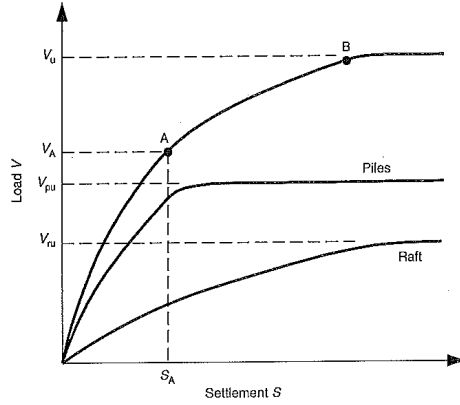


Fig. 1. Load-settlement relationship for CPRF acc. [13]

It is assumed that the pile and raft load-settlement relationship are hyperbolic, then the secant stiffness of the piles (K_p) and the raft (K_r) can be expressed as follows:

$$K_p = K_{pi} (1 - R_{fp} V_p / V_{pu}) \quad (8)$$

$$K_r = K_{ri} (1 - R_{fr} V_r / V_{ru}) \quad (9)$$

where K_{ri} and K_{pi} denote initial axial stiffness of raft and initial axial stiffness of pile group respectively.

The load carried by the piles is given by:

$$V_p = \beta_p V \leq V_{pu} \quad (10)$$

and the load carried by the raft is:

$$V_r = V - V_p \quad (11)$$

Substituting equations (3)–(11) in equations (1) and (2), the following expressions are obtained for the load-settlement relationship of the piled raft system.

For $V \leq V_A$:

$$S = \frac{V}{XK_{pi} \left(1 - \frac{R_{fp} \beta_p V}{V_{pu}} \right)} \quad (12)$$

For $V > V_A$:

$$S = S_A + \frac{V - V_A}{K_{ri} \left(1 - R_{fr} \frac{(V - V_{pu})}{V_{ru}} \right)} \quad (13)$$

where:

$$S_A = \frac{V_A}{XK_{pi}(1 - R_{fp})} \quad (14)$$

with V_A is given by equation (3)

Equations (12)–(14) provide a method for estimating the average load-settlement relationship for the CPRF. Because K_r and K_p will vary with the applied load level, the parameters X and βp will also generally change.

3. Modeling studies of CPRF

The CPRF model consisted of four piles (aluminum tubes of 16 mm diameter with wall thickness of 1.5 mm and 300 mm long) connected to the acrylic glass square-shaped plate (50 mm high and 150 mm width). The model is shown in Fig. 2.

Plate (8) provided guides (2), into which piles (1) were installed. At the top of each pile, aluminum tubes (3) of 6 mm diameter was installed. Steel arm (4), connected directly to frame (5) and plate (8) by spring (6), was set on element (3).

The load was transferred directly on the plate by the pin coupled to the displacement measuring gauge. When the pile was switched on to transfer the load, arm (4) moved causing the spring enlargement measured by gauge (7).

The application of load was carried out gradually; each load step was considered completed when certain stabilization of settlement was achieved. The criterion of settlement stabilisation was adopted at the level of 0.01 mm in 15 minutes.



Fig. 2. Model of CPRF used in presented studies

4. Determination of stiffness of CPRF elements

3.1. Stiffness of pile group

3.1.1. Stiffness of measurement spring

Prior to testing, the equipment was subjected to the procedure of calibration in order to link the displacement of arm (4) which is equal to enlargement of spring (6) in response to applied load i.e. to define the linear stiffness of spring (6), $k_1 = 19 \text{ kG/mm}$.

3.1.2. Stiffness of single pile

Secondly, the non-linear stiffness of the pile k_2 (Fig. 3, dotted lines) was described. In the same soil conditions and using the same laboratory equipment three series of load of single pile tests were performed.

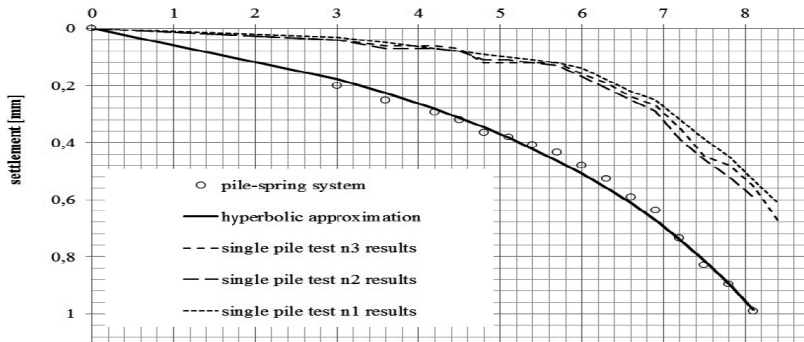


Fig. 3. Load-settlement relationship of single pile (top) and pile-spring system (bottom)

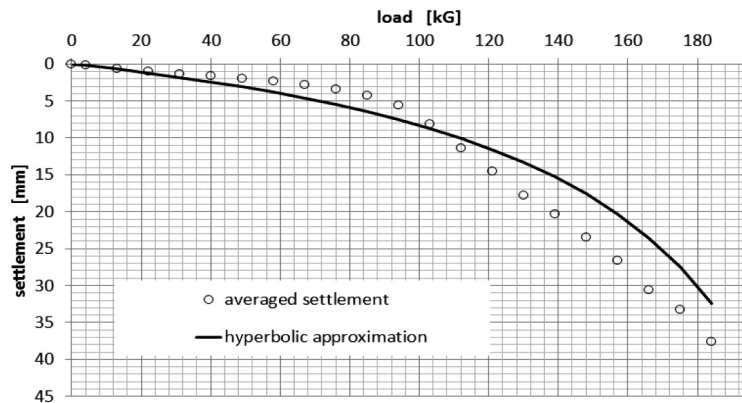


Fig. 4. Load-settlement relationship of raft

The aluminum tube was pressed into the soil to the same depth as for experiments with CPRF model. Then the load was gradually increased and directly transferred to the pile. The increase of load caused the settlement of the pile. Again, the application of load was carried out step-by-step; each load step was considered completed when the settlement of pile was not greater than 0.01 mm in 15 minutes.

3.1.3. Stiffness of serial pile-measurement spring connection system

For the system consisting of serial connection of two springs with different stiffness (pile and measurement spring), the forces acting on each spring, without taking into account the weight of springs, are identical. The total elongation of this system is the sum of extensions of both springs. Hence, we have formulas:

$$F = k_1 x_1, \quad F = k_2 x_2, \quad x = x_1 + x_2, \quad (15)$$

which enable us to calculate finally that the total stiffness of the system k is:

$$\frac{1}{k} = \frac{1}{k_1} + \frac{1}{k_2} \quad (16)$$

3.1.4. Impact factors of pile working in a pile group (Tejchman [17])

Finally, knowing the total stiffness of the system composed of measurement spring and single pile and using the factor of impact of pile acting in a group, one can define the stiffness of pile group. To make easier, the calculation of impact factor of a pile group consisted of 4 piles in square-shaped form installed at the distances equal to 3 fold diameter between them was assumed as 1.0 according to studies made on pile groups in sand by Tejchman [17].

Now, the secant stiffness of pile group in hyperbolic form (8) can be calculated using the following formulas

$$K_{pi} = K_{i1} \cdot 4 / 1 \quad (17)$$

$$R_{fp} = R_{fp1} \quad (18)$$

$$V_{pu} = V_{pu1} \cdot 4 \quad (19)$$

3.2. Stiffness of raft

By analogy with the definition of stiffness of a single pile, the stiffness of the plate was determined. Three series of tests were done. The square-shaped raft 150 mm width was founded on the flat surface of the ground and then gradually loaded. Again, application of load was carried out step-by-step; each load step was considered completed when a settlement of raft was not greater than 0.01 mm in 15 minutes.

5. Comparison of theoretical results from design procedure by Poulos [14] with those obtained from model studies

The aim of this study was to verify the theoretical model procedure given by Poulos [14] whereby piles participate in load carrying up to its bearing capacity and later additional load must be carried by the raft only (see Chapter 2).

Using the design procedure of CPRF presented by Poulos [14] and recalled in chapter 2, settlement of piled-raft foundation in the function of applied load can be obtained and compared with the results from laboratory tests (Fig. 5 left). Analogously, the portion of load carried by the piles can be estimated (Fig. 5 right). Interpretation of both presented figures enables to conclude that the theoretical procedure underestimated the contribution of the pile in load transfer which results in lower stiffness of foundation system (CPRF).

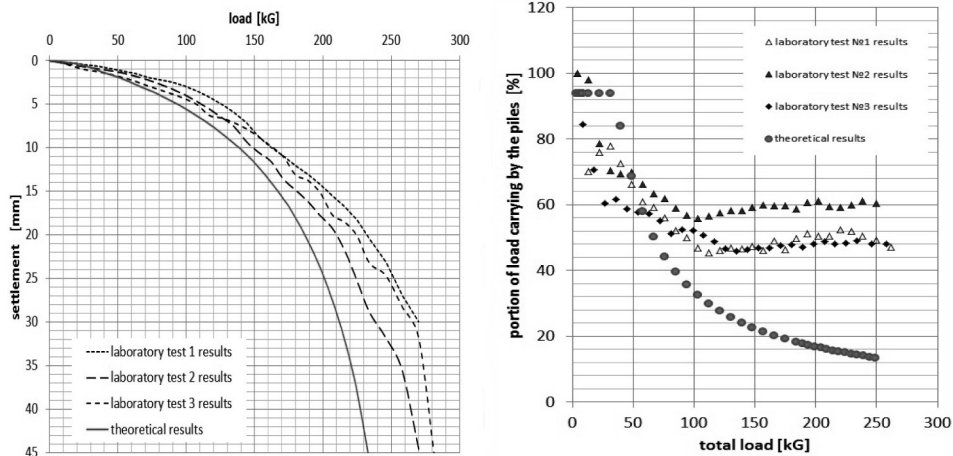


Fig. 5. Comparison of theoretical results to those obtained in laboratory tests. Left: load – settlement relationship. Right: portion of load carried by the piles

Entering the correction factor for the piles by simple enlarging the ultimate capacity of pile group V_{pu} by multiplying by 1.75 results in better fitting the theoretical load-settlement curve to the laboratory results (Fig 6. left). Unfortunately, increased capacity of piles doesn't fit very well to the observation made during laboratory tests: piles take more load then raft at the beginning of loading (up to 40% of total load) and then raft dominates according to theoretical procedure.

From the engineering point of view, the observation of laboratory model tests provide very important information about load distribution on the elements of CPRF foundation. We have noted that piles hold more load then that calculated using Poulos procedure. The same was observed by Hanisch [8] who showed using the FEM analysis that the piles in pile-raft foundation work better showing a steady increasing trend beyond the settlement of pile head corresponding to 3% of pile diameter.

Finally, summarizing the research done, it can be noted that the CPRF design procedure by Poulos enables to safely estimate the load-settlement relationship of CPRF (lower stiffness of foundation system) as well as the load carried by the piles resulting in a larger number of piles. The authors showed that modification of Poulos method by this factor by simple enlarging the ultimate capacity of pile groupe V_{pu} multiplying by 1.75 enables to optimize the total number of piles in Combined Pile Raft Foundation.

Because the research concerned sandy soils, further studies should be focused on CPRF behavior in cohesive soils taking into account secondary consolidation.

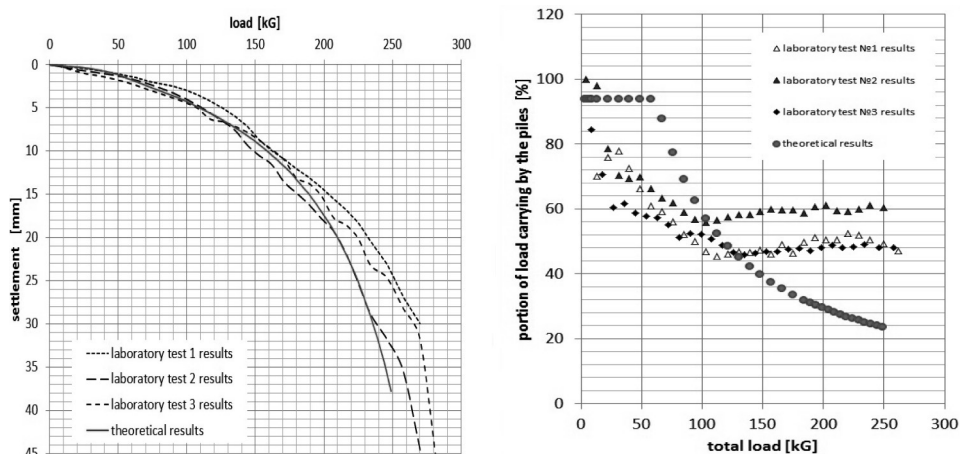


Fig. 6. Comparison of theoretical results with correction factor to those obtained in laboratory tests. Left: load – settlement relationship. Right: portion of load carried by the piles

References

- [1] Bartolomey A.A., Omelchak I.M., Yushkov B.S., *Prognoz osadok svajnyh fundamentov*, pod red. Bartolomeya A.A., Stroyizdat, Moskva 1994, 30-72.
- [2] Borel S., Combarieu O., *Some Observations on Pile Footings*. W: Proc. 2nd Int. PhD Symposium in Civil Engineering, Budapest 1998.
- [3] Davis E.H., Poulos H.G., *The analysis of piled raft systems*, Australia Geotechnique Journal, Vol. No. 1, 1972, 21-27.
- [4] Burland J.B., Broms B.B., De Mello V.F.B., *Behaviour of foundations and structures*. W: Proc. 9th Int. Conf. Soil Mech. Foundn Engng, Tokyo 1977, Vol. 2, 1977, 495-546
- [5] Fioravante V., Jamiolkovski M.B., *Fizicheskoe modelirovanie plitno-svajnyh fundamentov*. Razvitie gorodov i geotekhnicheskoe stroitelstvo, Vol. 10, 2006, 200-206
- [6] Franke E. (1991). *Measurements beneath piled rafts*. W: Key note lecture to the ENPC Conf. on Deep Foundations, Paris 1991, 1-28
- [7] Gandhi S.R., Maharaj D.K., *Behavior of Piled Raft Under Uniform Loading*. W: Proc. Indian Geotechnical Conference (IGC-95), Bangalore, Vol. 1, 1995, 169-172
- [8] Hanisch J., Katzenbach R., König G., *Kombinierte Pfahl-Plattengründungen*, 2002.

- [9] Hooper J.A., *Observations on the behaviour of piled-raft foundation on London Clay*. W: ICE Proceedings. Vol. 55, No. 4., Ice Virtual Library, 1973, 855-877.
- [10] Hooper J.A., *Review of behaviour of piled raft foundations*, Rep. No. 83, Construction Industry Research and Information Association, London 1979.
- [11] Kacprzak G., Kravchenko P., Smolak W., *Rozkład obciążenia na elementy fundamentu płytowo-palowego posadowionego na podłożu słabonośnym*. Politechnika Białostocka, Budownictwo i Inżynieria Środowiska, vol. 4, no. 3, 2013, 205-209.
- [12] Kurillo S.V., Skorohodov A.G., Fedorovskiy V.G., *Kraschetu osadok svajnyh i svajno-plitnyh fundamentov*. NIIOSP, Moskwa 2003.
- [13] Mirsayapov I.T., Artemev D.A., *Modelirovanie napryazhenno-deformirovannovo sostoyania plitno-svajnovo fundamenta pri sovmestnom deformirovanii s okruzhayushchim gruntowym massivom*. Vestnik grazhdanskih inzhenerov, 19, 2009, 77-82.
- [14] Poulos H.G., *Practical design procedures for piled raft foundations*, Design applications of raft foundations, 2000.
- [15] Price G., Wardle I.F., Queen Elizabeth II Conference Centre: *monitoring of load sharing between piles and raft*. W: ICE Proceedings. Vol. 80, No. 6., Ice Virtual Library, 1986, 1505-1518.
- [16] Sommer H., Wittmann P., Ripper P., *Piled raft foundation of tall building in Frankfurt Clay*. W: Proc. 11th International Conference on Soil Mechanics and Foundation Engineering, San Francisco 1985, Vol. 4, 1985, 2253-2257.
- [17] Tejchman A., *O osiadaniu grup palowych*. Sesja naukowa z okazji jubileuszu 70-lecia profesora Zbigniewa Grabowskiego, Politechnika Warszawska, 2000, 231-238
- [18] Tejchman A., Gwizdała K., Słabek A., *Obliczanie fundamentów płytowo-palowych*, W: II Problemowa Konferencja Geotechniki „Współpraca budowli z podłożem gruntowym”, Tom 1, Białystok-Białowieża 2004, 232-3346.
- [19] Ulickiy V.M., Shashkin A.G., Shashkin K.G., Vasenin V.A., *Rekonstrukciya gorodov i geotekhnicheskoe stroitelstvo*, Vol. 8, 2004, 68-82.
- [20] Zeevaert L., *Compensated friction-pile foundation to reduce the settlement of buildings on the highly compressible volcanic clay of Mexico City*, W: Proc. 4th International Conference on Soil Mechanics, London 1957, 81-86.

GRZEGORZ KACPRZAK, ŁUKASZ STEFAŃSKI*, PAWEŁ PIETRZYKOWSKI**

TRANSFORMATIONAL FUNCTIONS FOR DISPLACEMENT COLUMNS PERFORMED IN COHESIVE LOW-BEARING-CAPACITY SOILS

FUNKCJE TRANSFORMACYJNE DLA KOLUMN PRZEMIESZCZENIOWYCH WYKONYWANYCH W SPOISTYCH GRUNTACH SŁABONOŚNYCH

Abstract

The paper presents the method of determining the total non-linear correlation of load settlement relationship for individual concrete displacement columns performed in cohesive low-bearing-capacity soils, gytja in Żoliborz-Szczęśliwice glacial tunnel valley.

Keywords: gytja, transformational function, settlement

Streszczenie

W artykule przedstawiono metodę wyznaczenia globalnej nieliniowej zależności obciążenie-osiadanie dla pojedynczych kolumn przemieszczeniowych wykonywanych w spoistych gruntach słabonośnych, gytjach „Rynny Żoliborsko-Szczęśliwickiej”.

Słowa kluczowe: gytia, funkcja transformacyjna, osiadanie

* Ph.D. Eng. Grzegorz Kacprzak, Eng. Łukasz Stefański, Zakład Geotechniki i Budowli Podziemnych, Wydział inżynierii Lądowej, Politechnika Warszawska.

** M.Sc. Paweł Pietrzykowski, Państwowy Instytut Geologiczny, Państwowy Instytut Badawczy.

1. Classification and mechanical characteristic of gyttja

In accordance with the Polish Standard PN-B-02480: 1986 concerning beside other classification of soils for engineering purposes, gyttja is described as "mud with calcium carbonate content of more than 5%, which may change soil skeleton giving the nature of the rocky soil with low compressive strength values".

According to Długaszek [1] gyttja are composed of lacustrine deposits containing more than 2% of organic matter, and includes the lacustrine chalk, the sediment containing more than 80% of the calcium carbonate content, organic matter may be less than 2%.

Specialists in natural and engineering sciences (i.e. agriculture, geology, geotechnics and construction sector, engineering geology, sedimentology, petrology, soil science, botany) are interested in lacustrine deposits, especially in gyttja. That wide range of scientific applications concerning this type of soil required the introduction of a number of definitions and classifications.

Since when in 1862 Hampus von Post has adapted the Swedish word "gyttja" literally meaning "slime" or "ooze" (Myślińska [5]) to determine a specific type of lake sediments, several dozens of organic soils' classifications, including lacustrine sediments as well as gyttja have been created.

A simple classification by Długaszek [1], concerning only gyttja and a simplified classification by Okruszko [7] are according to the authors' opinion the most appropriate engineering and geological classification of this type of soil for engineering purposes.

The most common types of gyttja described in the branch literature concerning engineering geology and geotechnics are based on classifications by Okruszko [7], Markowski and Ilnicki and present the percentage content of easily determined elements in the sediment (calcium carbonate, organic material and non-carbonate mineral grains and particles).

According to selected classification, the comparison of some types of gyttja presented in the Table 1 was made. The samples were collected from the terrain where the columns were installed.

Table 1

Comparison of several types of gyttja according to selected classification

calcium carbonate CaCO ₃ (%)	organic material Iom (%)	non-carbonate mineral grains and particles (%)	gyttja type by Długaszek	gyttja type by Okruszko	gyttja type by Ilnicki	gyttja type by Markowski
10	22	68	Mineral and organic low carbonate gyttja	clayey gyttja	organic and clayey gyttja	lacustrine mineral deposits
calcium carbonate CaCO ₃ (%)	organic material Iom (%)	non-carbonate mineral grains and particles (%)	gyttja type by Długaszek	gyttja type by Okruszko	gyttja type by Ilnicki	gyttja type by Markowski
50	22	28	mineral and organic high carbonate gyttja	calcareous/lime gyttja	calcareous/lime gyttja	calcareous/lime gyttja

To expand the knowledge about the mechanical properties of gytja and to use some common designing method for displacement columns based on in-situ tests, such tests (CPT and DMT tests) were made in six sites in Warsaw, located in Żoliborz-Szczęśliwice glacial tunnel valley. Macroscopic description and gradation tests classified the investigated soil as gytja with particle size distribution typical for silts. The same conclusions gave Flat Dilatometer Tests (DMT) (68% of 559 readings by DMT were qualified as silts). Moreover, preliminary tests of Atterberg limits gave the same results to those obtained from CPT/CPTU. On the modified Casagrande plasticity chart (ASTM D 2487-93, BS EN ISO 14688-2:2006/ Ap2:2012; Grabowska-Olszewska [2]) the results of the investigated gytja were clustered in a very cohesive group, below the A line, separating soils CL (lean clay) and CH (fat clay) from soils ML (silt) and MH (elastic silt) or OH (organic clay). Basing on original Casagrande plasticity chart, the investigated gytja with liquid limit $WL > 50\%$ gave the results clustered in the group of high plasticity with the symbol OH. Using the extended group of plasticity (eg, according to the classification form in conformity with the British Standards – BS 1377: Part 2:6,4; 1990), the tested soil was characterized by extremely high plasticity and therefore it may be marked by symbol OE.

Although the particle size distribution was typical for silts (done by laboratory tests and DMT), the results of CPT/CPTU clearly showed (more than 96% of 6566 readings of cone resistance and sleeve friction) that the investigated gytja from Żoliborz-Szczęśliwice glacial tunnel valley revealed the characteristic properties of glacial tills (sandy clays) and clays. The classification was based on adaptation of Robertson profiling chart to Polish soils classification PN-B-04452: 2002. Such observations allows to treat gytja like clays/sandy clays for estimating the bearing capacity of displacement columns.

2. Transformational functions

2.1. Recommended functions

According to the recommendations by Gwizdała [3] the load-settlement of column head can be determined with sufficient accuracy using hyperbolic function or power function. Their general form could be presented in the following formulas (1) and (2).

The general form of hyperbolic function is as follows:

$$q = \frac{z}{a_1 + \frac{z}{\alpha_1 q_f}} \quad \text{for } z \leq z_f \quad (1)$$

where:

- α_1 – correction factor for hyperbolic function (1,25 by Det Norske Veritas according to [3]),
- a_1 – initial slope of the curve,
- q_f – shaft (t_{\max}) or bottom resistance (q_p) of the column [kPa],
- z – settlement of column head [m],
- z_f – column head displacement required to mobilize resistance along the shaft (z_v) or in the bottom of the pile (z_p) [m].

The general form of power function:

$$q = q_f \left(\frac{z}{z_f} \right)^\beta \quad \text{for } z \leq z_f$$

where:

- β – selected on the basis of the calculation to get the best compatibility with the field test results,
- q_f – shaft (t_{\max}) or bottom resistance (q_p) of the column [kPa],
- z – settlement of column head [m],
- z_f – column head displacement required to mobilize resistance along the shaft (z_v) or in the bottom of the pile (z_p) [m].

2.2. Column shaft or column bottom resistance based on CPT test results

In order to determine the unit column shaft (t_{\max}) or column bottom resistance (q_p) modified Bustamante and Gianceselli method was used (for details see [6]) treating gyttyja as clay, according to CPT test results presented in chapter 1.

2.3. Full mobilization criteria

The international study on column head displacement needed to mobilize the column shaft or bottom of column resistance presented by Gwizdała [3] show that the threshold of 2–5% column diameter D and 10% D must be reached respectively. Preliminary study on interpretation of column load test made in gyttyja indicated that the mobilization of column shaft resistance responds similarly to the mobilization of bottom resistance, requiring the column head displacement of 0.1 D . Finally, to determine the proper transformation function for all columns, $z_f = z_v = 0.1 D$ were adopted.

2.4. Determination of transformation functions

To determine the key parameters initial values for the transformation function of shaft as well as column bottom (hyperbolic and power function, see Tab. 2), two column field load tests were performed in standard way with additional measurements of axial force distribution along column cores using a chain of connected, retrievable extensometers (the construction and operating principles of the extensometers was described in detail, see for example Krasinski [4]).

Table 2

Initial range of estimated parameters for transformational functions

		Column no. 255	Column no. 273
β (for power f.)	bottom of column	0.5494	0.5892
	column shaft	0.5325	0.5805
a_1 (for hyperbolic f.)	bottom of column	0.0035	0.0034
	column shaft	0.0492	0.0564

The next step was to use appropriate Curve Fitting method and with previously obtained parameters scope, which resulted in determining precise values β and a_1 for the transformation function of column shaft and column toe, see Tab. 3. The key parameters were found using all available test load results for the global function, The fitting was done separately for each column to obtain the local function. Fig. 1 and Fig. 2 present histograms of local and global fitting for respectively hyperbolic and power function being the sum of transformation function of shaft and toe of column.

Table 3

Parameters for local and global functions

		Local function	Global function
β (for power f.)	bottom of column	<0.2879–1.0000>	0.6447
	column shaft	<0.4670–1.0000>	0.6326
a_1 (for hyperbolic f.)	bottom of column	0.00355	0.00355
	column shaft	<0.0350–0.2000>	0.1162

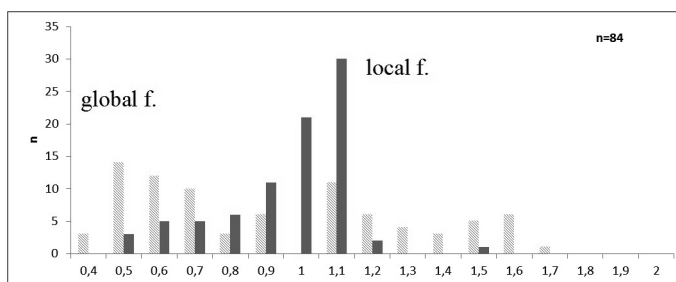


Fig. 1. Frequency bar chart of compliance for hyperbolic function

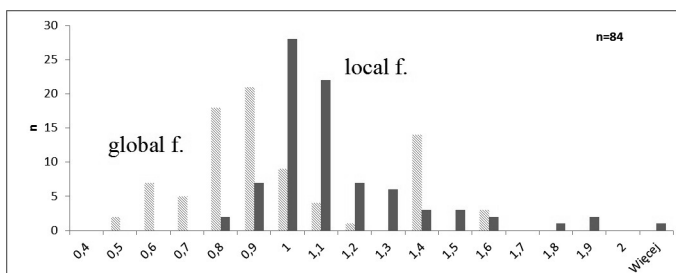


Fig. 2. Frequency bar chart of compliance for power function

Because unique parameters of transformation function are needed i.e. for the global function, better compatibility is attained for power function. These results in the vast majority have better compatibility factor (< 1). The results for which compatibility factors are greater than 1 are observed in the initial stage of the load-settlement ratio during the load test (see details in [6]).

The result of all the performed tests and their analysis allowed to create new transformation power functions for bottom (3) and shaft of column (4) respectively.

$$q = q_f \left(\frac{z}{z_f} \right)^{0.6447} \quad (3)$$

$$t = t_{\max} \left(\frac{z}{z_v} \right)^{0.6326} \quad (4)$$

3. Summary

In order to determine the transformation function of shaft and bottom of column, a series of 19 in-situ static load tests of concrete displacement column with diameter of 40 cm in gyttja and based on stiff clay were performed. Authors compared the field results with those estimated using power and hyperbolic function. Analysis of all obtained results shows that power function with found key parameter $\beta = 0.6326$ and $\beta = 0.6447$ for shaft and bottom of column respectively, can be used in the sufficient estimation of load-displacement relation for separately working column in a cohesive low-bearing-capacity soil (gyttjas of "Rynna Żoliborska").

References

- [1] Długaszek M., *Ocena właściwości fizyczno-mechanicznych gyttii Pojezierza Olsztyńskiego dla potrzeb inżyniersko-geologicznych*, rozprawa doktorska, Archiwum Wydziału Geologii Uniwersytetu Warszawskiego, Warszawa 1988
- [2] Grabowska-Olszewska B., *Plastyczność i pęcznienie różnych genetycznych typów gruntów spoistych*, Seminarium „Badania geotechniczne i ich zastosowanie w projektowaniu”, Polska Akademia Nauk. Sekcja Geoinżynierii Komitetu Inżynierii Lądowej i Wodnej, Instytut Dróg i Mostów Politechniki Warszawskiej: 45-54, Warszawa 1995.
- [3] Gwizdała K., *Fundamenty palowe. Technologie i obliczenia*, Wydawnictwo naukowe PWN, rozdz. 5 i 6, Warszawa 2010.
- [4] Krasieński A., Sieńko R., *Measurement of the vertical force distribution in a pile during static tests*, Materiały 56 Konf. Naukowej KILiW PAN i KN PZITB, 161-168, Krynica 2010.
- [5] Myślińska E., *Grunty organiczne i laboratoryjne metody ich badania*, Wydawnictwo Naukowe PWN, Warszawa 2001.
- [6] Stefański Ł., *Zastosowanie funkcji transformacyjnych do przedstawienia zależności obciążenie-osiadanie w gyttiach Rynny Żoliborskiej*, praca inżynierska, Politechnika Warszawska, Warszawa 2013.
- [7] Żurek-Pysz U., *Inżyniersko-geologiczna charakterystyka kredy jeziornej i gyttii z Grabowa, Marcelina i Prostynii na Pomorzu Środkowym*, Rozprawa doktorska, Archiwum Wydziału Geologiczno-Poszukiwawczego Akademii Górniczo-Hutniczej im. Stanisława Staszica, Kraków 1989. .

PIOTR KANTY*

RESEARCH ON THE INFLUENCE OF THE APPLIED STONE COLUMN FORMATION METHOD ON THE CONSOLIDATION TIME OF THE SURROUNDING SOIL

BADANIA WPŁYWU TECHNOLOGII FORMOWANIA KOLUMNY KAMIENNEJ NA CZAS KONSOLIDACJI JEJ OTOCZENIA

Abstract

Dynamic replacement (DR) and vibro replacement (VR) are the most common methods of stone column formation applied in Poland. A stone column acting as a drain is considered as a method of speeding up the soil consolidation process. However, the influence of the column formation process itself on the consolidation time is unknown. Dynamic effects as well as the destruction of soil structure taking place during DR column formation may extend the time of soil consolidation in comparison to less invasive methods, like vibro replacement. To verify this thesis, laboratory model tests of three VR columns and three DR columns were conducted at the geometric scale 1:40. Weak soil was imitated with very soft clay and the column material – with gravel. In order to identify phenomena occurring during the investigation, the clay itself was tested as well and FEM was applied. The initial parameters used in the numerical analyses were taken from standard laboratory tests.

Keywords: dynamic replacement method, rammed stone columns, physical modelling

Streszczenie

W Polsce kolumny kamienne kształtuje się najczęściej metodą wymiany dynamicznej lub wibrowymiany. Uznaje się, że kolumna kamienna pracująca jako dren przyspiesza proces konsolidacji podłoża. Nie wiadomo jednak, jak proces sam formowania kolumny wpływa na czas konsolidacji. Możliwe, iż efekty dynamiczne jak i zniszczenie struktury gruntu, towarzyszące wbijaniu kolumn w metodzie wymiany dynamicznej, wydłużają czas konsolidacji podłoża w odniesieniu do technik mniej inwazyjnych, jak na przykład wibrowymiana. W celu weryfikacji tej tezy wykonano laboratoryjne badania modelowe trzech kolumn wibrowymiany i trzech kolumn wbijanych. Badania wykonano w skali geometrycznej 1:40. Za grunt słaby posłużyła miękkoplastyczna glina, za materiał kolumn żwir. W celu lepszej identyfikacji zjawisk zachodzących podczas badań wykonano również badanie samej gliny bez kolumny oraz posłużono się metodą elementów skończonych. Parametry wyjściowe do analiz numerycznych uzyskano ze standardowych badań laboratoryjnych.

Słowa kluczowe: wymiana dynamiczna, wbijane kolumny kamienne, badania modelowe

* M.Sc. Kanty Piotr, Department of Geotechnics and Roads, Faculty of Civil Engineering, Silesian University of Technology.

Symbols

DR	–	dynamic replacement
VR	–	vibro replacement
ϕ'	–	effective angle of internal friction [°]
c'	–	effective cohesion [kPa]
k_{10}	–	hydraulic conductivity at 10°C [cm/s]
Mo	–	oedometric moduluj [MPa]
σ	–	stress [kPa]
w_{ini}	–	moisture [%]
ρ_d	–	relative density [g/cm ³]
c_u	–	shear strength [kPa]

1. Introduction

1.1. Description of the method

Both Dynamic Replacement (DR) and Vibro Replacement (VR) techniques are used to reinforce weak soils (especially soils which can be significantly compressed, e.g. soils with organic content, weak clay soils and loose anthropogenic soils).

Introducing stone material into the soil requires the use of equipment that enables free drop of an 8–20 t rammer from a height up to 25 m [12]. This kind of equipment with a suspended rammer used for stone column formation is presented in Fig. 1a. First of all, the dropping rammer forms a crater which is filled with coarse-grained material (such as rubble, stone aggregate, blast furnace slag, burnt shale and debris). The material is rammed until it is introduced into the surrounding soil. When the crater becomes empty again, it is refilled with the material and the sequence is repeated. The formation process continues until the soil becomes significantly resistant to further ramming. The procedure ends when an aggregate column is completed. The vertical bearing capacity of the column is higher than the vertical bearing capacity of the soil naturally occurring on site. In Poland, the most common column diameter is about 2.5 m and its length is up to 5 m [9]. The particle size of the aggregate used for stone column formation is generally 30/120, 30/300, 0/500 mm [8].

In the vibro replacement method, columns are formed with a special vibrator. The formation process can be divided into three main stages:

- The vibrator penetrates the soil to the design depth. The penetration process is often aided by compressed air or water jetting, or by the use of air-water mixture.
- The crater is filled with aggregate. The vibrator is lifted and at the same time, a portion of aggregate is introduced from above to the main part of the vibroflot and then released through a hole located in the main part of the vibroflot. The aggregate of previously determined particle size, is introduced to the main part of the vibroflot through a special feeder in the upper part of the equipment (Fig. 1b).
- The introduced aggregate is compacted as the vibrator is lifted in a reciprocating motion. Downward movements of the vibrator displace and densify the aggregate. The compaction proceeds by stages, every 0.3–0.5 m.



Fig. 1. Equipment for a) DR and b) VR column formation

During the VR column formation process, no soil is withdrawn to the surface and therefore there is no need to remove big quantities of soil. The columns formed with the use of vibro replacement method are also called gravel columns. Their diameters vary between 0.6 and 1.2 m and they are up to 45 m long. The column diameter depends on the vibrator dimensions. In general, the size of the used aggregate is 0–31.5 mm, which is determined by the vibrator shape. Particles of bigger size could constitute obstructions inside the vibrator.

Both DR and VR columns are designed in triangular, rectangular and hexagonal grids [6]. Their axial spacing differ due to different stone column diameters. What can be similar in both techniques are the values of the soil replacement ratio, that is the ratio of column section surface to the surface of its immediate vicinity (the so called unit cell [6, 11]).

1.2. Description of the research problem

In the case of both methods, cone resistance changes occur in the soil adjacent to the stone column, this is reflected in changes of strength and shear parameters. This type of change is the object of the author's research [15]. For information on the aforementioned changes in the VR method, see [1]. These changes are due to the specificity of a given technology and to the drainage function of the columns. The drainage effect of VR columns is described in international literature [2–4], whereas the case of DR columns has yet to be examined. The research described in [13, 14] is one of the few attempts to examine this question.

While analytical methods of designing vibro-column reinforcement exist [6, 10], there are no algorithms for driven columns which would take into account the specific method of their construction [6–8]. While designing such columns, two factors are taken into consideration: the column's bearing capacity; settlements of the system consisting of the column and its surrounding [9]. The drainage effect is very rarely taken into account in projects, whereas it is visible during the construction of reinforcements realized with the use of DR and VR methods. As an example, we propose the photo (Fig. 2) of the area reinforced with the DR method. This photo was taken on one of the building sites in Poland.

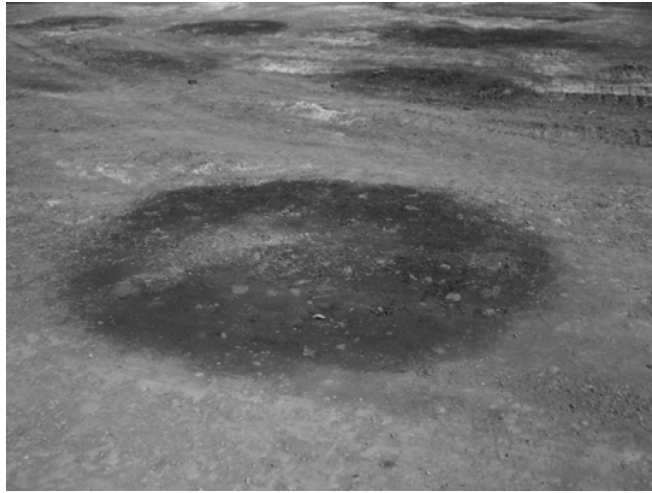


Fig. 2. Area reinforced with the DR method, visible damp spots in places where columns are located

The research described below is the first attempt of the author to determine, via laboratory tests, the efficiency of the DR column drainage in comparison to the VR column.

2. Research methodology

2.1. Description of the test stand

The research aim was to construct three DR and three VR columns and to perform one model test without columns.

All the tests were performed at a geometric scale of 1:40, inside a tube which was 30 cm in both diameter and height. In every test, the tube was filled with sand up to 12.5 cm, on which a 12.5 cm layer of clay was placed (Fig. 3). Sand represented the strong soil layer and clay represented the layer of weak soil that needed to be reinforced. Sand and clay were placed layer by layer (about 2.5 cm each) and always compacted in the same way. The tube was placed on non-woven geotextile fabric, which allowed water to drain freely. The next step consisted of placing the load on the model without column and, for the DR and VR models, in column formation.

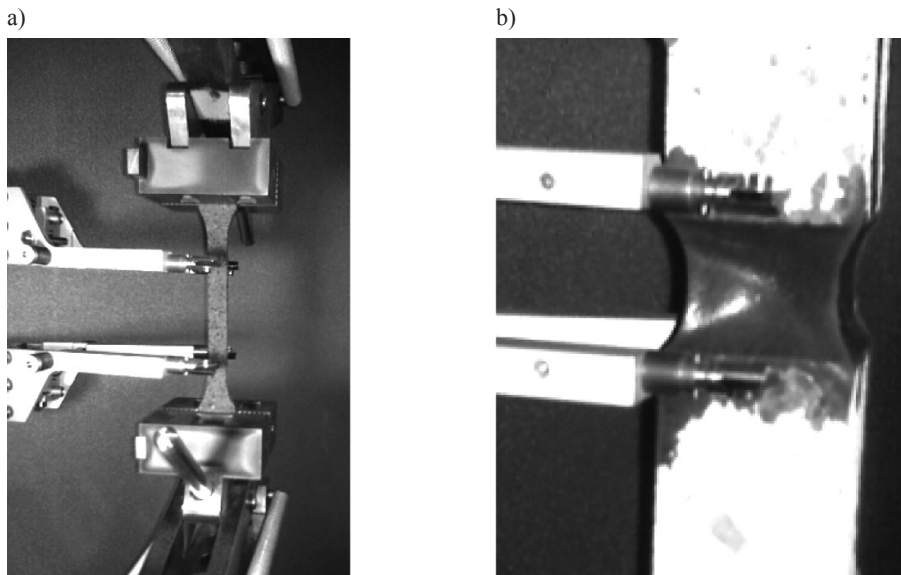


Fig. 3. Schematic research models: a) with column, b) without column

Soil parameters used in the research (Table 1) were determined on the basis of standard laboratory test.

Table 1

Materials parameters used in laboratory tests

Soil type	ϕ' [°]	c' [kPa]	k [cm/s]	M_o [MPa] for $\sigma = 2.5\text{--}5.0$ kPa	w_{in} [%]	ρ_d [g/cm ³]	c_u [kPa]
Silty Clay	9	27	$2.6 \cdot 10^{-6}$	0.27	46.6	1.20	13
Sand	41	0	0.01535	5.78	0.1	1.91	–
Gravel	44	0	0.09690	7.14	0.1	1.70 (VR) 1.84 (DR)	–

2.2. Column formation

DR columns were formed with a 200 g steel weight which was 5 cm in height and 2.5 cm in diameter. Every column was formed by 10 drops from a height of 70 cm and 3 drops from 35 cm. After each drop, the formed crater was refilled with gravel. When the rammer did not penetrate the soil anymore, the column construction was completed (Fig. 4a).

To form VR columns, a 5-cm-diameter tube was screwed in up to the required depth and then unscrewed, removing the clay to the surface of the ground. The formed crater was filled from above (Fig. 4b). In order to prevent dynamic effects, the column material was not compacted, as happens in real conditions when the vibrator is pulled out in a reciprocating motion.

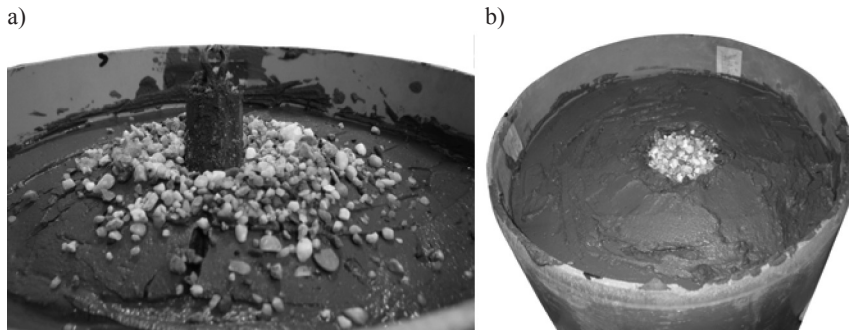


Fig. 4. a) the last stage of DR column formation, b) completed VR column

In spite of the different densities of the gravel that the columns were formed from, volumes of both columns were similar (1200 m^3 and 1140 m^3).

2.3. Settlements measurements

When the columns had been completed, loads with a total mass of about 39.3 kg were placed on each sample. Steel loads (Fig. 5) were put one by one on the surface of the samples. The operation lasted approximately 10 minutes. This induced stress of about 5.6 kPa. Sensors accurate to 0.001 mm were used to measure vertical displacements. While the loads were being placed, measurements were performed by three sensors located close to the edges (Fig. 5). Two hours later, only one sensor located in the center of the upper load was used. The measurements were conducted over a 1440 hours (60 days) period. The readings were performed initially every 10 seconds, later, every 2 minutes and in further stages, every 20 minutes.



Fig. 5. Samples during the consolidation process: a) within two hours of completion

2.4. Moisture changes tests

60 days later, after final vertical displacements had been registered, test systems were successively dismantled and samples were collected in order to conduct moisture tests. The mentioned samples were taken from 5 levels: 4 and 8 cm (sand), 14, 18 and 22 cm (silty clay) measured from the bottom of the tube, according to Fig. 6. At each level, 12 samples were collected: four at 4, four at 8 and four at 12 cm from the column axis. They were taken from an axes perpendicular axes of the tube. Moreover, 5 samples of material were collected from different levels on the axis of the system. In total, moisture of about 450 samples was examined. The moisture values of samples taken from the same localization were averaged.

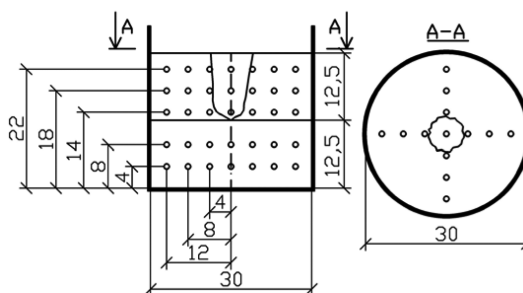


Fig. 6. Localization of the points where the samples for moisture tests were taken

Consolidation curves obtained from measurements of vertical displacements were processed on a spreadsheet. The results for DR and VR models were interpreted on the basis of the averaged values of the measurements.

3. Laboratory tests results

The key results of the conducted research are presented and discussed below. These are consolidation curves of column-surrounding weak soil system and soil moisture changes that vary depending on the distance to the column.

3.1. Consolidation curves of the test system

Figure 7 presents consolidation settlement values for models with DR and VR columns, as well as for the weak soil without column. The first minutes of the test, when the load was being placed on the samples and immediate settlements occurred, are not presented on the graph (Fig. 7a, b).

The differences between consolidation settlements values for DR and VR columns, shown in Fig. 7a, are minor (about 6%). Settlements of DR system are smaller, which is probably due to the difference in column material density, as DR column material is more compact. Smaller settlements may also be the results of the column formation method itself, which changes the parameters of the surrounding soil.

The settlements for the model without column were almost twice as big as those for the models with columns.

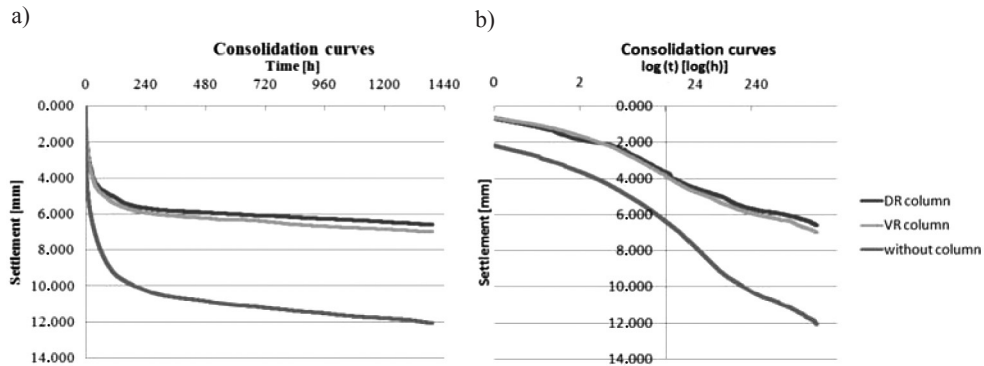


Fig. 7. Averaged consolidation curves for particular models

In this paper, we do not analyse the values of settlements, but their changes over time (the inclination of consolidation curves). It should be noted that the consolidation curves for both models with columns are perpendicular almost from the beginning of loading. It is clearly seen on the graph in logarithmic time scale (Fig. 7b). The behaviour of the model without column is similar up to a certain point after loading, when the consolidation curve becomes more inclined. It can be explained by slower filtration consolidation. Thus, it seems that the method of column formation has no significant influence on the time and course of consolidation process of the column surrounding. Both DR and VR columns accelerate the soil consolidation process in the same way.

3.2. Moisture

Samples for moisture investigation were collected as described above. Initially, the average value of clay moisture for the DR and VR column models, as well as for the model without a column, were 46.0% ($\pm 0.5\%$). The initial values of moisture for sand were equal (0.1%). After 60 days of consolidation, different moisture values for cohesive soil and underlying sand were registered, depending on their distance from the system axis. Fig. 8 presents the results of the investigation.

It was observed that the moisture of soil in the DR column model is higher in almost every measuring point than the moisture in the VR column system. The differences are insignificant (about 0.5%). Test precision was also determined to be 0.5%. Higher moisture values for DR columns system may be related to the lower filtration capacity of these type of columns. The inclination of moisture measurements results is noticeable in both cases. In the upper part of the system ($h = 22$ cm), moisture values are similar and are not influenced by the distance from the column ($\Delta = 0.5\%$). It is clearly visible in the lower part of silty clay ($h = 14$ cm) that the moisture value drops in the vicinity of the column and rises next to the tube sides ($\Delta = 2.0\text{--}3.0\%$). When it comes to sand, the differences are not significant

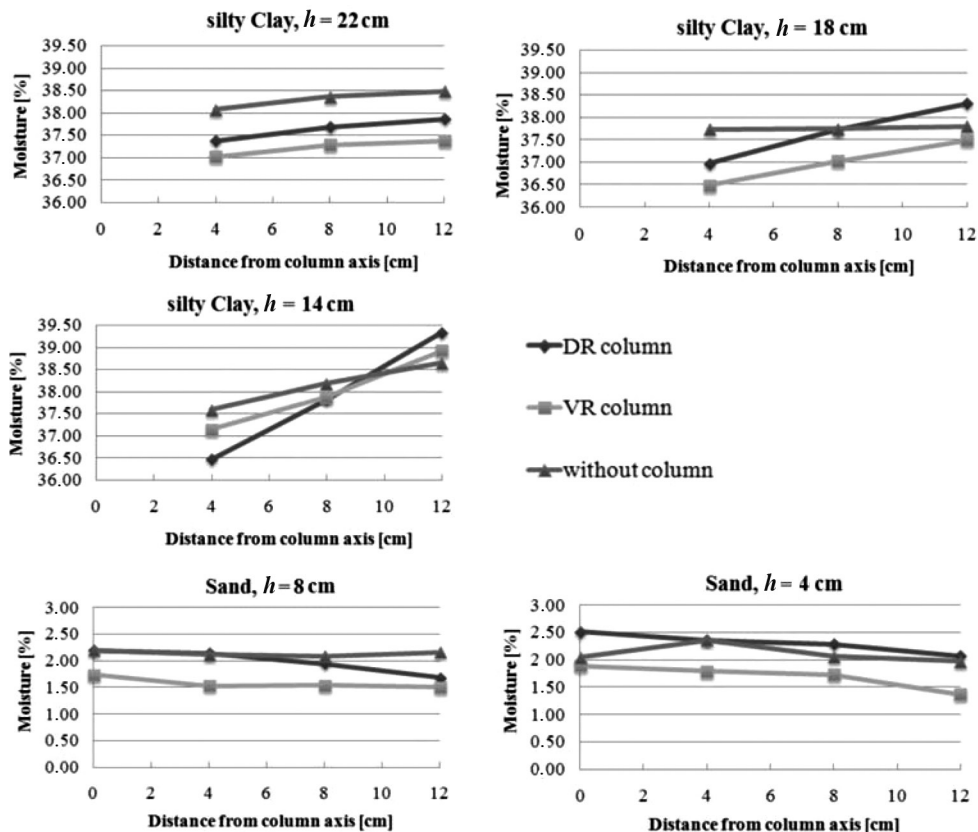


Fig. 8. Results of moisture investigation of the measurement system

($\Delta = 0.5\%$), but moisture values tend to be higher in measuring points located under the column. The measurements indicated the highest moisture values under the column and the lowest in the sand adjacent to the tube sides. These observations indicate the existence of vertical and horizontal water flow in the analyzed system. The influence of vertical filtration is distinctive.

The interpretation of the results of measurements performed in the system without a column is more difficult. The upper part ($h = 22$ cm) of the system without a column showed higher moisture values than the models with columns and the results were the same for all the measuring points. It proves that the columns improve the filtration of the entire system and that the soil moisture in the upper part decreases more quickly. However, the differences are minor ($\Delta = 0.5\text{--}1.0\%$). The situation in lower parts of clay is similar only in the measuring points located in the closest vicinity the centre of the system. The closer the sides, the moisture values become the same or even (in the system without column) they are smaller than others ($h = 14$ cm). When it comes to sand, the moisture values of the system without a column are similar to the values of VR column. What should be noted is the inclination of the consolidation curves in the model without column – at every level, it is flatter than in the DR and VR systems, which proves a lack of horizontal filtration in that system.

4. Numerical model of the system without column

In order to understand better the phenomena which occurred during laboratory tests, a numerical model of the test system was elaborated in FEM software Z-Soil. The form of laboratory system was used to create a numerical axi-symmetrical model which aimed at reflecting the course of the test performed without a column. The Coulomb-Mohr material model was applied, with Menetray-William (M-W) modification and non-associated flow rule [17]. Initial stresses were generated assuming normal soil consolidation. The calculations took into account soil deformation resulting from the initial consolidation. First of all, typical values of strength and shear parameters of soil, determined on the basis of laboratory tests, were used in the calculations. Then, by trial and error, some chosen parameters of the model were modified in order to obtain the same numerical consolidation curve as the one from laboratory tests.

Hundreds of analyses with various material parameters proved not enough to obtain a numerical curve which would be the same as the curve obtained in laboratory tests. On the other hand, three phenomena were identified:

- Non-linear elasticity: while the load was being placed on the soil in the laboratory, the soil behaviour was characterised by non-linear elasticity. Using the hyperbolic elastic model of Duncan-Chang [5], attempts were made to obtain results convergent with the first few minutes of laboratory test. Satisfactorily true results were obtained up to the point in which the last load was placed.
- Yielding: after the last load had been placed, a momentary but clear increase of settlement was noted which was disproportionate to the value of the applied load. It has been observed that some clay was pushed out through the space between the tube sides and the load's base, a few millimetres smaller in diameter. The soil yield. It was impossible to reflect these results in the Duncan-Chang model. The results obtained from the Coulomb-Mohr model (M-W) were not satisfactory either. Further analyses omitted the loading stage and tried to find similarities in other parts of the consolidation curve.
- Creep (secondary consolidation): numerical analyses of system deformations that only took into account the primary consolidation showed that the process ends much before the end of the test. The last sections of the consolidation curve are flat, the same as Terzaghi's theoretical curve of uniaxial consolidation [16]. Only after secondary consolidation (creep) in the logarithmic function [17] has been taken into consideration in the analyses, the results were convergent nearly on the entire consolidation curve. In Z-Soil system, according to the formula:

$$\varepsilon^{cr} = \varepsilon_{inst.}^e \cdot f(t) = \sigma C(t) \quad (1)$$

strain due to creep (ε^{cr}) is proportionate to temporary elastic deformations.

The function $C(t)$ described by the following formula was chosen for the model:

$$C(t, t_0) = A \cdot \ln(1 + Bt) \quad (2)$$

where:

- t_0, t – initial time of the analysis and the time in a particular computational stage,
- A, B – logarithmic function parameters, in this case, selected on the basis of backtracking.

The final result, in the form of superposed laboratory and numerical curves, is presented in Fig. 9.

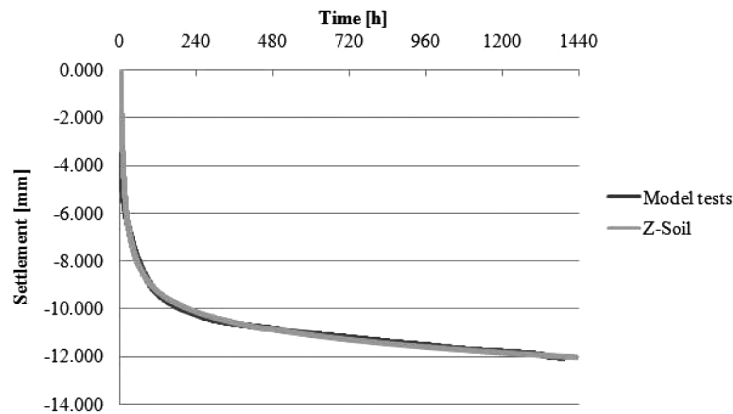


Fig. 9. Numerical and laboratory consolidation curves for the model without column

There are plans to perform a series of numerical analyses for systems with columns with the use of a numerical model calibrated in this way. The aim of such analyses will be to identify changes in horizontal and vertical filtration at every stage of the investigation.

5. Observations and conclusions

During the course of the research and the interpretations of the results, the author observed what follows and draws the following conclusions:

- In the described tests, no visible difference was observed in the course of the consolidation process of the column-weak soil system for the DR and VR columns. On the basis of small scale tests, can it be stated that the settlement value is determined by time, way of load placing, volume and density of drain material and not by the method of column formation. The author plans to conduct further research on a bigger scale that would permit drawing other conclusions.
- Investigations examining consolidation proved that the application of the DR and VR columns results in horizontal filtration occurring in the direction of the column. No quantitative conclusions could have been made due to the research scale which was too small. The similarity of the results for different models allowed only for qualitative conclusions.
- In similar investigations, insulation (e.g. using mineral wool) of the sides of the container in which tests are conducted should be considered. That would make laboratory conditions more similar to the conditions in situ, where the dynamic wave induced by the DR rammer drop may spread to long distances.
- Moisture tests showed only a little difference in consolidation of the two systems, which should be considered as negligible in designing. However, the analysis of processes occurring during the reinforcement construction clearly indicates tendencies to change.

- The importance of horizontal filtration was confirmed by differences in moisture values between the system without a column and two models with columns. Horizontal filtration will constitute the object of detailed analyses in future.
- The application of FEM allowed the identification of the processes occurring in the system without column during laboratory tests. The FEM software seems to be necessary to draw other conclusions from the investigations.

In further works, the author would like to find out what is the influence of the DR and VR column formation process on horizontal filtration in the vicinity of the column. The results of laboratory tests and numerical analyses for the DR column will be compared with analytical solutions which do not take into account the specificity of the DR method.

References

- [1] Asalemi Ali Amini, *Application of seismic cone for characterization of ground improved by vibro-replacement*, PhD Thesis, Teheran 2006.
- [2] Castro J., Sagaset C., *Consolidation around stone columns. Influence of column deformation*, International Journal for Numerical and Analytical Methods in Geomechanics, 33, 2009, 851-877.
- [3] Castro J., Sagaset C., *Deformation and consolidation around encased stone columns*, Geotextiles and Geomembranes 29, 2011, 268-276.
- [4] Dheerendra Babu M.R., Nayak S., Shivashankar R., *A critical review of construction, analysis and behaviour of stone columns*, Geotech Geol Eng, 2013, 1-22.
- [5] Duncan J.M., Chang C.Y., *Nonlinear analysis of stress and strain in soils*, Journal of the Soil Mechanics and Foundations Division, ASCE, 96 (SM5), 1970, 1629-1653.
- [6] Gryczmański M., *Methods of analyzing bearing capacity and settlements of soil strengthened with stone columns*, Inżynieria Morska i Geotechnika, Vol. 5, 1993, 224-231.
- [7] Hughes J.M.O., Withers N.J., *Reinforcing of soft cohesive soils with stone columns*. Ground Engineering, Vol. 7, No. 3, 1974, 42-49.
- [8] Kwiecień S., *Theoretical and experimental analysis of soil strengthening with the use of dynamic replacement method*, PhD Thesis, Politechnika Śląska, Gliwice 2008.
- [9] Kwiecień S., Sękowski J., *Stone columns formed with dynamic replacement technology*, Monograph, Wydawnictwo Politechniki Śląskiej, Gliwice 2012.
- [10] McCabe B.A., McNeil J.A., Black J.A., *Ground improvement using the vibro-stone column technique*, Paper presented at the Joint meeting of Engineers Ireland West Region and the Geotechnical Society of Ireland, NUI Galway, 15.03.2007, 1-12.
- [11] Priebe H., *The design of vibro replacement*, Technical Paper – reprint from Ground Engineering, 1995.
- [12] Sękowski J., Kwiecień S., *Dynamic replacement. Practical aspects of the use in roads engineering*, Magazyn Autostrady, Vol. 10, 2010, 24-128.
- [13] Sękowski J., Grzesik B., *Consolidation of subsoil reinforced with dynamic stone columns – laboratory tests*, Roczniki Inżynierii Budowlanej – Zeszyt 8/2008, 67-70.
- [14] Sękowski J., Grzesik B., *Influence of driven stone columns on water content of the strengthened subsoil*, Problemy geotechniczne i środowiskowe z uwzględnieniem podłoży ekspansywnych, Bydgoszcz 2009, 201-207.

- [15] Sękowski J., Kwiecień S., Kanty P., *The influence of the rammed stone kolumn formation on strength parameters of the surrounding soil*, *Budownictwo i Inżynieria Środowiska* 4/2013, 301-308.
- [16] Terzaghi K., *Erdbaumechanik auf Bodenphysikalischer Grundlager*, Deuticke Vienna, Austria 1925.
- [17] Zimmermann Th., Truty A., Podleś K., *Z_Soil.PC 2009 Manual*.

PAWEŁ KISIEL, ARKADIUSZ KWIECIEŃ*

NUMERICAL ANALYSIS OF A POLYMER FLEXIBLE JOINT IN A TENSILE TEST

ANALIZA NUMERYCZNA POLIMEROWYCH ZŁĄCZY PODATNYCH PODDANYCH ROZCIĄGANIU

Abstract

The paper presents an analysis of Polymer Flexible Joint behaviour in a tensile test. Three Finite Element Method models have been developed in order to compare numerical and laboratory test results. A discrepancy between laboratory test results and computational results obtained in models based on material parameters derived from polymer dumbbell test has been shown. This work also presents the influence of the choice of hyperelastic material model on calculations accuracy in Polymer Flexible Joint analysis.

Keywords: hyperelasticity, parameters identification, polymer flexible joint, tensile test

Streszczenie

W artykule przedstawione zostały wyniki analizy pracy Polimerowego Złącza Podatnego poddanego rozciąganiu. Wykonano trzy modele rozciąganego złącza za pomocą Metody Elementów Skończonych oraz porównano uzyskane wyniki numeryczne z rezultatami badań eksperymentalnych. Praca prezentuje rozbieżności pomiędzy wynikami bazującymi na parametrach materiałowych z jednoosiowego rozciągania próbki polimeru a wynikami z eksperymentów laboratoryjnych. W pracy przedstawiono również wpływ doboru modelu hipersprężystego na rozbieżności wyników obliczeń i testów laboratoryjnych.

Słowa kluczowe: hipersprężystość, identyfikacja, polimerowe złącza podatne, rozciąganie

* M.Sc. Paweł Kisiel, Ph.D., D.Sc. Arkadiusz Kwiecień, Institute of Structural Mechanics, Faculty of Civil Engineering, Cracow University of Technology.

1. Introduction

Polymer Flexible Joint (PFJ) technology is an innovative technology which allows for the carrying of loads with large deformations [1]. In particular, the PFJ can be used as a repair technology suitable for historic structures, for buildings located in seismic areas or to join concrete slabs in airfield pavements [2].

The development of guidelines for PFJ numerical modelling is a very important aspect of technology improvement. Consequently, there has been made an attempt to determine the material model for PFJ in tensile tests. There were obtained parameters for Mooney-Rivlin material model, representing polymer in joints basing on uniaxial test data. However, after numerical calculations performance of flexible joints with particular dimensions, there has been shown, that there is a significant discrepancy between calculated results and those obtained by an experiment, this can be observed in Fig. 1 [3].

The aim of this work is to analyse flexible joint behaviour under a tensile load, taking into account different specimens' geometry and various material models. The parameters of material are derived from the uniaxial polymer dumbbell test and they are identified for four different hyperelastic models. The results presented below clearly show that none of the material models correctly fits the PFJ behaviour in the tensile test.

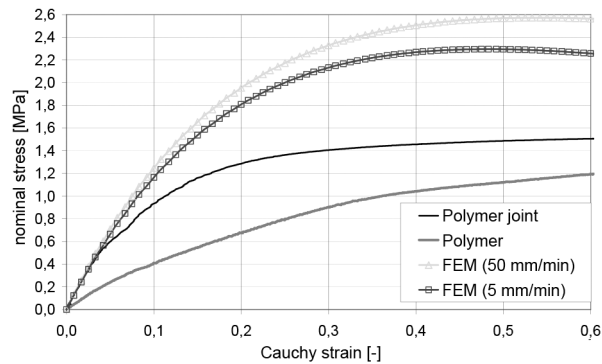


Fig. 1. Comparison of PFJ tensile laboratory test and numerical experiment results [3]

2. Description of experimental laboratory tests

Uniaxial tension tests were performed on 4 different types of specimens. First type was made of the PM-type polymer in a dumbbell shape, the other three types represent PFJ. Tests on the dumbbell shape specimens were performed according to [4]. Every specimen of PFJ consists of two concrete elements joined by a polymer layer. Schematic drawings of PFJ specimens are presented in Fig. 2. Tests on the PFJ specimens were performed according to own procedure.

Each concrete specimen was initially tested in the tensile test without the polymer layer to obtain correct data for numerical analysis. Subsequently, the test was performed for the PFJ specimens. The tensile tests were carried on ZWICK 1455 testing machine with maximum

force of 20 kN and precision of 0.1 N. There was used a mechanical extensometer of 0.005 mm precision. The tests were performed with displacement control of constant ratio of 50 mm/min. Sketch of the PFJ sample specimens are presented in Fig. 3.

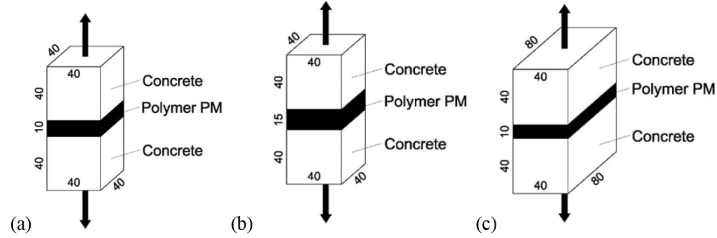


Fig. 2. Sketch of PFJ specimens with polymer joint dimensions: $40 \times 40 \times 10$ (a), $40 \times 40 \times 15$ (b) and $80 \times 40 \times 10$ (c)

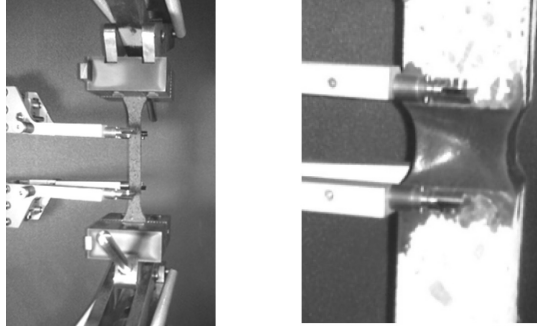


Fig. 3. Laboratory tests of polymer dumbbell specimens (on the left) and laboratory tests of PFJ (on the right)

3. Material parameters' identification

Material parameters identification has been performed basing on the Abaqus CAE 6.12 material property module. Tests data used for identification were obtained from the dumbbell tensile tests. There have been determined four different hyperelastic material models parameters. There are presented below analytical formulas for each applied material model.

– Mooney-Rivlin form – formula (1):

$$U = C_{10} (\bar{I}_1 - 3) + C_{01} (\bar{I}_2 - 3) + \frac{1}{D_1} (J^{el} - 1)^2 \quad (1)$$

where:

U – the strain energy per unit of reference volume,

C_{ij}, D_i – temperature-dependent material parameters;

\bar{I}_1, \bar{I}_2 – the first and second deviatoric strain invariants defined in formulae (2) and (3).

$$\bar{I}_1 = \bar{\lambda}_1^2 + \bar{\lambda}_2^2 + \bar{\lambda}_3^2 \quad (2)$$

$$\bar{I}_2 = \bar{\lambda}_1^{(-2)} + \bar{\lambda}_2^{(-2)} + \bar{\lambda}_3^{(-2)} \quad (3)$$

where:

$$\bar{\lambda}_1 = J^{-\frac{1}{2}} \lambda_i, J - \text{ the total volume ratio,}$$

$$J^{el} - \text{ the elastic volume ratio and } \lambda_i \text{ are the principal stretches.}$$

– 2nd order Polynomial form – formula (4)

$$U = C_{10}(\bar{I}_1 - 3) + C_{01}(\bar{I}_2 - 3) + C_{20}(\bar{I}_1 - 3)^2 + C_{02}(\bar{I}_2 - 3)^2 + C_{11}(\bar{I}_1 - 3)(\bar{I}_2 - 3) + \frac{1}{D_1}(J^{el} - 1)^2 \quad (4)$$

– Marlow form – formula (5)

$$U = U_{\text{dev}}(\bar{I}_1) + U_{\text{vol}}(J^{el}) \quad (5)$$

where:

$$U_{\text{dev}} - \text{ deviatoric part of } U,$$

$$U_{\text{vol}} - \text{ volumetric part of } U;$$

– 3rd degree Ogden form – formula (6)

$$U = \sum_{i=1}^N \frac{2\mu_i}{\alpha_i^2} (\bar{\lambda}_1^{\alpha_i} + \bar{\lambda}_2^{\alpha_i} + \bar{\lambda}_3^{\alpha_i} - 3) + \sum_{i=1}^N \frac{1}{D_i} (J^{el} - 1)^{2i} \quad (6)$$

where:

$$N - \text{ order of polynomial form,}$$

$$\mu_i, \alpha_i - \text{ temperature-dependent material parameters.}$$

Detailed explanation of the analytical formula can be found in [5] and discussion of the presented models in [6–9].

Obtained parameters values for Mooney-Rivlin material are relatively convergent with presented in [3]. They are equal to $C_{10} = 0.0119$ MPa and $C_{01} = 0.7901$ MPa, while parameters from [3] are equal to $C_{10} = 0.0195$ MPa and $C_{01} = 0.8305$ MPa for analysed load speed. The identified parameters of the models present good adjustment to the experimental results (Fig. 4).

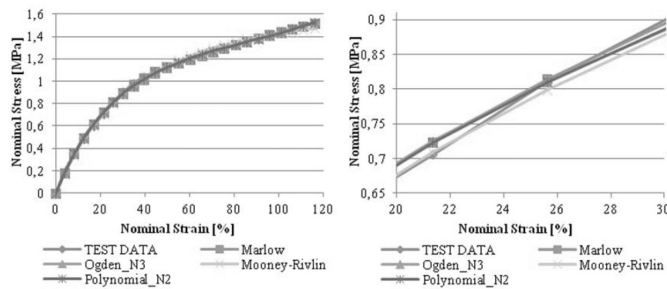


Fig. 4. Parameters identification in Abaqus 6.12, fragmentary enlarged graph on the right

4. Polymer model's verification

There has been performed a short analysis, in order to verify the polymer Finite Element Method (FEM) model as well as material models. A numerical FEM model in Abaqus 6.12 has been made for the dumbbell tensile test of the polymer PM and the determined model parameters have been used in analysis. The numerical model is characterized by following features:

- there have been used 25 600 3D elements – type C3D8H,
- only interior 8 cm of the dumbbell specimen has been modeled,
- there has been defined a displacement of boundary condition in order to compare properly calculation results with experimental test results.

The carried out calculations of the numerical model of the dumbbell specimen (for different hyperelastic models) allow determining the Cauchy stress map (Mises stress) calculated for the nominal strain $\epsilon = 30\%$ (shown in Fig. 5). The nominal stress – nominal strain curves, also determined for the considered hyperelastic models, present good results convergence, which can be noticed in Fig. 6.

Fig. 5. Cauchy stress distribution corresponding to the nominal strain of 30% in polymer verification of the FEM model of the dumbbell specimen

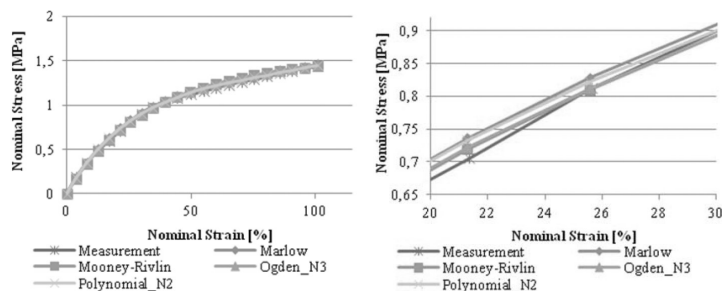


Fig. 6. Polymer model's verification, fragmentary enlarged graph on the right

The presented in Fig. 5 level of principal Cauchy stresses σ_1 (parallel to specimen's axis) can be compared with the value of the nominal stress (tensile force F divided by initial cross-section area S_0) corresponding to the nominal strain $\epsilon = 30\%$ (Fig. 6), only after recalculation [1] according to formula (7). This comparison manifests good adjustment (comp. Fig. 5), because the nominal stress of value 0.9 MPa correspond to the Cauchy stress value of 1.17 MPa.

$$\sigma_1 = \frac{F}{S_0}(1 + \epsilon) = (0.9 \text{ MPa}) \cdot (1 + 0.3) = 1.17 \text{ MPa} \quad (7)$$

5. PFJ numerical model description

All the numerical models of PFJ have been done using the FEM in Abaqus CAE 6.12. The dimensions and material parameters for the models have been defined in accordance with tests described above. The numerical models are characterized by following features:

- there have been used C3D8H elements for polymer and CRD8R for concrete,
- mesh density has been increased in the joint zone, specimens were modeled by 96 000 elements (for the biggest specimen),
- a contact layer has been modeled between specimen and reference rigid plane,
- there has been defined a displacement of boundary condition in order to compare properly calculation results with experimental test results. The boundary conditions were defined for rigid plane's reference points,
- concrete parameters were applied according to the carried out concrete tensile test and basing on Eurocode 2 [10]. Concrete was modeled as a linear-elastic material using parameters: $E = 32 \text{ GPa}$, $\nu = 0.18$, $\rho = 2400 \text{ kg/m}^3$.

6. Calculation results

There were considered 4 hyperelastic models (using the determined parameters for the dumbbell specimen) for 3 PFJ models (12 series of calculations). The obtained results for various hyperelastic models, calculated for the specimens presented in Fig. 2, are compared in Fig. 7 with the experimental data of the PFJ specimens. It can be noticed that the adjustment of the numerical analysis and laboratory test data is not very well.

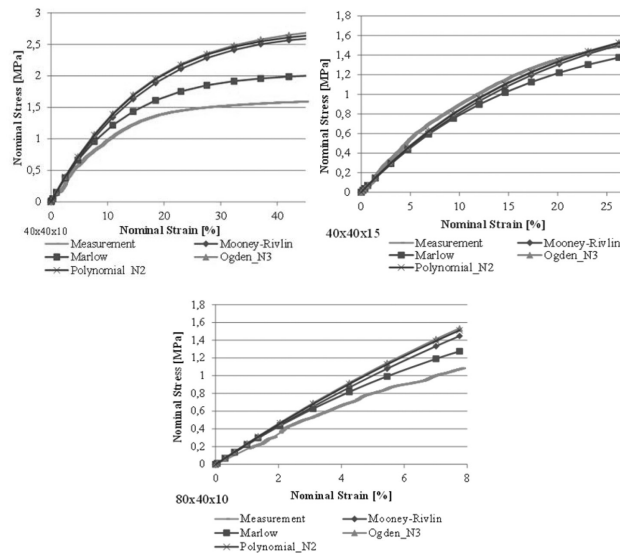


Fig. 7. Comparison of the numerical and laboratory tests results for $40 \times 40 \times 10$ (upper left), $40 \times 40 \times 15$ (upper right) and $80 \times 40 \times 10$ (bottom) PFJ variants

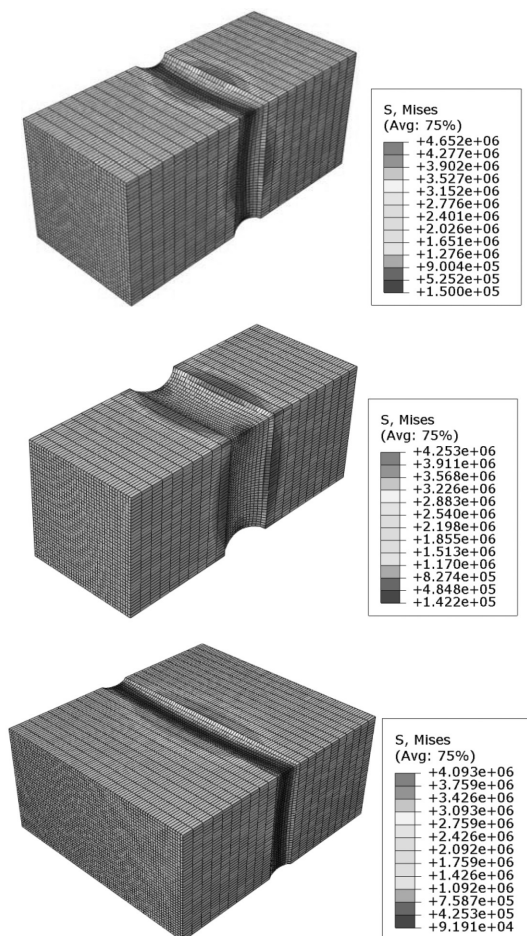


Fig. 8. Stress distribution for models with particular dimensions and nominal strain: $40 \times 40 \times 10$ and 30% (at the top), $40 \times 80 \times 10$ and 30% (in the middle), $40 \times 80 \times 10$ and 24% (at the bottom)

The calculated results for the PFJ models allowed also presenting maps of stress distribution in the considered models of the flexible joints, working under tensile stress (Fig. 8). It can be noticed that in the case of large deformations the stress distribution is complex and not evenly distributed at the interface between the concrete substrate and the polymer joint. It confirms also comparison of the stress distribution in the particular cross-section layers of the polymer PM (Fig. 9). In the middle layer, the stress is almost evenly distributed over the whole surface (with low intensity). On the other hand in the interface layer, peaks of stress concentrations (of high intensity) occur at the edges of the cross-section, whereas in the middle of the cross-section the stress is of low intensity. This conclusion was also confirmed by analysis presented in [1].

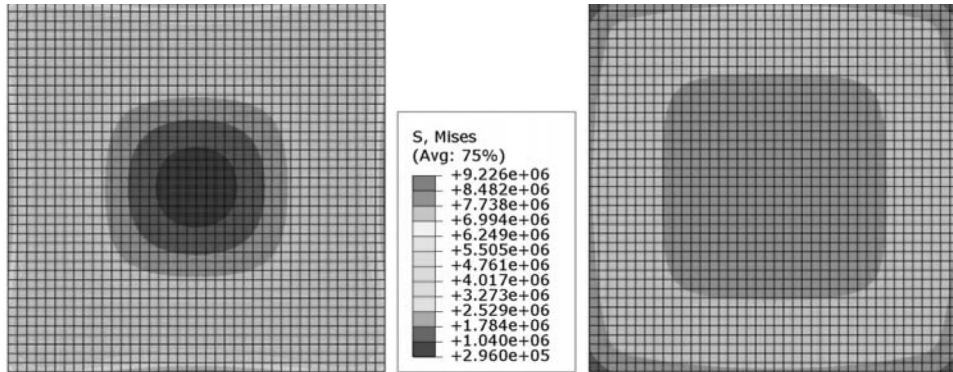


Fig. 9. Stress distribution in polymer layer at the interface between polymer and concrete (on the left) and in middle of the polymer layer cross-section (on the right)

6. Conclusions

Basing on the presented results following conclusions can be drawn:

- the hyperelastic material models, obtained during the uniaxial dumbbell tensile test is adequate for tensile calculations of a specimen made of polymer. However, using the same model in the PFJ calculations it leads to inaccuracies of about 30% or more,
- there is a big influence of the hyperelastic model type on results convergence; basing on this analysis it can be found that the Marlow form leads to smaller inaccuracy in analysed cases,
- both dimensions of specimens cross-section and polymer layer thickness influence the results' discrepancy. In presented example the highest convergence was obtained for specimen $40 \times 40 \times 15$, while for other specimens numerical models are characterized by a greater connection stiffness. At this point it is difficult to explain those results,
- laboratory as well as numerical test results lead to conclusion, that polymer's behaviour in the PFJ tensile test is more rigid than in the dumbbell one; the rigidity increase can be connected with complex stress state as well as shear effects in polymer layer next to the concrete surface,
- the pure adjustment of the PFJ model to the experiment results can be also connected with rheological behaviour, not included in these analyses.

This work indicates that PFJ theoretical model as well as numerical approach should be developed. As a continuation of this work, further laboratory tests as well as theoretical and numerical research will be performed in order to describe correctly the PFJ mechanical behaviour, including also rheological aspects.

References

- [1] Kwiecień A., *Polimerowe złącza podatne w konstrukcjach murowych i betonowych*. Monografia nr 414, Wydawnictwo Politechniki Krakowskiej, Seria Inżynieria Lądowa, Kraków 2012.
- [2] Kwiecień A., Gruszczyński M., Zając B., *Tests of flexible polymer joints repairing of concrete pavements and of polymer modified concretes influenced by high deformations*, Key Engineering Materials Vol. 466 (2011), Trans Tech Publications 2011, 225-239.
- [3] Kwiecień A., Kuboń P., Zając B., *Experimental verification of hyperelastic model of polymer on a case study of the flexible polymer joint*, Zeszyty Naukowe Politechniki Rzeszowskiej nr 276. Budownictwo i Inżynieria Środowiska, Zeszyt 58 nr 3/2011/II, 373-380.
- [4] PN-EN ISO 527-1: 1998 *Tworzywa sztuczne – Oznaczanie właściwości mechanicznych przy statycznym rozciąganiu – Zasady ogólne*.
- [5] Abaqus Theory Manual, Abaqus On-line documentation, <http://baribal.cyf-kr.edu.pl:2080/v6.7>
- [6] Weber G., Anand L., Finite deformation constitutive equations and a time integration procedure for isotropic, hyperelastic-viscoplastic solids. *Computer Methods in Applied Mechanics and Engineering*, 79 (1990), s. 173–202.
- [7] Kaliske M., Rothert H., *On the finite element implementation of rubber-like materials at finite strains*. *Engineering Computations* 14, 1997, 2, 216–232.
- [8] Aidy A., Hosseini M., Sahari B.B., *A review and comparison on some rubber elasticity models*, *Journal of Scientific and Industrial Research*, 69, 2010, 495-500.
- [9] Jemioło S., *Studium hipersprężystych własności materiałów izotropowych: Modelowanie i implementacja numeryczna*, *Prace naukowe, Budownictwo, OWPW, Warszawa 2002*.
- [10] Ajdukiewicz A., *EUROKOD 2. Podręczny skrót dla projektantów konstrukcji żelbetonowych*, Stowarzyszenie Producentów Cementu, Kraków 2009.

DOROTA MIROSŁAW-ŚWIĄTEK, MARIA MERKEL, WITOLD GIŻYŃSKI*

APPLICATION OF THE FILTRATION NUMERICAL MODEL FOR THE ASSESSMENT OF THE EFFECTIVENESS CUT OFF WALLS IN LEVEES

ZASTOSOWANIE NUMERYCZNEGO MODELU FILTRACJI DO OCENY EFEKTYWNOŚCI PRZESŁON HYDROIZOLACYJNYCH W WAŁACH PRZECIWPOWODZIOWYCH

Abstract

In this paper, a two-dimensional numerical model of filtration was used to evaluate the effectiveness of cut off walls constructed in DSM and WIPS technology. Numerical calculations were performed for a steady state water flow through the body and the base of the levee. On the basis of these simulations results, an assessment of the effectiveness of these cut off walls was made.

Keywords: cut off walls, levee, FEM

Streszczenie

W artykule do oceny efektywności przesłon hydroizolacyjnych wykonywanych w technologii DSM i WIPS zastosowano dwuwymiarowy numeryczny model filtracji przez korpus i podłoże obwałowania. Obliczenia numeryczne wykonano dla stanu przepływu ustalonego wody przez korpus i podłoże wału. Na podstawie wyników symulacji dokonano oceny efektywności tych przesłon.

Słowa kluczowe: przesłona hydroizolacyjna, wał przeciwpowodziowy, MES

* Ph.D. Dorota Mirosław-Świątek, M.Sc. Eng. Maria Merkel, M.Sc. Eng. Witold Giżyński, Instytut Meteorologii i Gospodarki Wodnej, Państwowy Instytut Badawczy.

1. Introduction

The purpose of levees is protecting the adjacent areas from flooding. The geometry and soil configuration of the levee must be properly selected so that the structure is safe in terms of stability and filtration. Proper levee construction should take into account the correct height, preventing overflowing during peak flows and considering wave accumulation caused by wind or embolic events (e.g. freezing). One of the hydraulic conditions for levees, which should always be met, is preventing the free flow of water on the downstream slope. Unfavorable soil configuration in the levee's cross section when a permeable soil (e.g. sand) is placed on the upstream side and a poorly permeable soil (e.g. clay or clayey sand) on the downstream slope causes an increase in hydraulic pressure inside a levee's body. During intensive and long-lasting floods, this state enables the formation of leaks on the downstream slope. A high level of water pressure inside the levee's body can cause dangerous suffosive outflows. This phenomenon may appear on the downstream slope, at the toe, or in the adjacent area. The long term persistence of such a state can therefore lead a levee to break. Considering stability and proper filtration, it is preferred that the full saturation area of the levee's body was as small as possible and located as low as possible. It is assumed that the water table should not be closer to the downstream slope than 1 m, this can be achieved by means of appropriate drainage systems [1]. The important matter is the height of water pressure in the base. During flood events, the most beneficial is the water pressure distribution to be similar to the conditions found before this period, i.e. approximate to the natural conditions.

One of the methods to repair levees is to form vertical cut off walls along their body, eliminating or reducing unwanted water filtration and increasing the stability of levees. These diaphragms are created through various methods using special hardening mineral slurries. These are primarily sheet piling in narrow trenches, vibration-grouting slit diaphragms (WIPS) and the palisade of deep-mixed soil columns (DSM).

Filtration analysis in levees should be considered using an unsteady state water flow model in porous media, because its course mainly depends on the time-varying wave hydrograph of a river. [4–5]. In recent years, both in the Vistula and the Oder catchment area, there has been an increase of long-lasting floods distinctive by two peak points several days apart [2–3]. This situation causes a long lasting high water saturation of the levee. Under these hydrological conditions, the effectiveness of cut off walls may be analysed in steady state conditions resulting from a long-lasting high water level in the river. The research was performed on a selected section of the right Warta River levee located in the village of Kostrzyń.

2. The study area

2.1. Specification of the selected section of the levee

A generalized cross-section of the levee was assumed for the purpose of model studies. The most unfavorable was considered to be the one with the smallest width of the base with the following parameters: height 3.20 m, width 28.60 m. The levee has no drainage facilities and did not have any cut off facilities until this project.

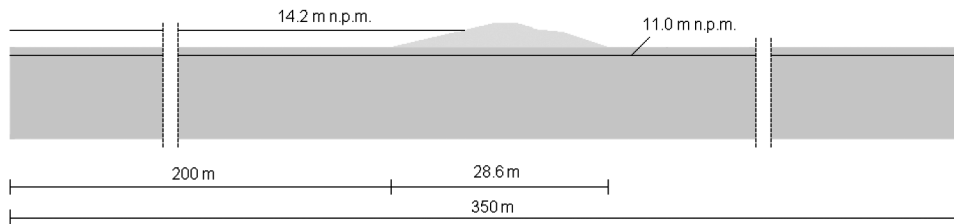


Fig. 1. Filtration area outline

The average distance between the levee and Warta River in this area is about 200 m. The elevations on both sides of the levee vary between 11.5 and 13.0 m a.s.l. In the immediate vicinity of the levee it is about 12 m a.s.l. During the geotechnical investigations, where the maximum drilling depth amounted to 10 m, the impermeable layer was not found. According to the Polish Hydrogeological Atlas of 1993 [5] on a scale of 1:500 000 the depth of a first aquifer in the vicinity of Kostrzyń is up to 15 m. The filtration model assumes that the impermeable layer is at elevation 0 m a.s.l. The elevation of the groundwater table at the start of the flood is 11 m a.s.l., which is 1 m below the surface, and the maximum flood level is at elevation 14.2 m a.s.l., which is 1 m below the levee's crest. The total length of the filtration area is 350 m (Fig. 1).

The conducted geotechnical investigation has shown that the study area consists of accumulation of river. These are predominantly fine sands with inclusions of sandy silt with an organic content in the range of 5 to 15%. Through these materials, water filtrates in numerous places. As a result of these studies three, geotechnical layers were marked out:

- I – constructional embankment, which consists of the levee body,
- II – sands representing the aquifer,
- III – silty sands interbedding the aquifer.

The values of hydraulic conductivity for each layer and for the materials forming cut off walls were obtained from geotechnical investigations and are shown in If it is necessary to strengthen the levee and improve its filtration properties, a popular solution is to create vertical cut off walls. These are primarily sheet piling in narrow trenches, vibration-grouting slit diaphragms (WIPS) and the palisade of deep-mixed soil columns (DSM) [6].

Table 1 [6].

Three different stratifications were distinguished for the examined levee based on geotechnical documentation, all with a homogeneous body but a slightly different foundation:

- KP – homogeneous sands disregarding the silty inclusions considering their mild effect on the formation of the groundwater head;
- KPHI – homogeneous aquifer with a 0.5 m layer of silty sands lying directly beneath the surface;
- KPHII – homogeneous aquifer with a layer of silty sediments 20 m wide with a maximum depth of 1 m located centrally with respect to the embankment crest.

If it is necessary to strengthen the levee and improve its filtration properties, a popular solution is to create vertical cut off walls. These are primarily sheet piling in narrow trenches, vibration-grouting slit diaphragms (WIPS) and the palisade of deep-mixed soil columns (DSM) [6].

The values of hydraulic conductivity

Layer	hydraulic conductivity [m/s]
Constructional embankment [I]	6.0E-05
Aquifer [II]	1.5E-05
Silty sands [III]	4.0E-07
Cut off wall – DSM	4.0E-08
Cut off wall – WIPS	6.0E-10

2.2. Cut off walls

A variation of the method of implementation of diaphragm walls is the WIPS technology, which is based on forming a narrow trench (usually not wider than 20 cm) by inserting with vibrations a steel profile provided with nozzles on the bottom for applying a hardening slurry. After achieving the desired depth, the profile is pulled upwards with the simultaneous administration of adhesive, which fills the gap. The continuity of the diaphragm is obtained by performing successive plunging of the profile, partially overlapping. Once the adhesive hardens, the parameters of the obtained diaphragm are similar to the walls constructed in narrow trenches. In both cases, the advantage is the applicability in soils with organic content, due to the lack of mixing of the adhesive with the surrounding soil and groundwater.

Cut off walls using the DSM technology are constructed using drills equipped with mixers shaped as plate augers with nozzles for the mineral adhesive application. The process involves mechanical drilling without excavation, with the simultaneous administration of the adhesive. After achieving a desired depth, the soil is then mixed several times with the adhesive by repetitive raising and penetration. This results in a formation of a pile made of soil particles permanently combined with the hardened adhesive. By carrying out subsequent, partly overlapping piles, a continuous diaphragm is obtained with the parameters dependent on the adhesive used. This method works well in ground improvement by using cemented piles. In the case of cut off walls where excessive rigidity of the piles is not desired, clay or loam instead of cement is used as a base for slurries. Its efficiency is then dependent on the type and the physico-chemical properties of the soil that is to be treated. A significant disadvantage of the DSM method is the difficulty of maintaining proper vertical drilling at greater depths, which may lead to a lack of continuity of the diaphragm in the lower part.

A finished diaphragm, regardless of the implementation method, should have a hydraulic conductivity of about 10^{-7} – 10^{-10} m/s, dissolving resistance to water and compressive strength not exceeding 1 MPa, so that the material retains sufficient flexibility to guarantee good cooperation with deformations in the ground. Therefore, adhesives based on loam are preferred with a small addition of cement as a binder.

3. Methodology

The GMS/SEEP2D numerical modeling system was used in the flow calculation through a cross-section of the river levee. This software was developed to model a variety of problems involving steady state of seepage [8]. The SEEP2D model is based on the following equation:

$$\frac{\partial}{\partial x} \left(K_{xx} \frac{\partial h}{\partial x} + K_{xy} \frac{\partial h}{\partial y} \right) + \frac{\partial}{\partial y} \left(K_{yx} \frac{\partial h}{\partial x} + K_{yy} \frac{\partial h}{\partial y} \right) = 0 \quad (1)$$

where:

h – total head (elevation head plus pressure head),

K – hydraulic conductivity.

The following conditions can be modeled using SEEP2D: isotropic and anisotropic soil properties; confined and unconfined flow for profile models; saturated/unsaturated flow for unconfined profile models; confined flow for plan (areal) models; flow simulation in the saturated and unsaturated zones; heterogeneous soil conditions; axisymmetric models such as flow from a well; drains.

In the model, a finite element method (FEM) is used for solving the governing equation (1) and the region being modeled is represented by a finite element mesh. Boundary conditions are typically entered as constant head at the node, the head equals the elevation (exit face) at a node, or as an incoming flux at a node or along an element edge. Exit face boundary conditions are used when modeling unconfined flow problems and should be placed along the face where the free surface is likely to exit the model. The SEEP2D program can calculate the head, flow, discharge (Darcian) velocity, and pore pressure at every node in the mesh.

In the elaborated model, an unconfined flow through a levee is simulated as a flow in both the saturated and unsaturated zones with isotropic soil properties. The hydraulic conductivity in the unsaturated zone is calculated using the Van Genuchten method.

Vertical cut off walls are presented in the model as soil layers in the filtration area with specified parameters (Table 1). In the chosen cross-section of the levee, on the boundary between the levee and the river a Dirichlet boundary condition is given with a total value of H , which corresponds to the water level in the stream. Exit face boundary conditions are used on the downstream slope and the downstream surface area.

4. Results

The filtration calculations were performed for two cut off wall location variations and for the actual situation (KP model), which reflects the current state of the levee. In the first model (P) both cut off walls are located in the centre of the levee's body (Fig. 2).

In the second case (GP), the cut off walls are located in the upstream slope near the toe of the levee and interact with an impermeable membrane (Fig. 3). The minimum distance between the geomembrane and the upstream slope surface should be 1 meter and the inclination of the upstream slope should be milder than the one of the geomembrane. In both cases, the cut off walls reach a depth of 9 m below the surface.

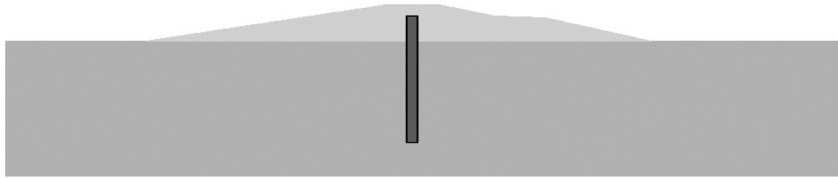


Fig. 2. 'P' model representing the levee with a cut off wall located in the centre

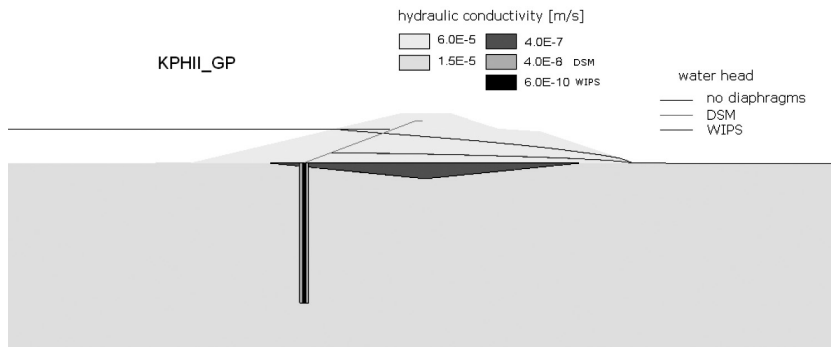


Fig. 3. 'GP' model representing the levee with a cut off wall located in the upstream slope and interacting with an impermeable membrane

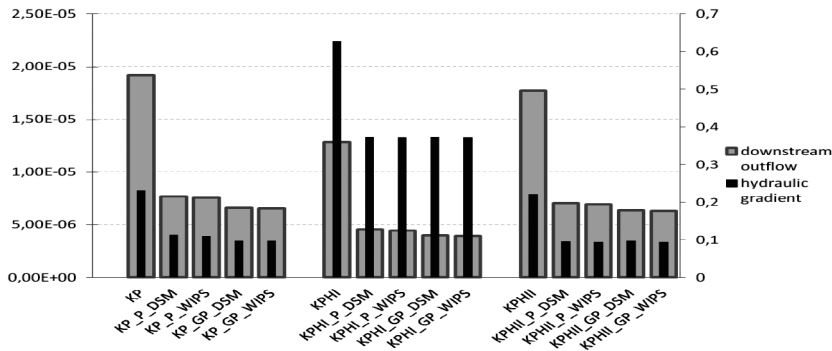


Fig. 4. Water head position with and without diaphragms on the upstream side interacting with a membrane (GP) for a homogeneous foundation model with a layer of silty sediments 20 m wide (KPHII)

The position of the water head in the body of the levee was calculated for all possible combinations of foundation, cut off wall position and technology (18 in total). As a result, it was shown that for a steady state water flow, the water head position is independent of the technology that the cut off wall was constructed in. For all foundation models, the groundwater head in the levee was almost the same for cut off walls made with WIPS and DSM technology. As an example, Fig. 4 shows the calculation results for the KPHII foundation

model with the diaphragm interacting with a membrane. It is also clear that the diaphragm located in the upstream area and interacting with a membrane lowers the groundwater head sooner, influencing a decrease in the total water content in the levee's body.

For effective assessment of the cut off walls, an analysis of other parameters was taken into account, namely, the hydraulic gradient in the downstream toe area and the intensity of the water outflow downstream. Fig. 5 confirms that for all foundation models, locating the cut off wall on the upstream side interacting with a geomembrane give slightly better results in terms of limiting filtration. Table 2 presents the percentage values of these parameters, where 100% correspond to the initial situation without any diaphragms in the levee.

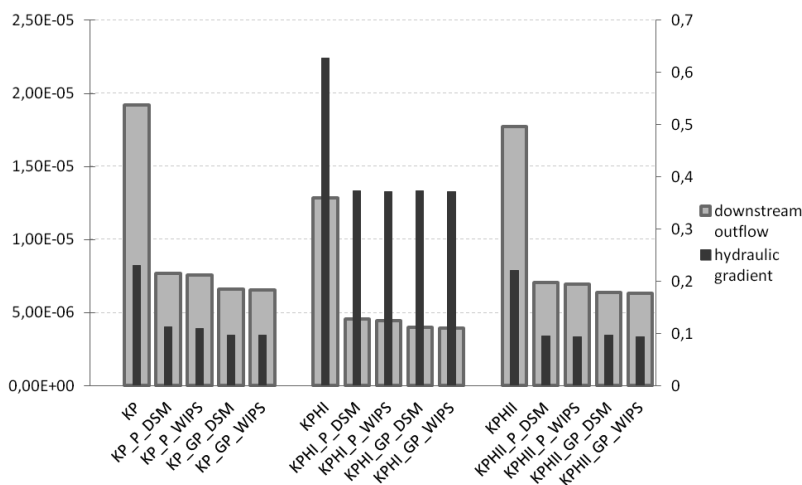


Fig. 5. Downstream outflow and hydraulic gradient change analysis after construction of DSM and WIPS cut off walls

Table 2

Effectiveness of cut off walls for different locations, foundation models and technologies

Numerical model	Downstream outflow reduction effectiveness		Hydraulic gradient reduction effectiveness	
	DSM	WIPS	DSM	WIPS
KP_P	48%	48%	40%	39%
KP_GP	42%	42%	34%	34%
KPHI_P	60%	59%	36%	35%
KPHI_GP	60%	59%	31%	31%
KPHII_P	43%	43%	40%	39%
KPHII_GP	43%	44%	36%	36%

5. Conclusions

The calculations of steady state seepage for the selected section of a levee on the Warta River in the area Kostrzyń allow for the drawing of the following conclusions:

- Cut off walls constructed in the WIPS or DSM technology can be successfully included in a numerical model of filtration through a levee as areas of a particular geometry and a known hydraulic conductivity.
- None of the diaphragms regardless of technology used and the location does not eliminate the free water outflow on the downstream side of the levee, however they all prevent the water from flowing through the downstream slope.
- Cut off walls made in the same location using different technologies give very similar results in terms of the position of the groundwater table and reducing the hydraulic gradient and the outflow on the downstream side.
- The cut off walls located near the upstream slope and interacting with an impermeable geomembrane proved to be more effective than the ones located in the centre of the levee.
- Each case related to flood security and solutions offered must be considered individually, so that the effectiveness of the proposed protection system is optimized for the given conditions.
- Simulations should be performed for several variations of the proposed flood protection to assess their effectiveness and select the optimal technical solution to eliminate irregularities in the course of filtration.

This paper is a result of a project conducted by Przedsiębiorstwo Robót Geologiczno-Wiertniczych called Application of ultrafine clay-based adhesives to construct cut off walls under the Sectoral Operational Programme “Improvement of the Competitiveness of Enterprises, years 2004–2006” also known as EU FOR THE ENTREPRENEURIAL – “PROGRAMME COMPETITIVENESS”.

References

- [1] Bednarczyk S., Mackiewicz S., *Powodzie w Polsce i skuteczność ochrony przeciwpowodziowej*, Inżynieria Morska i Geotechnika, nr 2, 1998, 55.
- [2] Maciejewski M., Ostojski M.S., Tokarczyk T., *Monografia powodzi 2010. Dorzecze Odry*, IMGW, Warsaw 2011.
- [3] Maciejewski M., Ostojski M.S., Walczykiewicz T., *Monografia powodzi maj–czerwiec 2010. Dorzecze Wisły*, IMGW, Warsaw 2011.
- [4] Makowski R., Popielski P., *Wykorzystanie terenowych badań geofizycznych i modelowania numerycznego do oceny zmodyfikowanych wałów przeciwpowodziowych*, Zapory – bezpieczeństwo i kierunki rozwoju, Warsaw 2013.
- [5] Mirosław-Świątek D., *Zastosowanie modelu numerycznego filtracji do określenia efektywności zabezpieczeń przeciwfiltracyjnych wałów przeciwpowodziowych*, IMGW, Materiały Badawcze (13), Seria Inżynieria Wodna, Warszawa 2002.
- [6] Mirosław-Świątek D., Zielińska M., Giżyński W., *Opracowanie modelu matematycznego filtracji dla różnych konstrukcji hydrotechnicznych w których zaprojektowano przesłony hydroizolacyjne*, Project Report on Application of ultrafine clay-based adhesives to

construct cut off walls, Institute of Meteorology and Water Management in Warsaw Dams Monitoring Centre, 2008.

- [7] Paczyński B., *Atlas hydrogeologiczny Polski: Systemy zwykłych wód podziemnych*, Państwowy Instytut Geologiczny, 1993.
- [8] *Groundwater Modeling System SEEP2D PRIMER*, Brigham Young University, Engineering Computer Graphics Laboratory, 1999.

PAWEŁ POPIELSKI*, SEBASTIAN KOWALCZYK**, RADOSŁAW MIESZKOWSKI**,
MAREK CHADAJ***, MICHAŁ KRYSIAK***, BŁAŻEJ SMOLIŃSKI****

THE APPLICATION OF GEOPHYSICAL METHODS AND NUMERICAL MODELING FOR THE EVALUATION OF EMBANKMENT TECHNICAL CONDITIONS

ZASTOSOWANIE METOD GEOFIZYCZNYCH I MODELOWANIA NUMERYCZNEGO DO OCENY STANU TECHNICZNEGO WAŁÓW PRZECIWPOWODZIOWYCH

Abstract

The paper focuses on selected geophysical methods, which may be applied for the evaluation of the technical conditions of flood banks. The paper presents and discusses results of geophysical tests (refractive seismic, geo-radar, vertical electrical sounding and electrical resistivity tomography) obtained from the Kobylnica research test site, i.e. for parts of flood banks on the Vistula River in the Mazovia Region. For a part of the flood bank, where geophysical anomalies were presented, and where cones of hydraulic leakages were observed, numerical calculations of the filtration processes (suffosion) were performed. The obtained results of the geophysical investigations were compared with geotechnical investigations.

Keywords: Geophysical Methods, Electrical Resistivity Tomography (ERT), Ground Penetrating Radar Method (GPR), Vertical Electrical Soundings (VES), refractive seismic, numerical modelling, suffosion

Streszczenie

W artykule skoncentrowano się na wybranych metodach geofizycznych, które można zastosować do oceny stanu technicznego wałów przeciwpowodziowych. Przedstawiono i zinterpretowano wyniki badań geofizycznych (sejsmiki refrakcyjnej, georadaru, pionowych sondowań elektrooporowych oraz tomografii elektrooporowej) uzyskanych z poligonu badawczego Kobylnica, tj. fragmentów wałów przeciwpowodziowych na rz. Wiśle na Mazowszu. Dla fragmentu wału przeciwpowodziowego, gdzie wskazano anomalie geofizyczne oraz wcześniej wykryto strefy przebieg hydraulicznych, wykonano obliczenia numeryczne procesów filtracyjnych (sufozji). Uzyskane wyniki badań geofizycznych skonfrontowano z wynikami badań geotechnicznych.

Słowa kluczowe: metody geofizyczne, tomografia elektrooporowa (ERT), metoda georadarowa (GPR), metoda pionowych sondowań elektrooporowych (VES), tomografia sejsmiczna, sejsmika refrakcyjna, modelowanie numeryczne, sufozja

* Ph.D. Paweł Popielski, Institute of Water Supply and Hydrological Constructions, Faculty of Environmental Engineering, Warsaw University of Technology.

** Ph.D. Sebastian Kowalczyk, Ph.D. Radosław Mieszkowski, Institute of Hydrogeology and Engineering Geology, Faculty of Geology, University of Warsaw.

**** Marek Chadaj, Eng. Michał Krysiak, Eng. Błażej Smoliński, Faculty of Environmental Engineering, Warsaw University of Technology, Scientific Circle of Water Engineering.

1. Introduction

Phenomena of filtration, moistening or loosening of grounds in the body of a flood bank are well visible during periods of rising waters or floods. Observations performed in this field are highly valuable for the evaluation of the technical conditions of flood banks. The possibility of locating such phenomena during other periods is complicated, since some defects are not visible from the terrain surface. The important parameters which influence the quality of the flood banks are its stability, impermeability and the quality of its foundations. The important issue concerns inspections of the technical conditions and safety of flood banks. Investigations performed with the use of geophysical methods have recently become more important. Such methods allow for pointing to weakened places within the investigated structure of the flood bank, where more detailed geotechnical tests should be performed. Such tests are non-invasive into the tested medium, their costs are low and a relatively short time is required to obtain the results of such tests. Geophysical methods were, among others, recommended as dedicated methods for the detection and observations of internal erosion processes [3].

At present, geotechnical methods such as dynamic soundings (Dynamic Probing Light), soundings (Cone Penetration Test) and small-diameter drillings, are the most important methods of investigation of the technical conditions of flood banks in Poland. Such approaches allow for stating whether the ground is soaked with water or whether it is compact or characterised by the high porosity in a given place. It is an effective test, but to perform it in places located within long distances may result in overlooking in the structure of flood banks.

Investigations of technical conditions of flood banks are more efficient when monitoring using geophysical methods are performed prior to preparation of geotechnical documentation. Geophysical methods allow for continuous, instrumental observations (2D or 3D) of the flood banks and its foundations based on changes in the physical parameters of embankment grounds, such as electric resistance, the dielectric constant, the velocity of seismic waves propagation etc. This means that measurements are not performed at given points, but instead, they are made along measuring lines. Therefore, it is possible to initially point, basing on geophysical anomalies, to places which are potentially threatened by breakdowns and to continue geotechnical investigation and strengthening of these places. The important advantage of these investigations concern their non-invasive characteristics. When investigations are performed using these methods, there is no physical intervention in the construction of banks.

This paper presents results of geophysical investigations performed in 2012 for the selected test site, *Kobylnica*. The obtained results of geophysical investigations were compared with the results of geotechnical investigations, performed in 2011, within the Rector's Grant of the Warsaw University of Technology, *Analysis of possibilities to utilise geophysical surface seismic methods for evaluation of technical conditions of flood banks*. Comparison of the results of investigations allowed for the determination of the correctness of results obtained with the use of geophysical methods and for evaluation of their accuracy. Based on the results of geophysical and geotechnical investigations, numerical modelling of the stability of escarpments of flood banks, as well as processes of filtration within the banks and under them, with consideration of the high water level in the river bed, was performed [5].

2. Description of a flood bank within the Kobylnica research test site (43+285 km)

The works were focused on the selected research test site, i.e. the part of the flood bank on the Vistula River, located south of Warsaw, in Kobylnica. This location was selected because of alarming events, which were observed on the flood bank and in its foundation during the flood of 2010. They included transudation through the flood bank body and hydraulic leakages in the bank foundation. The location of the test site is presented in Fig. 1.

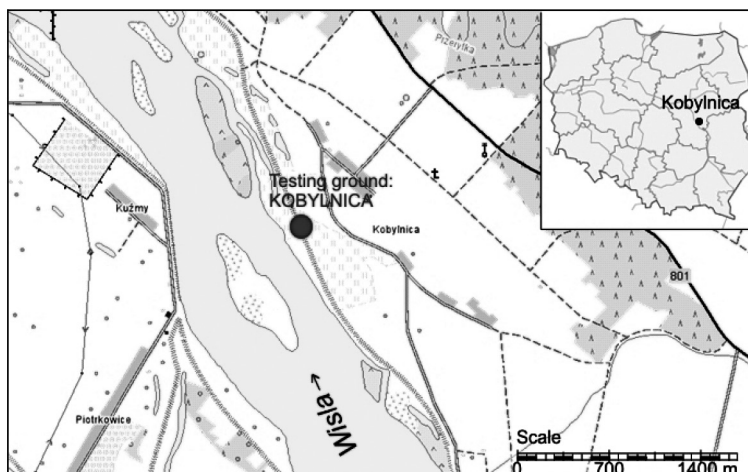


Fig. 1. A map presenting the location of the Kobylnica research test site (www.geoportal.gov.pl)

The flood banks within the area of Kobylnica are hydrotechnical structures of the 2nd class. They were modernised in 2007. The characteristic feature of this area is the close neighbourhood of old river beds and marginal lakes both located between the banks and behind them. The body of the flood bank is constructed of materials which are available locally, i.e. fine and dusty sand, with dust and clay. Although refurbishment works were performed, which included construction of the anti-filtration diaphragm in the flood bank body with a thickness of 15 cm and a depth of 7 m, suffosion phenomena was observed during the flood of 2010. It could be noticed in the form of the zones of water outflows close to the bank foundation, on the back side of the bank. This phenomenon is presented in Fig. 2.

The following investigations were performed within the Kobylnica test site:

- 1) borings to the depth of 6 m, DPL, Multichannel Analysis of Surface Wave (MASW) Continuous Surface-Wave System (CSWS) (2011 r.) [1, 4],
- 2) *vertical electrical soundings (VES)*, *electrical resistivity tomography (ERT)*, ground penetrating radar (GPR) and refractive seismic [5].

The objective of these investigations was to determine the physical and mechanical parameters of the ground and types of geophysical anomalies at the place of existing suffosion phenomenon and weakening of the flood bank. The location of the performed works is presented in Fig. 4.



Fig. 2. Suffusion phenomena close to the bank foot, the area at the back of the flood bank, Kobylnica 2010 (photo. M. Marszałek)

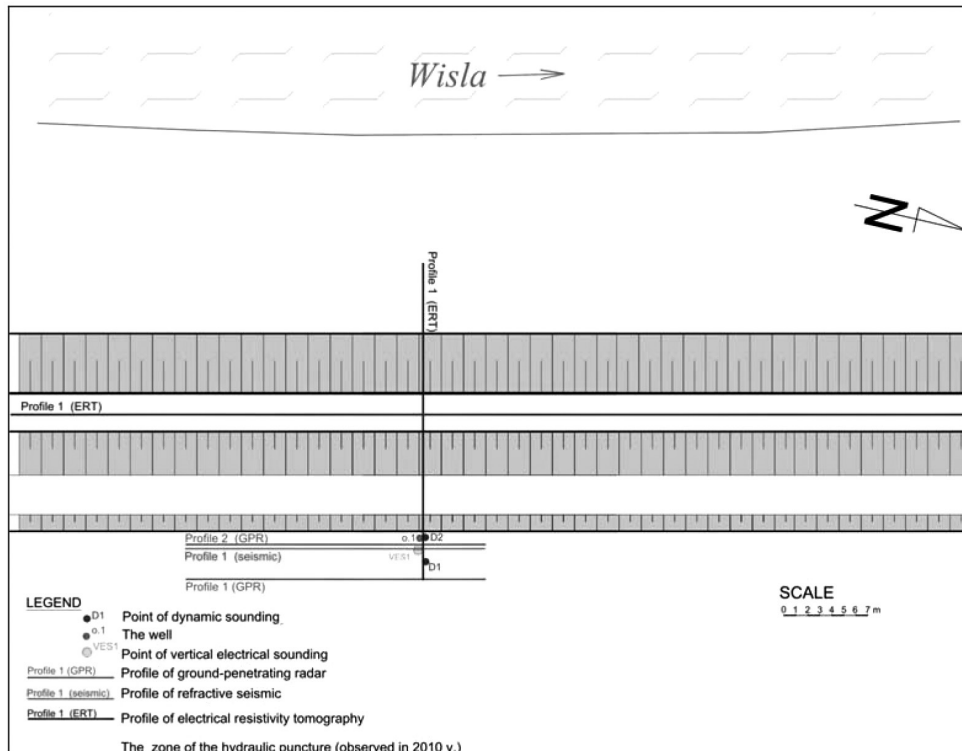


Fig. 3. A documentary map of geotechnical and geophysical tests

3. Geophysical tests

3.1. Vertical electric resistivity soundings

Assumptions of the method of vertical electrical soundings (VES) were formulated at the beginning of the 20th century by two brothers, Conrad and Marcel Schlumberger. The theoretical description may be found, for example, in [9, 16]. In general, this method is aimed at observations of properties of the electric field, which is artificially generated in the soils by a system of electrodes. This method is used for measurements of the apparent resistivity of soils which occur within the generated field. Basing on these measurements, the way of location of soils, which differ in the ability to conduct the electric current, is interpreted in the 1D system.

3.2. Electric resistivity tomography (ERT)

The method of the electric tomography (ERT) was developed at the end of the 20th century; it has been widely discussed, for example in: [6, 10–12]. This method is performed in such a way that it allows for recognition of the distribution of electric resistivity in the soils, in the 2D and/or 3D system. The Terrameter LS, produced by ABEM from Sweden, was utilised for investigations of the electric resistivity performed within the discussed works.

3.3. The ground penetrating radar method

The concept of geophysical investigations performed with the use of ground penetrating radar systems is based on reflection of high frequency electromagnetic waves emitted by special transmitting antennas into the geological medium. The issue of geo-radar investigations is widely discussed in [7, 8, 10].

In total, 20 geo-radar profiles were performed in the selected test site shield antennas of frequency 250 MHz were used for this purpose. For further discussions in this paper, two selected profiles have been used which were characterised by highly visible anomalies. In order to perform investigations using radar profiling, the universal RAMAC GPR system, produced in Sweden by Mala GeoScience, was used. The maximum range of depths of investigation for the existing geological conditions, was equal to almost 5 m.

3.4. The refractive seismic method

The physical basis for the utilisation of seismic measurements in geological-and-geotechnical prospecting is the relationship between the velocity of seismic waves, which propagate within the medium and mechanical parameters of this medium, which are connected with lithology, the level of densification or the level of damages of the primary structure of the medium [16].

Seismic refraction investigations use refractive seismic waves, i.e. waves refracted under the limit angle, at the border of two media, out of which the lower located medium is characterised by greater velocities of seismic waves. Measurements were performed using the profiling method of the length of 21 m (distances between geophones every 1 m). Seismic waves were generated at both of ends and along its length, spaced every 2–3 geophones). The applied methodology of measurements allowed for detailed diversification of the velocity of seismic waves in the subsurface layers of sediments, in the foundation of the flood bank. Calculations were performed with the use of ReflexW, the licensed software package. Seismic waves were generated percussively by using the 8 kg hammer. The registration of vibrations was performed using geophones of 28 Hz frequency and the seismic installations DMT Summit, with digital recording and the possibility to sum up the energy of seismic vibrations.

4. Results of geophysical testing

Data obtained from geophysical tests were processed and interpreted. Results were presented in the form of diagrams and cross-sections with appropriate descriptions.

4.1. The vertical electrical soundings

The paper presents results of one sounding operation (VES) which was performed close to the zone of the hydraulic leakage (location: Fig. 4). Sounding was performed in the Schlumberger system. The estimated range of prospecting was equal to approx. 8 m below the terrain surface. Measurements were performed using the PMG102 device; the DC converter of the voltage up to 400 V was used for supplying the AB (current electrodes) line. The obtained VES curves were processed and quantitatively interpreted using the INCEL software. As a result of processing and quantitative interpretation of the VES1 curve, the image of the system of geological layers was obtained on the basis of the distribution of real resistivity values at the scale of the real depth. Interpretation of VES1 soundings (Fig. 4) was correlated with the profile of the drill openings (Fig. 4) and with the diagram of the dynamic sounding DPL (Fig. 4). Increased values of the electric resistivity are clearly visible on the VES1 curve – approx. 190–240 Ωm from the terrain surface to a depth of approx. 2 m. This separation corresponds to wet, medium and coarse in medium-density conditions. Deeper, between 2.0–3.0 m the layer of very high resistivity is visible, equal to approx. 1700 Ωm – it corresponds to coarse, loose sands. At a depth of 3 m, the free level of groundwater occurs in coarse sands; loose conditions – the resistivity of these sediments is equal to 80 Ωm . At a depth of 7 m, the floor of cohesive sediments was interpreted; its resistivity is equal to 28 Ωm ; it was impossible to reach this levels by drilling. In the case of performed VES1 sounding, it is important to ensure correlation within the interval of depth between 2–3 m below the terrain surface, of the separated geological layer characterised by the high electric resistivity of 1700 Ωm , with the geotechnical layer, which corresponds to coarse sands in loose conditions. This layer is the privileged path for suffosion processes.

Within the Kobylnica test site, one geotechnical drilling was performed to a depth of 4 m below the terrain surface, as well as two DPL soundings to a depth of 6 m below the terrain

surface. In the profile of drilling loose sediments of the river origin (fine sands, coarse sands and gravels). The free level of the groundwater was drilled to a depth of about 3 m, which coincides with data obtained from geophysical tests.

DPL soundings (Fig. 4) proved that the grounds are in a medium-dense condition, from the terrain surface up to the depth of about 1.8–2.0 m below the terrain surface; deeper they are in loose conditions.

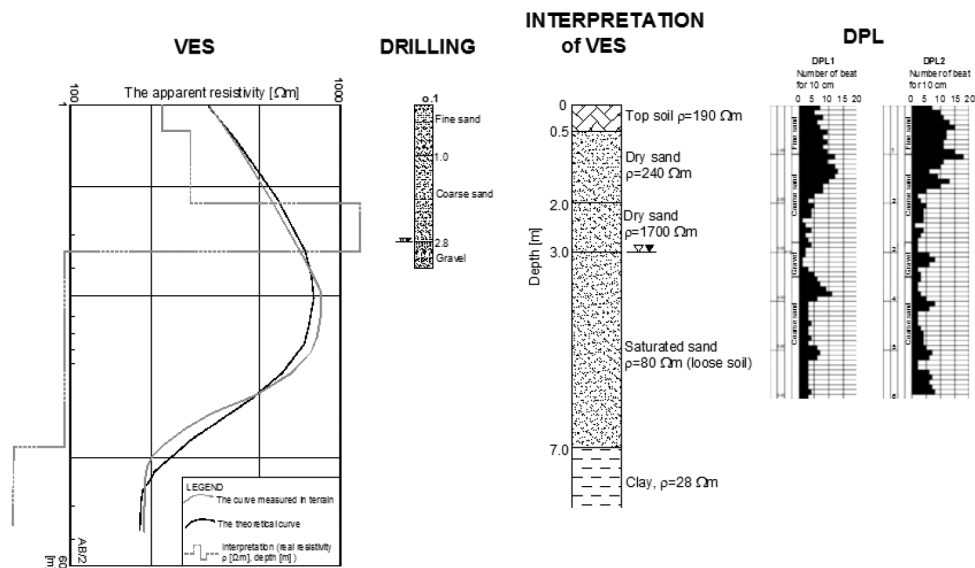


Fig. 4. Presentation of the results of investigations: VES, drilling, DPL. Kobylnica (2012)

4.2. The electric resistivity tomography

Field data was processed using the Res2Dinv software package [14]. All measurements were performed in a system of 41 electrodes, following the gradient protocol. Measuring profiles were located in parallel and perpendicularly to the axes of the flood bank – Fig. 3. The interval between electrodes along the traced measuring profiles was equal to 2 m (measurements along the bank) and 1 m (cross measurements). The maximum range of the depth of recognition of the medium resistivity obtained in measurements, equalled about 10 m below the flood foundation. Distribution of the electric resistivity within the flood bank body is uniform within the prevailing part of the examined sections of banks. Only in the northern part is the anomaly relating the increased resistivity value visible. Below the flood bank foundation, in the ground, measurements point to two anomalies of the increased resistivity: between 24–34 m and between 56–66 m of the profile length (Fig. 5). The increased values of the ground resistivity may result from changes in the lithology of grounds or of the increased porosity. The drilling profile made in the foundation of the flood bank (in the ground) to a depth of 4 m proves that within the given area, loose sediments occur of variable granularity (fine

sands, coarse sands and a small layer of gravel). In such conditions, the considerable increase of the ground resistivity which was obtained in the ERT tests, results from the increased porosity of sediments. This result confirms the thesis, which was formulated during the measurements performed, with the use of the method of vertical electric resistivity sounding that the layer characterised by the increased resistivity value is the privileged path for the suffusion processes. There was no anti-filtration diaphragm during ERT measurements in the embankment.

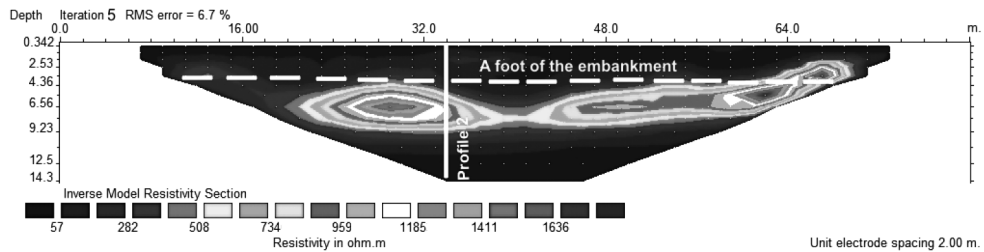


Fig. 5. The ERT – Profile 1 along the bank axis, Kobylnica

The measurements, which were performed transversely to the axis of the flood bank (Fig. 6), allowed for the separation of two distinct zones of the increased value of resistivity; at the eastern side, in grounds, below the bank foundation and at the western side, within the flood bank body.

The location of anomalies at the eastern side correspond to the occurrence of the zone of the hydraulic leakage (suffusion) of 2010 (Fig. 2, 3). This anomaly extends under the bank and it presents the expansion of grounds, within which, suffusion processes are generated. The anomaly in the bank body at the western side, may result from the increased porosity of the embankment grounds and/or their shrivelling processes.

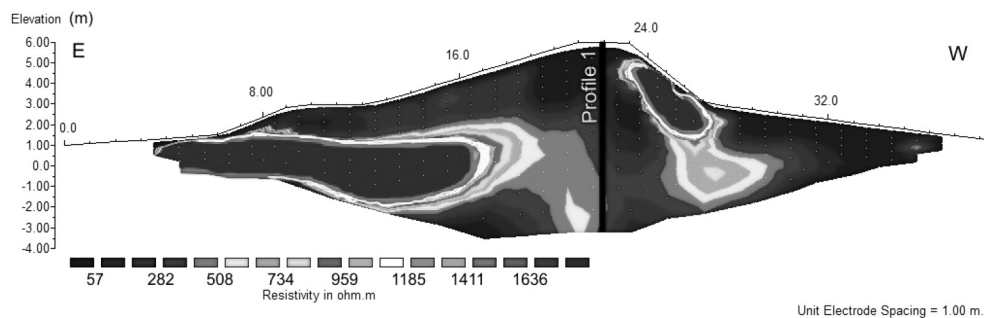


Fig. 6. The ERT method – Cross-section 2, perpendicular to the bank axis, Kobylnica

4.3. The ground penetrating radar method

Results of the ground penetrating radar data were processed with the use of the system for advanced data processing and interpretation: ReflexW by Sandmaier Co. Geo-radar data processing aimed at gain the signal of the electromagnetic wave and elimination of noises. There were applied the following procedures of the processing: move starttime, subtract-DC-shift, bandpassfrequency, background removal and gain. Interpretation of results of geo-radar testing was mainly performed with respect to location of anomalies related to zones of electromagnetic waves attenuation (Fig. 7, 8), which are visible on radargrams. They may be caused by: moist grounds or their attenuation, or adding the fraction of dusts or silt. In order to verify the origin of the anomalies, geotechnical investigations were performed

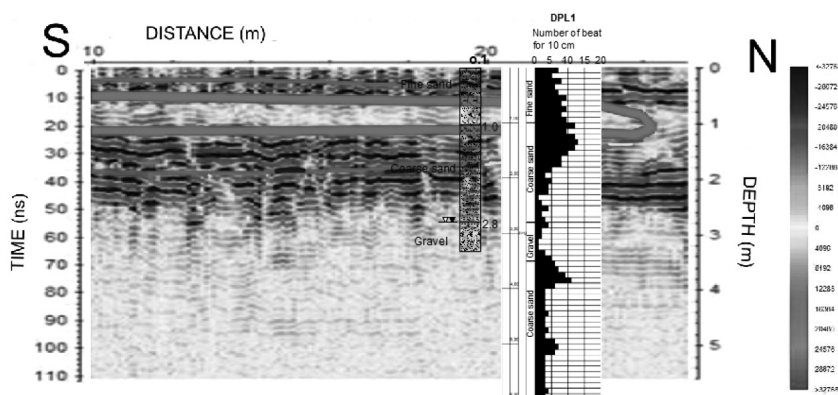


Fig. 7. Profile 1 – geo-radar radargrams with presented zone of electromagnetic waves attenuation

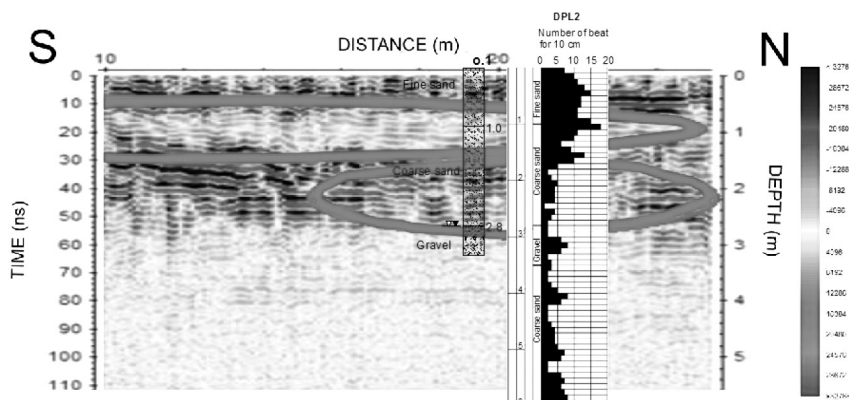


Fig. 8. Profile 2 – geo-radar radargram with presented zone of electromagnetic waves attenuation

(drilling and DPL sounding). Correlation of geotechnical data and GPR radargrams proves the correlation of zones of electromagnetic waves attenuation with sand in loose conditions. The lack of reflections in Profile 1 between depths of 0.5 m to 1 m is caused by the presence of fine sands. Appearance of reflections in coarse sands is obvious because the porosity of such a medium is higher and the porous space is filled with air. Along profile 2 decreasing of reflections amplitudes between depths of 1.5 m and 3 m might be caused by the increase moisture of the soil.

It was accepted for time-depth conversion that velocity is 0.07 m/ns).

4.4. The method of refractive seismic

Analysis of data obtained from the refractive seismic allowed for the separation of two seismic layers (Fig. 9). The layer 1: the velocity of the seismic wave is c.a. 386 m/s. In layer 2 the velocity of the seismic wave is c.a. 834 m/s. The seismic border between layers (no. 1 and no. 2) corresponds with the maximum value of the soil density.

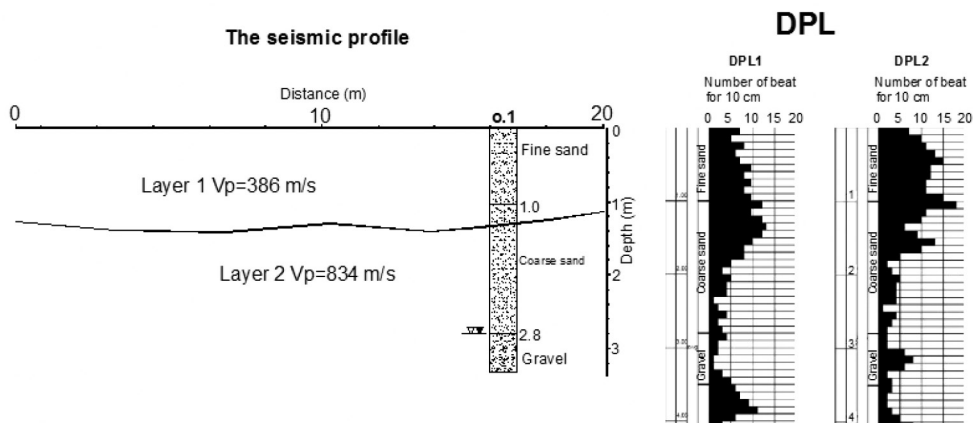


Fig. 9. Seismic cross-section

The method of refractive seismic did not give good results in this problem because the zone of suffosion is shallow and probably is small in size.

5. Numerical analysis

The investigated sections of the flood bank were numerically modelled (Fig. 10). The geological structure, parameters of the filtering diaphragm and grounds were assumed based on results of the performed boreholes, dynamic probing and the design of the modernisation of flood banks [13].

In order to evaluate the filtration and stability of flood banks, the specialised software package, *Z_Soil.PC*, was applied for engineering calculations. The model of untraced filtration was used for calculations. The function which describes variations in the water table level was specified based on hydrograms of passing of the flood wave in 2010. The total raised water stage lasted for 33 days. Coefficients of the stability were determined using the method of proportional reduction of resistance parameters ($c-\phi$ reduction) [15].

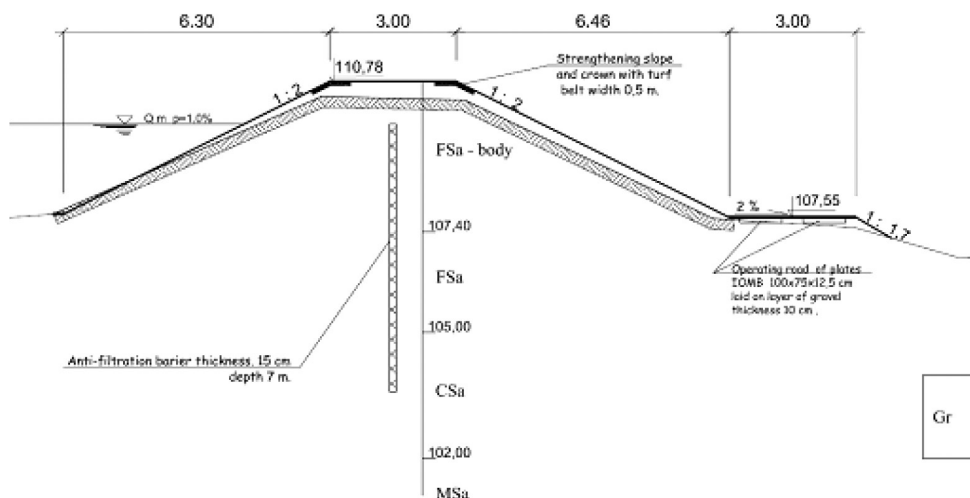


Fig. 10. Cross-section of the flood bank in Kobylnica

Due to considerable water leakages observed during the flood of 2010, numerical simulations were implemented concerning the insufficient depth of the constructed anti-filtrating diaphragm to the assumed level in the flood bank foundations, as well as the existing hydraulic leakages. Three numerical models (Fig. 11) presenting various stages of the development of hydraulic leakages were generated, which specified these leakages.

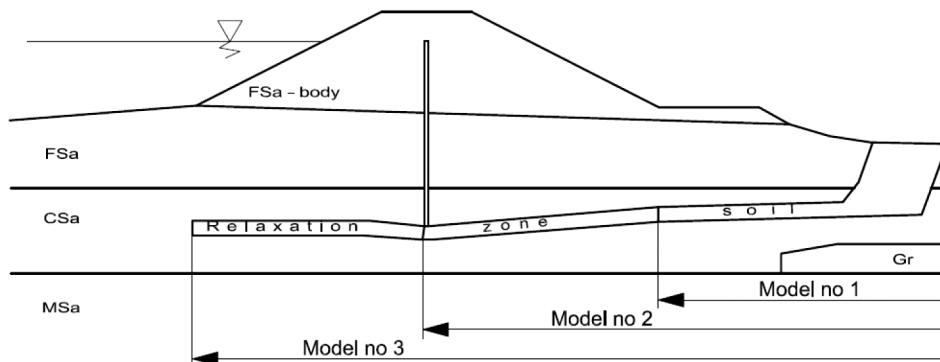


Fig. 11. Computational model – variants of calculations

Below, selected results of filtration (Fig. 12, 13) and stability (Fig. 14) are presented for model no. 3; the best compliance with observations performed during the high water stage in 2010 were obtained for this model.

The results of geophysical research proves that the modernization of flood embankments in the area of Kobylnica is. In the vicinity of the levee the anomalies in the ground were detected. On the basis of measurements field can be assumed that these areas are loosened or damp soil. This suggests the occurrence of subsidence which can be due to the presence of increased filtration phenomena (sufossion, hydraulic leakage). During various phases of the high water stage (rising or falling down of water between flood banks) the downstream face may lose its stability.

The obtained results of calculations should be considered with the tolerance resulting from the assumed theses, the level of accuracy of recognition of material zones of the flood bank body and the foundations, as well as from the assumption of the plain conditions of the numerical analysis. Computations considered the effect of the internal erosion, generation of

Table 1

Summary of material parameters

Type of Soil	E	ν	γ	γ_D	k	C	ϕ
	[kN/m ²]	[-]	[kN/m ³]	[kN/m ³]	[m/day]	[kN/m ²]	[deg]
Fsa – body	80000	0.3	18	18	5	3	27
Fsa	80000	0.3	18	18	5	3	27
Msa	120000	0.25	16	16	20	3	31
Csa	95000	0.25	18	18	30	3	32
Gr	155000	0.2	18	18	50	2	36
RZS*	120000	0.25	16	16	100	3	17

* Relaxation zone soil

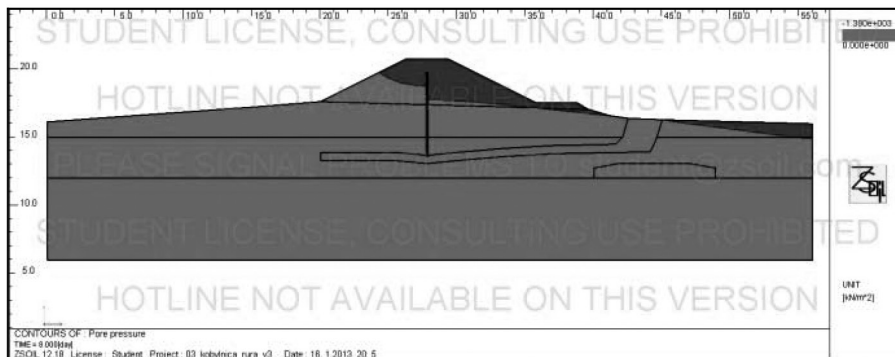


Fig. 12. Location of the depression curve

zones of grounds of modified values of parameters; for such an assumption the compliance of quality with observations performed during the flood was obtained. Thus, the extension of changes in the foundations, assumed for the analyses, was confirmed. It should be realised that during the successive raised water stage, in the same place, the development of the disadvantageous phenomenon of internal erosion will take place and the stability of the flood banks may be threatened.

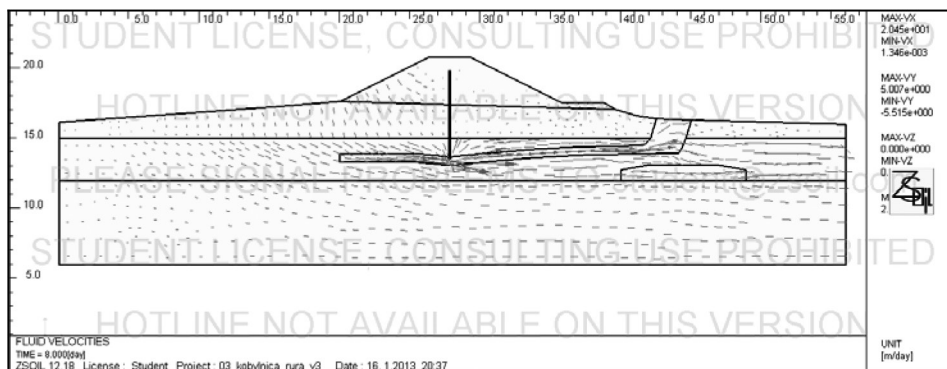


Fig. 13. Distribution of water flow speed vectors

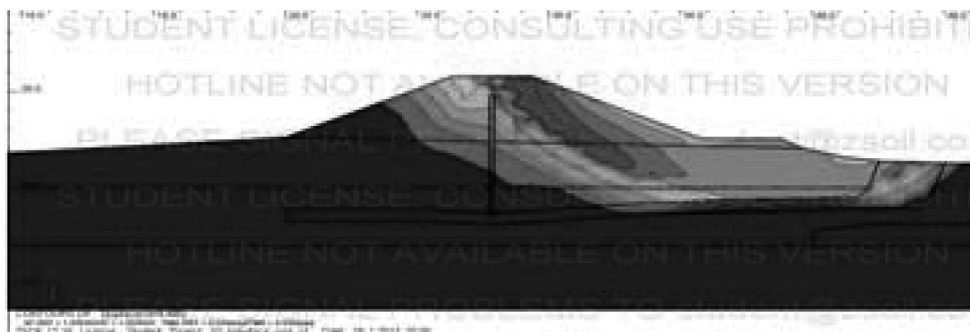


Fig. 14. The slipage area $SF = 1.60$

6. Final remarks

- Based on the performed tests, the usefulness of geophysical methods for recognition of technical conditions of flood banks may be stated, together with the possible specification of zones of diversified density, stiffness, parameters of filtration within the flood bank body and in the foundations.
- For the low water level in the river bed, the following geophysical anomalies were stated:
 - the increase of the electric resistivity of loose grounds, as well as grounds of increased porosity, threatened by the processes of suffusion,

- the occurrence of zones of damping in geo-radar echograms within loose grounds, probably as well as grounds of increased wetness and porosity (suffosion phenomena),
- the visible decrease in the velocity of propagation of seismic waves in loose grounds, as well as in grounds of increased porosity.
- Detailed geotechnical investigations should be preceded by geophysical tests; due to their non-invasive features, they allow for the fast location of anomalies which occur within the investigated grounds. Therefore, it is possible to correctly locate research openings within the areas of anomalies and in typical places of the investigated flood bank.
- Geophysical methods, although their applications for the evaluation of technical conditions of hydrotechnical structures are relatively new in Poland, become more important in practice. The high potential of these methods, which can become an additional source of data, results from their non-invasive features. It is also possible to amend data concerning the specified area of interest between the places of testing (drilling, sounding) by verification of the variability of parameters of the ground medium using various geophysical methods.
- Multi-variant numerical analysis allowed for the utilisation of the results of the geophysical investigations, and next, for the determination of the location of the depression curve and places of flow concentration, variable in time, as well as calculation of the stability coefficient and location of the slippage zone of the escarpment in particular days of the raised water stage.
- Comparing results of investigations performed with the use of various methods allowed for the determination of the correctness of the results obtained with the use of geophysical methods, as well as the evaluation of their accuracy and possible scope of utilisation.

The authors would like to thank the Mazovian Unit of EU Programmes Implementation in Warsaw for financing the purchase of Terrameter LS (ABEM) out of the Regional Operating Programme 'Modernisation and Equipment of Laboratories of the Faculty of Geology of the University of Warsaw for conducting research and development works in the field of the environmental geo-engineering, important for the Mazovia Region – STAGE 1', which was applied for the implementation of the presented research works.

References

- [1] Barański M., Kłobukowski D., Makowski R., Popielski P., Szczepański T., *Analysis of possibilities to utilise geophysical surface seismic methods for evaluation of technical conditions of flood banks*, Czasopismo Techniczne z. 3-Ś/2012, Kraków 2012.
- [2] Fajkiewicz Z. (ed.), *Zarys geofizyki stosowanej, An outline of applied geophysics*, Wydawnictwa Geologiczne, Warszawa 1972.
- [3] Fry J.J., *How to Prevent Embankments from Internal Erosion Failure?*, International Symposium on Dams on Changing Word, Kyoto, Japan, June 5, 2012.
- [4] Grant Rektorski PW: *Analysis of possibilities to utilise geophysical surface seismic methods for evaluation of technical conditions of flood banks*, Koło Naukowe Inżynierii Wodnej Politechniki Warszawskiej, Warszawa 2011.
- [5] Grant Rektorski PW: *Analysis of possibilities to utilise modern methods of researches of grounds and numerical modelling for evaluation of technical conditions of hydro-*

- technical structures*, Koło Naukowe Inżynierii Wodnej Politechniki Warszawskiej, Warszawa 2012.
- [6] Griffiths D.H., Barker R D., *Two-dimensional resistivity imaging and modelling in areas of complex geology*, Journal of Applied Geophysics, no. 29, 1993, 211-226.
- [7] Jol H.M. (ed.), *Ground Penetrating Radar: Theory and Application*, 1st ed., Elsevier, 2009.
- [8] Karczewski J., *An outline of the geo-radar method*, Uczelniane Wydawnictwa Naukowo-Dydaktyczne AGH, Wydanie I, Kraków 2007.
- [9] Keller G.V. Frischknecht F.C., *Electrical methods in geophysical prospecting*, Pergamon Press Inc., Oxford 1966.
- [10] Kirsch R., (ed.), *Groundwater Geophysics, A Tool for Hydrogeology*, 2 vol. ed., Springer, 2009.
- [11] Loke M.H., Barker R.D., *Rapid least-squares inversion of apparent resistivity pseudosections by a quasi-Newton method. Geophysical Prospecting*, no. 44, 1996, 131-152.
- [12] Loke M. H., *Tutorial: 2-D and 3-D electrical imaging surveys*, Geotomo Software, Malaysia 2012.
- [13] Projekt wykonawczy – *Modernisation of the flood bank, 2nd class in km 35+000 to 45+000, of the right-hand bank of the Vistula River valley, at the section: Antoniówka Świerżowska-Wróble Wargocin, Maciejowice Municipality, Garwolin District*, BIPROMEL, 2003.
- [14] *Res2DINV Manual*, GEOTOMO Software, 5 Cangkat Miden Loroung 6, Miden Heights, 11700 Gelugor, Penang, Malaysia, 2003, (www.geoelectrical.com).
- [15] Sanecki L., Truty A., Urbański A., *On the possibilities of computer-assissted modelling of stability of complex geotechnical systems*, Materiały XLV Konf. Nauk KILiW PAN Krynica 99, Wrocław 1999.
- [16] Szymanko J., Stenzel P., *Metody geofizyczne w badaniach hydrogeologicznych i geologiczno-inżynierskich*, Wydawnictwa Geologiczne, Warszawa 1993.

MARTA PUZDROWSKA*

APPLICATION OF NUMERICAL METHODS IN THE DESIGN AND ANALYSIS OF FISH PASS EFFICIENCY

ZASTOSOWANIE METOD NUMERYCZNYCH W PROJEKTOWANIU I ANALIZIE SPRAWNOŚCI PRZEPLAWKI DLA RYB

Abstract

The paper summarizes the examples of numerical computational methods to analyze the efficiency of fish passes. Numerical simulations were performed using the commercial software Flow 3D. The examples refer to the 2 types of construction of the device: Vertical Slot Fishways and Bolt Fishways.

Keywords: turbulence energy, fishways, fish pass, turbulent flow

Streszczenie

W niniejszym artykule przedstawiono przykład zastosowania metody numerycznej do analizy sprawności przepławek dla ryb. Obliczenia wykonano programem Flow 3D. Przykład odnosi się do 2 typów konstrukcji urządzenia: przepławki szczelinowej i ryglowej.

Słowa kluczowe: energia turbulentna, przepławki dla ryb, przepływ turbulentny

* M.Sc. Marta Puzdrowska, Instytut Geotechniki i Hydrotechniki, Wydział Budownictwa Lądowego i Wodnego, Politechnika Wrocławska.

List of variables

U_{crit}	– critical velocity of fish swimming [$m \cdot s^{-1}$],
NSL	– normal storage level [m],
$\bar{u}_x, \bar{u}_y, \bar{u}_z$	– mean (time-averaged) components of velocities (u_x, u_y, u_z) [$m \cdot s^{-1}$],
u_x', u_y', u_z'	– fluctuating components of velocities (u_x, u_y, u_z) [$m \cdot s^{-1}$],
\bar{p}	– mean (time-averaged) pressure [Pa]
p'	– fluctuating term of pressure [Pa]
t	– time [s]
ρ	– specific water density [$kg \cdot m^{-3}$]
F_x, F_y, F_z	– directional vectors of body force
μ	– dynamic viscosity of water [$kg \cdot m^{-1} \cdot s^{-1}$]
k	– turbulent kinetic energy [$m^2 \cdot s^{-2}$]
ε	– dispersion of turbulent kinetic energy [$m^2 \cdot s^{-3}$]
\bar{u}_{max}	– maximum average velocity [$m \cdot s^{-1}$]
\bar{u}_{min}	– minimum average velocity [$m \cdot s^{-1}$]

1. Fish pass efficiency

1.1. Definition of fish pass efficiency

- The efficiency of fish passes determined as a resultant of 2 key parameters [1], i.e.:
- quotient of fish of a given species which have passed an obstacle, and the number of fish trying to pass it;
 - time taken by fish to pass through the obstacle, the so-called delay.
 - Considering the aforementioned parameters, an assessment scale for fish pass efficiency was given below [1] and [2]:
- | | |
|------------------|--|
| <i>Very Good</i> | – 100% of fish pass the obstacle, delay of up to few hours, |
| <i>Good</i> | – over 95% of fish pass the obstacle, delay of up to few days, |
| <i>Weak</i> | – 70 to 95% of fish pass the obstacle, delay of over few days, |
| <i>Bad</i> | – less than 70% of fish pass the obstacle, delay of over few days. |

Facilities assessed as weak or bad should be redeveloped

Experience in assessing the efficiency of facilities used for fish migration proved that despite obtaining proper distribution of mean velocities in laboratory tests, i.e. such, which are tolerated by water organisms, the facilities did not achieve the required efficiency. As a consequence, it seems to be obvious that it is necessary to analyze the issue of water flow in fish passes, including more details for the flow characteristics.

As proved by practical experiments, the factor defining the efficiency of those facilities is not the mean flow, but turbulences occurring in the examined flow and their spatial distribution and intensity.

1.2. Requirements of ichthyofauna

Physical body parameters and swimming skills of catadromous fish are significantly lower in comparison to anadromous fish, which are physically adapted to overcome huge migration obstacles. For example, *critical swimming velocities*¹ (U_{crit}) defined by Pavlov [3] for bullhead are included in a range of $0.15\text{--}0.34\text{ m}\cdot\text{s}^{-1}$. Whereas perches and roaches seem to have better swimming skills. Based upon tests performed using those fish, it was established that in case of: perches $U_{crit} = 0.56\text{--}1.26\text{ m}\cdot\text{s}^{-1}$, and for roaches $U_{crit} = 0.91\text{--}1.22\text{ m}\cdot\text{s}^{-1}$ [5].

Moreover it was stated that the flow of fish within such areas where a turbulent flow occurs, causes an increase in the resistance force affecting the fish body. It may also cause orientation turbulence for some fish species, and even form a barrier and block the entrance to the next chamber. Such fish swimming skills as critical velocities estimated in the laboratory [6] seem to be re-evaluated in comparison to the ones observed in the environment [7].

The currently constructed facilities have a variable, uneven effectiveness for different fish species [8–10]. Designs are often developed based upon the requirements of a single or sometimes, a group of the selected species, Salmonidae mainly [11–13]. Unfortunately, such an approach makes a fishway at once useless for the remaining species of ichthyofauna, and especially for catadromous fish. Their relatively low spurt velocities and the shorter time of their maintenance in case of weaker specimens (it is also related to young Salmonidae specimens) forces the necessity to redevelop the existing fish passes in order to form a possibility of instant passage through the facility also for weaker fish [11] and [7]. It is recommended to arrange the new facilities with areas having a variable flow regime. It would allow for different fish species to overcome the fish pass and to pass through it efficiently.

2. Model of a fish pass

2.1. Basic information on a modelled object

The analysis of numerical verification potential for the efficiency of the fish pass will be performed based upon a newly constructed fish pass at the weir in Rzeszow, at chainage km 63.760 of the River Wislok. The object is located on the right river bank under the Karpacki Bridge at Powstancow Warszawy Alley in the city centre.

The fish pass includes two sections with varied constructions of partitions. The upper part is a fish pass with chamber and vertical-slot construction. The average width of the chambers is about 2.5 m. The width of the vertical slots is within the range of 0.8–1.0 m.

The lower part is a bolt structure (a partition consisting of arranged concrete rotary cylindrical elements with an elliptic section of $0.6 \times 0.4\text{ m}$). The width of chamber is 4.0 m, and the slot is 0.8 m. The length of the chamber in the case of both parts is 6.0 m. The estimated designed flow is $2\text{ m}^3\cdot\text{s}^{-1}$, at the NSL² of the reservoir.

¹ U_{crit} – critical velocity of fish swimming, i.e. the lowest fish swimming velocity, at which the water current starts to wash them away [4].

² NSL – normal storage level – it is the highest operational level of the water surface in periods except for freshets.



Fig. 1. View of the upper part of the structure fish passes with construction of Vertical Slot Fishways



Fig. 2. View of the upper part of the structure fish passes with construction of Bolt Fishways

2.2. Governing equations

The equations governing the steady, incompressible, three-dimensional turbulent flow are the Reynolds-averaged Navier-Stokes equations (N-S). The solution to issues associated with the turbulent flow is possible through applying the Reynolds Hypothesis to N-S equations, i.e. records of instantaneous velocity (u_x, u_y, u_z) and pressure (p) values, including the following component values: mean (time-averaged) ones and fluctuating ones in accordance with the following example:

$$u_x = \bar{u}_x + u'_x \quad (1)$$

where:

\bar{u}_x – mean (time-averaged) velocity,

u'_x – fluctuating term of velocity.

Such a modification of N-S equation is often named as a set of Reynolds equations, which can be presented in the following form [14]:

$$\begin{aligned} \frac{\partial \bar{u}_x}{\partial t} + \bar{u}_x \frac{\partial \bar{u}_x}{\partial x} + \bar{u}_y \frac{\partial \bar{u}_x}{\partial y} + \bar{u}_z \frac{\partial \bar{u}_x}{\partial z} &= F_x - \frac{1}{\rho} \frac{\partial \bar{p}}{\partial x} + \frac{\mu}{\rho} \left[\frac{\partial^2 \bar{u}_x}{\partial x^2} + \frac{\partial^2 \bar{u}_x}{\partial y^2} + \frac{\partial^2 \bar{u}_x}{\partial z^2} \right] - \left[\overline{\frac{\partial u_x'^2}{\partial x}} + \overline{\frac{\partial u_x' u_y'}{\partial y}} + \overline{\frac{\partial u_x' u_z'}{\partial z}} \right] \\ \frac{\partial \bar{u}_y}{\partial t} + \bar{u}_x \frac{\partial \bar{u}_y}{\partial x} + \bar{u}_y \frac{\partial \bar{u}_y}{\partial y} + \bar{u}_z \frac{\partial \bar{u}_y}{\partial z} &= F_y - \frac{1}{\rho} \frac{\partial \bar{p}}{\partial y} + \frac{\mu}{\rho} \left[\frac{\partial^2 \bar{u}_y}{\partial x^2} + \frac{\partial^2 \bar{u}_y}{\partial y^2} + \frac{\partial^2 \bar{u}_y}{\partial z^2} \right] - \left[\overline{\frac{\partial u_x' u_y'}{\partial x}} + \overline{\frac{\partial u_y'^2}{\partial y}} + \overline{\frac{\partial u_y' u_z'}{\partial z}} \right] \\ \frac{\partial \bar{u}_z}{\partial t} + \bar{u}_x \frac{\partial \bar{u}_z}{\partial x} + \bar{u}_y \frac{\partial \bar{u}_z}{\partial y} + \bar{u}_z \frac{\partial \bar{u}_z}{\partial z} &= F_z - \frac{1}{\rho} \frac{\partial \bar{p}}{\partial z} + \frac{\mu}{\rho} \left[\frac{\partial^2 \bar{u}_z}{\partial x^2} + \frac{\partial^2 \bar{u}_z}{\partial y^2} + \frac{\partial^2 \bar{u}_z}{\partial z^2} \right] - \left[\overline{\frac{\partial u_x' u_z'}{\partial x}} + \overline{\frac{\partial u_y' u_z'}{\partial y}} + \overline{\frac{\partial u_z'^2}{\partial z}} \right] \end{aligned} \quad (2)$$

The basis of the model is completed by continuity equation having the following form (markings as above):

$$\frac{\partial \bar{u}_x}{\partial x} + \frac{\partial \bar{u}_y}{\partial y} + \frac{\partial \bar{u}_z}{\partial z} = 0 \quad (3)$$

Eq. (2) is the momentum conservation equation with the last term on the left side representing the Reynolds stress arising from the fluctuating velocity field. This term can be determined on the basis of the turbulent kinetic energy model. In this calculation the two-equations $k - \varepsilon$ model was used originally developed by Launder and Sharma in 1974, in which model transport equations are solved for two turbulence quantities – turbulent kinetic energy k and its dissipation ε [14].

The turbulence kinetic energy is defined to be half the trace of the Reynolds stress tensor:

$$k = \frac{1}{2} \left[\overline{u_x'^2} + \overline{u_y'^2} + \overline{u_z'^2} \right] \quad (4)$$

The dissipation of turbulent kinetic energy may be identified using the following relation:

$$\varepsilon = - \frac{\partial k}{\partial t} \quad (5)$$

This set of equations must be complemented by boundary conditions – no-slip and impermeability at the wall, at the inlet, velocity was given. At the outlet, relative pressure. On the free surface, tangential stresses are zero. As an initial condition, assumed zero velocity field at time $t = 0$.

2.3. Numerical model of the object

Numerical simulations were performed using commercial software 3D flow, which is based on the finite volume method (FVM).

For the purpose of developing the fishway's numerical model, in the 1st step a three-dimensional model of the real-scale object was prepared in a graphical software program. Data was subsequently generated to the file with .stl format and uploaded to the Flow 3D software. Blocks of computational grid were then generated, and they included cubes with a length of side of 0.1m and comprised within its range and route the entire bed of the fish pass. As an initial conditions for calculation a water level at the upstream weir's station, at the inlet to the fish pass, was given, i.e. "P" – Pressure boundary condition; applied, when we do not know the exact course of flow distribution; although, boundary pressure values are known (e.g. filling up).

For the purpose of a description of model operations one has applied the following boundary conditions of computational areas:

- "O" – Outflow boundary condition; applied if there is a flow through the surface of the computational grid, but, we do not know its course. In the case of the discussed model these are sides of grid blocks within the channel's route, where the flow of water occurs;
- "S" – Symmetry boundary condition; applied if there is no flow through the boundary.

These conditions were defined on the surfaces of the computational solids, as determined in Fig. 3.

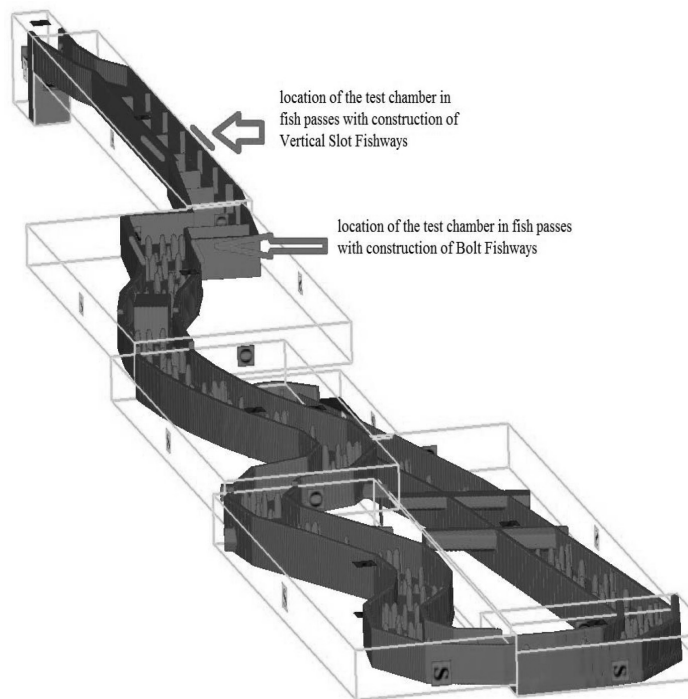


Fig. 3. Numerical grid with boundary conditions

3. Summary of results

3.1. Results of simulation of the vertical slot fishway

The following figures present a comparison of parameters derived for the partition and the inside of the chamber, in the upper section of the vertical slot fish pass.

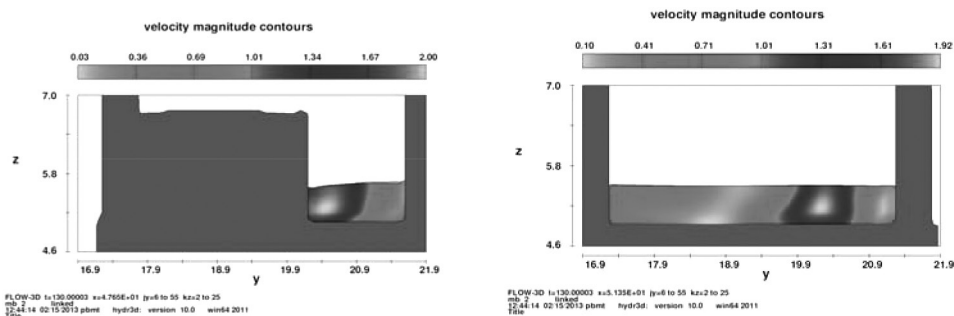


Fig. 4. Velocity values determined using Flow 3D (on the left: in a vertical slot; on the right: in the chamber)

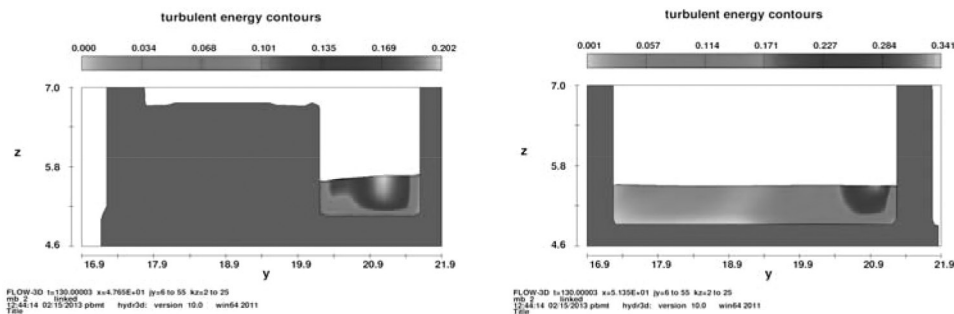


Fig. 5. Value of turbulent kinetic energy – k , established using Flow 3D (on the left: in a vertical slot; on the right: in the chamber)

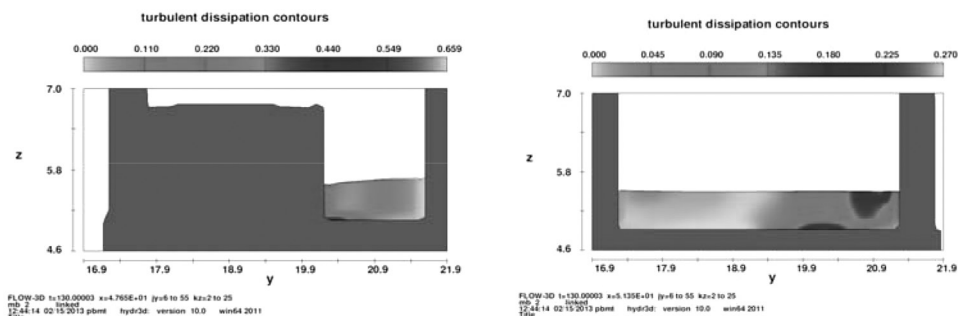


Fig. 6. Value of turbulent kinetic energy's dissipation – ϵ , established using Flow 3D

3.2. Results of simulation of the bolt fishway

The following figures present a comparison of parameters derived for the partition and the inside of the chamber, in the lower section of the bolt fish pass.

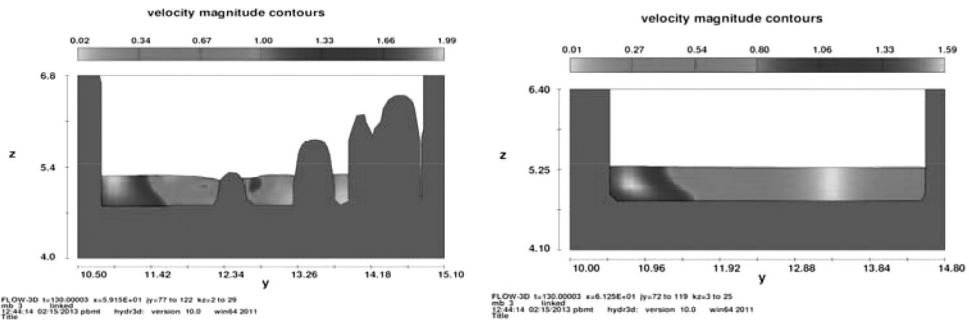


Fig. 7. Velocity values determined using Flow 3D (on the left: in a vertical slot; on the right: in the chamber)

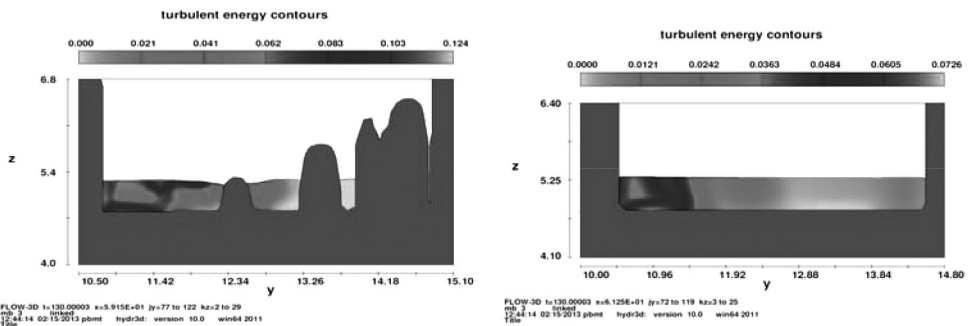


Fig. 8. Value of turbulent kinetic energy – k , established using Flow 3D (on the left: in a vertical slot; on the right: in the chamber)

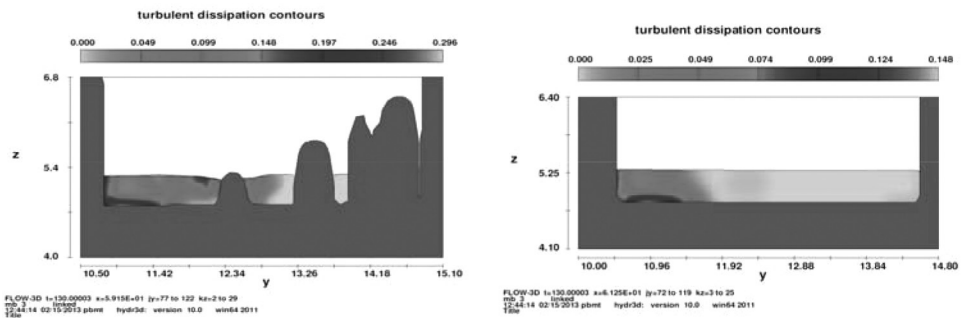


Fig. 9. Value of turbulent kinetic energy's dissipation – ϵ , established using Flow 3D

3.3. Summary of derived results

Table 1

Values of velocities and turbulent parameters k and ε , established using Flow 3D.

	\bar{u}_{\min}	\bar{u}_{\max}	k	ε
units	[m·s ⁻¹]	[m·s ⁻¹]	[m ² ·s ⁻²]	[m ² ·s ⁻³]
vertical slots	0.03	2.0	0.202	0.659
chamber	0.10	1.92	0.341	0.270
bolts	0.02	1.99	0.124	0.296
chamber	0.01	1.59	0.073	0.148

Within a baffle of Vertical Slot Fishways, lamp field can be observed with a high flow velocity (over 1.2 m·s⁻¹), which exceeds the swimming skills of catadromous fish. These fields cover about 55–60% of the slot's surface section. Field with the highest values of turbulent kinetic energy (k), up to 0.2 m²·s⁻², is located within the cross area of the slot, overlapping with a slower flow (in the range 0.1–1.0 m·s⁻¹). The range participation of areas of dissipation of kinetic energy is small. It occurs mainly in the transverse wall of the baffle; however, it reaches a fairly high value of 0.66 m²·s⁻³. After overlapping the areas where too high velocity and high values of k occur, it can be observed that they occupy most of slot's section leaving a small flow section for weak and small fish.

The transom baffle fish pass includes cylindrical transom elements. It does not form a compact structure, and as a result, enables the development of several flow fields with different locations within the baffle. Within the section of transom fish pass's section one may also observe field velocities higher than 1.2 m·s⁻¹, but their share is smaller. It occurs only in the greatest main baffle and amounts to about 40% of its sectional area. The field of high velocities is more broken and varied. This is due to the presence of bolts having an elliptical section and of the structures shown on the Figures which are formed due to the flow over the transom elements. Similar observations refer to the distribution and values of turbulent kinetic energy k . Fields for the higher values of k are scattered and do not occupy the entire field of lower velocities in the main slot. Moreover, the values of k are lower and amount to about 60% of values in Vertical Slot Fishways. The share of areas with energy dissipation is definitely bigger, which is a consequence of the decays of vortex structures that arise when passing the bolts. The values of dissipation in the slot's cross-section, even though it occupies a larger area, are also less than half lower than in the case of the Vertical Slot.

In the case of both types of constructions, there are areas with very different values and reach of all parameters (v , k , ε) in the chambers, which allow fish to find suitable conditions for migrating and reposing over the entire length of chambers.

4. Conclusions

Experience in the efficiency assessment for facilities used for fish migration proved that despite obtaining (also during laboratory tests) a proper distribution of mean velocities, i.e. such as those are tolerable by water organisms, fishways did not achieve the required efficiency. An objective for further works (performance of field tests) is to attempt to prove a thesis that turbulences occurring in the examined flow and that their spatial distribution and intensity, and not, as previously forced, the mean flow, decide on the efficiency of the fish pass. As a result, it seems to be obvious that it is necessary to analyze the issue of water flow within the fishways, including more details for flow characteristics. It seems that the problem may be associated with the velocity fluctuation, and therefore the direction of the discussion seems to be correct. Especially since in case of both types of studied fish passes, at least half of the cross-sectional area of the main slot contained average velocities lower than $1.2 \text{ m} \cdot \text{s}^{-1}$, which would facilitate the fish in finding the right migration way. The efficiency of both devices should be the same or similar.

However, during numerous site visits to the object, it was observed that all fish, regardless of size and species passed through Bolt Fishways more efficiently and definitely in a shorter time. In part of Vertical Slot Fishways, smaller fish and fish with lower swimming abilities gathered in front of the baffle wall. They took multiple attempts to pass through obstacles with little success.

While analyzing the total of field surfaces with high velocity and fields with high turbulent kinetic energy, one can see that in case of Vertical Slot Fishways, they occupy (globally) most of the slot's section, which means that behaviour of fish may be explained by the following statement (hypothesis): the value of the turbulent energy may remain an additional barrier for fish migration.

Tests performed up to this moment do not allow for obtaining an unequivocal correlation between the fishway's efficiency and the kinetic energy. Hence, it would be recommended to perform a wider analysis of turbulent flow parameters, including more tests, which would confirm or refute the given hypothesis.



KAPITAŁ LUDZKI
NARODOWA STRATEGIA SPÓJNOŚCI



URZĄD MARSZAŁKOWSKI WOJEWÓDZTWA DOLNOŚLĄSKIEGO
**DOLNY
ŚLĄSK**
www.umwd.pl

UNIA EUROPEJSKA
EUROPEJSKI
FUNDUSZ SPOŁECZNY



This paper is co-financed by the European Union as part of the European Social Fund.

References

- [1] Bojarski A. et. al., *Zasady dobrej praktyki w utrzymaniu rzek i potoków górskich*, Ministerstwo Środowiska, Departament Zasobów Wodnych, Warsaw 2005.
- [2] Jelonek M., *Utrzymanie i przywracanie, ekologicznej ciągłości rzek. Renaturyzacja, restytucja, re introdukcja*, prezentacja, Brzeczowice 2008.
- [3] Pavlov D.S., *Structures assisting the migration of non-salmonid fish: USSR*, FAO Fisheries Technical Papers 308, 1989.

- [4] Pavlov D.S., Lupandin A.I., Skorobogatov M.A., *The Effects of Flow Turbulence on the Behavior and Distribution of Fish*, Journal of Ichthyology, Vol. 20, 2000, 232-261.
- [5] Beatty S.J., Morgan D.L., Torre A., *Restoring ecological connectivity in the Margaret River: Western Australia's first rock-ramp fishways*, Ecological Management & Restoration, Vol. 8, No. 3, December 2007.
- [6] Tudorache C., Viaene P., Blust R., Vereecken H., De Boeck G., *A comparison of swimming capacity and energy use in seven European freshwater fish species*, Ecology of Freshwater Fish, 17, 2007, 284-291.
- [7] Lucas M., Baras E., *Migration of Freshwater Fishes*, Malden, MA, Blackwell Science, Oxford 2001.
- [8] Jungwirth M., Schmutz S., Weiss S., *Fish migration and fish bypasses*, Oxford: Fishing News Books, Blackwell Science, 1998.
- [9] Stuart I.G. and Mallen-Cooper M., *An assessment of the effectiveness of a vertical-slot fishway for non-salmonid fish at a tidal barrier on a large tropical/subtropical river*, Regulated Rivers, Research and Management, 15, 1999, 575-590.
- [10] Bunt C.M., Cooke S.J., McKinley R.S., *Assessment of the Dunnville fishway for passage of walleyes from Lake Erie to the Grand River, Ontario*, Journal of Great Lakes Research 26, 2000, 482-488.
- [11] Clay C.H., *Design of Fishways and Other Fish Facilities*. (2nd edn), Boca Raton, Lewis, and American Fisheries Society, Bethesda 1995.
- [12] Aarestrup K., Lucas M.C., Hansen J.A., *Efficiency of a nature-like bypass channel for sea trout (*Salmo trutta*) ascending a small Danish stream studied by PIT telemetry*, Ecology of Freshwater Fish, 12, 2003, 160-168.
- [13] Gowans A.D., Armstrong J.D., Priede I.G., McKelvey S., *Movements of Atlantic salmon migrating upstream through a fish-pass complex in Scotland*, Ecol. Freshw. Fish. 12, 2003, 177-189.
- [14] Popes S.B., *Turbulent Flows*, 8th ed., Cambridge University Press, 2011.

DANIEL SŁOWIKOWSKI*, GRZEGORZ KACPRZAK**

IMPLEMENTATION OF LOW PRESSURE INJECTION FOR SOIL REINFORCEMENT AND SEALING – SELECTED APPLICATION

ZASTOSOWANIE INIEKCJI NISKOCIŚNIENIOWEJ DO WZMOCNIENIA ORAZ USZCZELNIENIA PODŁOŻA GRUNTOWEGO – WYBRANA REALIZACJA

Abstract

The paper summarizes the practical aspects of the application of low pressure injection (grouting) for soil hydroinsulation and stabilization. Technical aspects of low pressure injection application and requirements dedicated to soil binders have been described. The paper also contains characteristics of selected investment where low pressure injection technology has been applied.

Keywords: execution of special geotechnical works, low pressure injection, hydroinsulation barrier, clay-cement binders, grouting

Streszczenie

W artykule przedstawiono praktyczne doświadczenia z zakresu stosowania iniekcji niskociśnieniowej w celu uszczelnienia i wzmocnienia podłoża gruntowego. Scharakteryzowano zagadnienia techniczne związane z wykonaniem iniekcji oraz wymagania dotyczące stosowanych spoiw gruntowych. Scharakteryzowano także wybraną inwestycję zrealizowaną w technologii iniekcyjnej.

Słowa kluczowe: wykonawstwo specjalnych robót geotechnicznych, iniekcja niskociśnieniowa, przesłony hydroizolacyjne, spoiwa ilowo-cementowe, grouting

* Msc. Eng. Daniel Słowikowski, Przedsiębiorstwo Robót Geologiczno Wiertniczych G. Janik R. Kuś sp.j. (PRGW).

** Ph.D. Eng. Grzegorz Kacprzak, Politechnika Warszawska, Wydział Inżynierii Lądowej, Instytut Dróg i Mostów.

1. Introduction

An intensive increase in the amount of new building investments has been observed for several years. Many of them are located in the centers of towns. The high cost of parcels and spatial restrictions determine investors to find flexible and cost efficient design solutions for the projects. Many of them require special and deep foundation or special geotechnical works for sealing or soil reinforcement (e.g. deep underground garage or crossing of underground communication and transport lines). One of the required elements of these projects is a hydroinsulation barrier. Depending on local conditions, the barriers are made in different technologies and to various depths. The basic expectations for waterproof barriers can be determined as follows:

- high insulating properties,
- long-term functionality,
- resistance to hydrostatic pressure,
- resistance to deformation,
- high resistance to corrosion caused,
- no impact on the environment.

One of the allowed ways for reinforcement and sealing is the injection of the binder (agent) into soil or rocks. Depending on injection pressure, we can differentiate between high pressure injection (jet grouting) and low pressure injection (grouting).

2. Low pressure injection

Low pressure injection (grouting) is a standardized method described by ISO Standards ISO-EN 12715 Execution of special geotechnical work. Grouting. Grouting isn't a method for the replacement of natural soil like jet grouting. In the grouting method, liquid agent is pumped by a special drilling hole into soil or rocks using pistons or plungers pump. Injected agent fills free area and decreasing water permeability. Therefore the goal of grouting can be described as modification of natural soil by:

- 1) filling of soil emptiness (suffosion effect, fractures etc.),
- 2) filling of porous canals in soil,
- 3) compaction and moving soil grains by the pressure of agent (binder).

Below (Fig. 1) is shown the theoretical model of soil sealing using water-cement suspensions pumping. The model is based on a column experiment where we can see three stages:

- 1) water pumping, where porosity and water permeability are constant,
- 2) agent pumping, where we can see a colmatation effect and
- 3) water pumping, where we can see partial decolmatation of pores.

In the 2nd stage, when we pump the agent, particle of cement fixes the pores and decreases permeability. During the injection and saturation of soil, we can observe an increase in injection pressure and a decrease flux in injected agent. In practice, the scale of this effect, as well as the distance of agent migration, depends on the soil condition and liquid agent parameters (e.g. viscosity, grain size of suspension). After the injection, the solidification process of the agent starts. If we make an injection into water flow area, a part of the agent can be distributed outside from injected soil, which makes increase permeable (reduced before). It is not a desired effect and we can eliminate it using sped up solidification components.

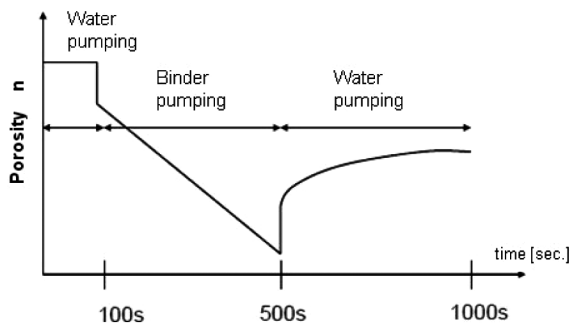


Fig. 1. Theoretical model of injection in porous media (water-cement suspension) [2]

Model Fig. 1 is typical for a liquid agent, similar to Newton's fluid model [2]. Many of the binders (agents) are thixotropic fluids (similar to Bingham's fluid model). The rheology and internal structure of thixotropic fluid is important for the decreasing or elimination of soluble binders, during and after injection. It is an important aspect of the injection design. Samples of quasi Bingham's binders are cement-bentonite solutions or binders based on modified clays.

Usually, the injection is made from bottom to top of injection unit of hole, by designed intervals (e.g. 1.0 or 0.5 m). In practice, pressure between 2–25 bar and flux 10–45 liters/min is used. The injection parameters depend on the soil or rock condition. For special jobs, injecting by angles and directional holes is possible.

Depending on the configuration of the injection holes kind of agent and agent propagation, grouting can find application in:

- building horizontal and vertical hydroinsulation barriers,
- protection and water inflow reduction for the deep founding excavations,
- modification of the mechanical parameters of soil and rocks,
- underground and open pit mine hydroinsulation,
- *in-situ* immobilization of the contaminants (soil and groundwater),
- contaminated soil and groundwater treatment.

3. Sealing and bonding agents

Depending on the requirements of the design, lots of different mixtures of binders can be described. The most popular, for engineering practice, are: water-cement suspensions; cement-bentonite solutions; silicates solutions (based on liquid glass); cement-clay solutions.

In PRGW (Geological and Drilling Works Company, Poland) practice, binders based on modified clays are the most useful. The main component of cement-clay binders is mono or poly-minerals clays, moved to water solution. The main required parameters of the clays are:

- 5 μm grain size participation > 60%,
- ability to form a thixotropic, colloid solution (Bingham's fluid).

Below is shown the mineral characteristic of clay from Brown Coal Mine in Bełchatów (Poland).

Mineralogical characteristics of clay from Belchatow brown coal resources (DTA – differential thermal analysis) [3]

Components	Content [weight %]
Beidellite (Montmorillonite group)	51.3–87.8
Kaolinite	8.7–14.2
Calcite	15.2–2.0
Siderite	0.0–5.0
Organic material	0.0–0.9
Thermal inactive minerals	1.4–18.5

Additional components of the solution based on the modified clay are:

- cement (as source of CSH phase),
- silicates (sodium liquid glass).

Below (Fig. 2) is shown a flowchart of the preparation of a solution based on modified clay [5]. In the first step, a water solution of clay, called base solution are prepared. In the second step, a base solution is modified by cement and silicate, and from this moment, the solidification reaction starts. The prepared binder is a thixotropic the solution and must be non-stop agitated before application to soil. It's necessary for the hang up solidification process and for the keeping the binders properties as liquid (solution).

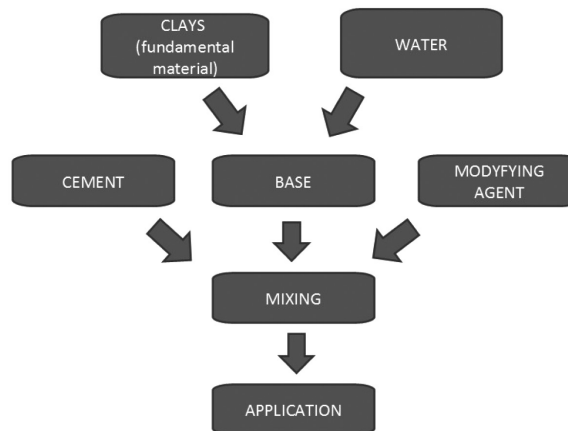


Fig. 2. Flow chart of preparation of the binder based on modified clays [5, 6]

Depending on the content of reagents, solidification can be managed according to the needs and project goals. Below (Fig. 3) are shown the results of the optimization of the solutions' rheological parameters. Depending of the contents of reagents, we can receive different parameters of binders, such as viscosity, thixotropy, etc. By managing the components, we can manage the binders parameters and fit them into the design requirements [6].

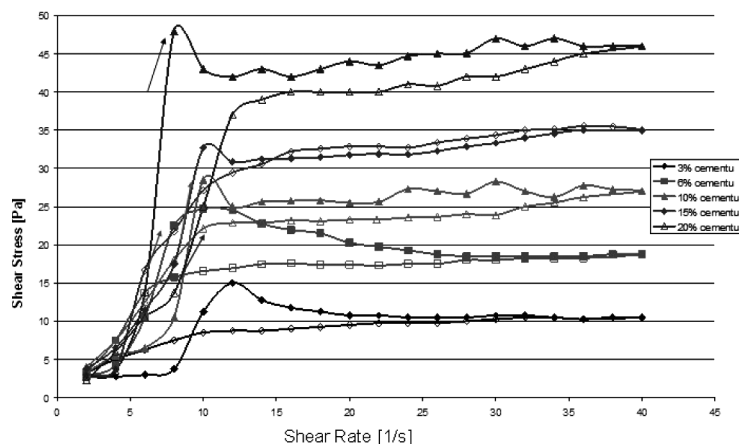


Fig. 3. Sample of rheological parameters optimization of liquid agent based on viscosity analysis [5]

Solidification is a highly expected attribute of soil binders which gives modified soil expected qualities. In Fig. 4 is shown SEM (Scanning Electron Microscope) view of a solid binder based on the modified beidellite clay from Bełchatów Field (Poland). In the picture we can see silicates and the aluminosilicates frame (phase CSH) filled with clay mineral packages. Silicates frame decide about mechanical parameters of solid binders and clay minerals about their permeability [6].

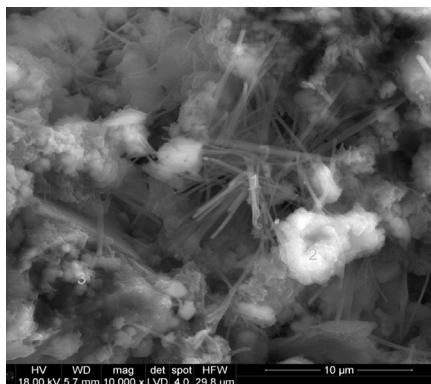


Fig. 4. SEM view of solid structure of agent based on modified clay [4, 5]

Selected parameters of the solid binder based on modified clay are [4, 5]:

- resistance to water soluble,
- no contraction during the solidification process,
- filtration coefficient of the binder – $k \sim 10^{-9}$ m/sec,
- Californian Bearing Ratio CBRd > 20%,
- shearing strength (resistance) ~ 190 kPa (after 28 days),
- bending strength (resistance) > 400 kPa (after 28 days),
- compression strength (resistance) > 500 kPa (after 28 days).
- full freeze resistance after 42 days (according to Transport and Road Research Lab. TRRL – UK).

4. Selected application – Horizontal hydroinsulation barrier for PROSTA Tower founding in Warsaw

A horizontal hydroinsulation barrier using low pressure injection was made for the protection and water inflow reduction of the deep founding excavation of PROSTA Tower in Warsaw. The Project was realized in the close center of the city, between already existing tall buildings. The reason for using the injection method was because it was a cost effective solution. The main goal of injection was:

- water inflow reduction,
- protection of water displacement of excavations bottom (–17,6 m below ground level and 13m hydrostatic buoyancy),
- no impact of groundwater drainage on neighboring buildings and area.

The whole area was enclosed by a 29,0 m deep diaphragm wall, suspended on permeable soil (medium and fine sands, ID ~0,6–0,8; $k \sim 8 \times 10^{-5} - 4 \times 10^{-4}$ m/sec.). The area of the building was over 800 sq.m.

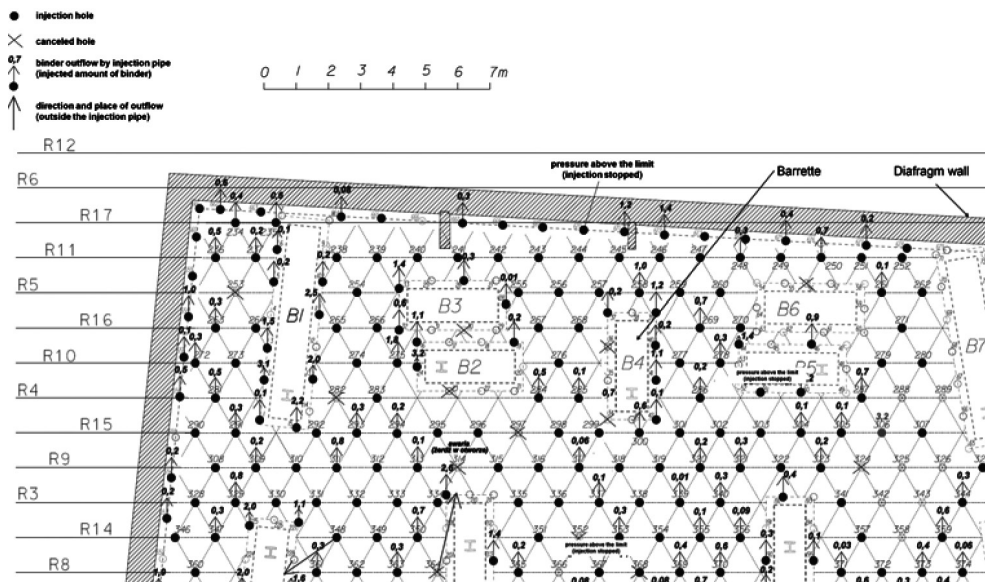


Fig. 5. Injection holes network – horizontal flow barrier

Based on geological investigation and filtration modeling, as well as on stability analysis, a horizontal barrier inside diaphragm wall was designed. The thickness of the barrier was 5.5 m. The barrier was constructed 24.0–29.5 m below ground level. For low pressure injection method and binder based on modified clay were selected for job execution.

Two groups of injection holes were designed (Fig. 5):

- based holes in triangle network (1.25 m spacing),
- special holes, parallel to diaphragm wall and barrettes lateral surfaces.

The goal of based holes was the creation of regular and continuous layer of stabilized and water-proofed soil. Special holes were designed for the additional sealing of contact between soil and lateral surfaces of the diaphragm walls sections and barrettes.

The Injection was made at 0.5 m intervals, from bottom to top of injected thickness.

The order of injection was based on the sequential spatial densification of holes and it was fixed during the job, based on analysis of recorded injection data. Fig. 6 shows sample data recorded during the job. Depending on injection progress and soil condition, different relationships between the injection flux and pressure can be observed. The natural relationships occurs when pressure increase flux is directly proportional. But in reality, we can observe many different relationships (Fig. 6). Such differences can be caused by:

- rheological parameters of the binder,
- consolidation and moving of particles of soil,
- open and filling canals or free spaces formed during the diaphragm wall execution.

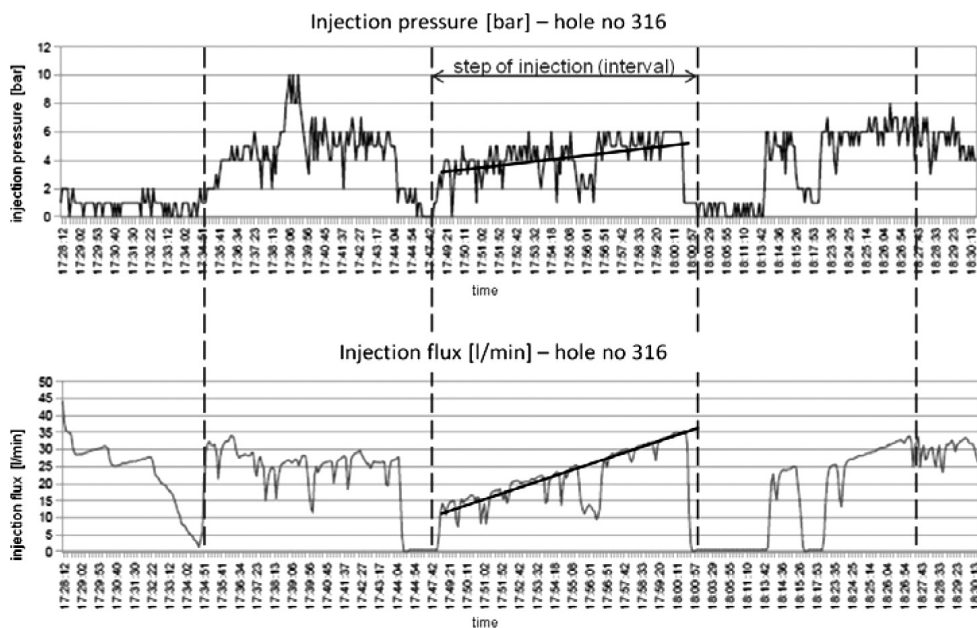


Fig. 6. Sample of main injection parameters fluctuation

All technical data have been collected during the job progress and can be used for analysis and job correction. Fig. 7 and 8 show sample of the 3D model of soil saturation by the binder. As input data recorded information about the amount of the binder injected in each 0.5 m interval were used. Points data can be estimated to spatial continuous 3D model using geostatistical methods.

In case of the Prosta Tower, the input data was estimated using the krigging method (Gaussian semi-variation function) and normalized for accordance with total binder consumption. Such analysis was made during the whole injection works and it is the basis for managing the works.

The Prosta Tower Project was a very difficult but successful job. During this Project, 816 injection holes were drilled (21 021 m of drilling) and $\sim 430 \text{ m}^3$ of binder was injected. The maximum amount of binders injected into holes was $\sim 7.2 \text{ m}^3$ (designed $0.75 \text{ m}^3/\text{hole}$). Probably, it was an effect of the anthropogenic changes of soil structure during a barrettes and diaphragm wall execution. The effects of the executed injection were as follows:

- groundwater table drawdown $S \sim 13$ m (inside excavation),
- average filtration coefficient of barrier $k \sim 6 \times 10^{-8}$ m/sec.,
- total water inflow to excavation $Q \sim 2.9$ m³/h,
- no groundwater table drawdown outside diaphragm wall,
- guarantee of stability of excavation bottom.

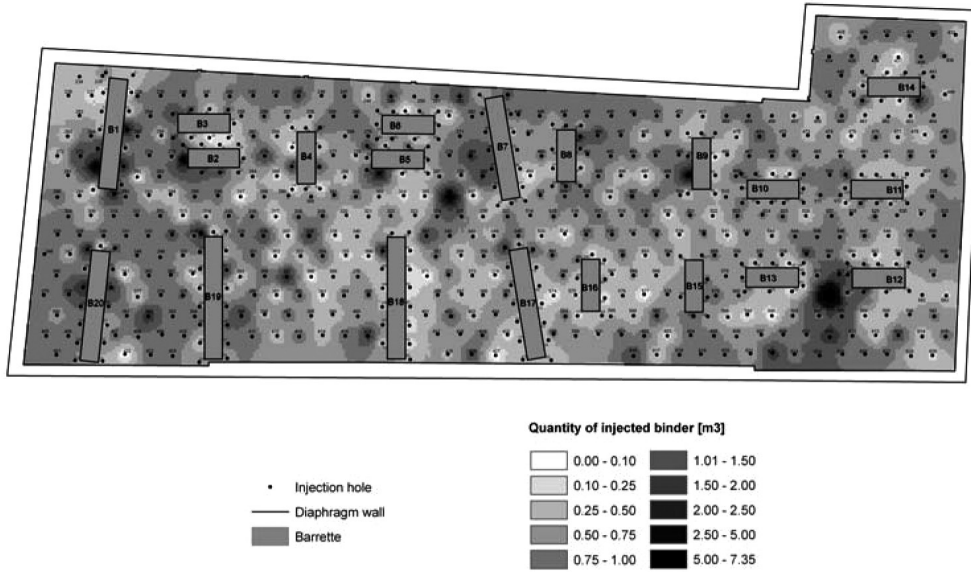


Fig. 7. Spatial distribution of soil saturation by binder as amount of binder injected to whole thickness of barrier (geostatistical model of barrier)

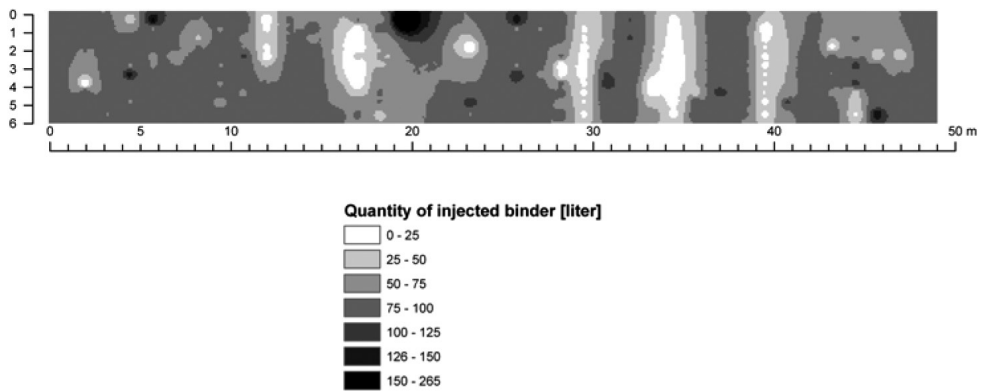


Fig. 8. Sample cross-section of the 3D model of spatial distribution of soil saturation by binder (geostatistical model of barrier)

5. Conclusions

1. Although grouting isn't the most popular method, it is a very flexible and effective method for the reinforcement and sealing of soil and rocks. Grouting can find an application in many solving engineering problems, where other methods cannot be used.
2. The most important aspect of injection is the good selection of liquid and solid binder parameters, dedicated to job requirement and soil or rocks conditions.
3. Limitations of grouting application in Poland are connected with problems of accessibility to good methods and tools for soft and easy designing of injection. There are no effective and certainly mathematical models, well described injection phenomena. Development of such tools will make this method more popular and understand.
4. In engineering practice, the uncertainty of the grouting method can be managed by:
 - good and precise investigation of water-soil conditions,
 - permanent analysis of the technical parameters of injection, during job progress,
 - flexible approach to grouting design, allowed current correction of the designed assumptions.

References

- [1] Kuś R., Słowikowski D., *Zastosowanie wybranych technologii uszczelniania podłoża gruntowego w budownictwie hydrotechnicznym – wieloletnie doświadczenia PRGW*, Europejskie Sympozjum Współczesne Problemy Ochrony Przeciwpowodziowej, Paryż–Orlean 28–30 marca 2012.
- [2] Bouchelanghem F., Vulliet L., *Mathematical and numerical filtration-advection-dispersion model of miscible grout propagation in saturated porous media*, IJNAMG 2001.
- [3] Instytut Techniki Budowlanej, Raport z badań iłu hydroizolacyjnego z Bełchatowa nr LG00-02511/10/ZOONG, Warszawa, listopad 2010.
- [4] PRGW G. Janik R. Kuś Sp.j., *Zastosowanie ultradrobnych spoiw na bazie gliny do wykonywania przesłon hydrizolacyjnych*, Projekt badawczy – SPO WKP Nr Projektu: WK P_1/1.4.1/1/2006/69/69/623/2006, 2009.
- [5] Słowikowski D., Kuś R., Izak P., *Zastosowanie spoiw ilowo-cementowych dla potrzeb poprawy warunków geotechnicznych gruntów w budownictwie hydrotechnicznym*, Polska Ceramika 2012, VII Międzynarodowa Konferencja Naukowo-Techniczna, Kraków 9–12 września 2012.
- [6] Wójcik Ł. Izak P., Kuś R., *Uszczelniające spoiwa ilowo-cementowe mikrostruktura i właściwości*, Europejskie Sympozjum Współczesne Problemy Ochrony Przeciwpowodziowej, Paryż–Orlean 28–30 marca 2012.

KRZYSZTOF STERNIK*

COMPARISON OF SLOPE STABILITY PREDICTIONS BY GRAVITY INCREASE AND SHEAR STRENGTH REDUCTION METHODS

PORÓWNANIE PROGNOZ STATECZNOŚCI SKARPY METODAMI ROSNĄCEJ GRAWITACJI I REDUKCJI WYTRZYMAŁOŚCI

Abstract

The finite element method has become the most widespread method of analyzing slope stability. Its advantage over the limit equilibrium method (the method of slices) has been proven in many publications. The most commonly applied FEM computational scheme in slope stability calculations is the shear strength reduction (SSR) method. Another way of analysing slope stability by FEM is the gravity increase (GI) method. The latter method may not be applied unconditionally. The paper contains a comparison of results obtained by the SSR, GI and modified Bishop's methods. A good agreement of the results produced by the SSR and the modified Bishop's methods has been confirmed. Overestimation of the safety factor by the GI method in the case of using the linear Mohr-Coulomb criterion has been shown.

Keywords: finite element method, limit equilibrium method, slope stability

Streszczenie

Metoda elementów skończonych stała się powszechnie stosowanym narzędziem do analizy stateczności skarpy. Jej przewagę nad metodami równowagi granicznej (metodami paskowymi) wykazano w licznych publikacjach. W ramach analiz stateczności MES najczęściej stosowana jest strategia redukcji wytrzymałości na ścinanie. Innym podejściem jest strategia rosnącej grawitacji, jednak nie może ona być stosowana bezkrytycznie. W artykule zaprezentowano porównanie wyników obliczeń wartości współczynnika bezpieczeństwa metodą redukcji na ścinanie, rosnącej grawitacji i uproszczoną metodą Bishopa. Pokazana została zbieżność wyników uzyskiwanych metodą redukcji wytrzymałości na ścinanie oraz metodą paskową Bishopa oraz przeszacowanie stateczności skarpy w metodzie rosnącej grawitacji w przypadku zastosowania tradycyjnego liniowego warunku Coulomba-Mohra.

Słowa kluczowe: metoda elementów skończonych, metoda równowagi granicznej, stateczność skarpy

* Ph.D. Krzysztof Sternik, Department of Geotechnics and Roads, Faculty of Civil Engineering, Silesian University of Technology.

Symbols

F_s	–	safety factor
\mathbf{d}	–	displacement vector
$\mathbf{B}(\mathbf{x})$	–	strain-displacement matrix at a spatial point \mathbf{x}
$\mathbf{N}(\mathbf{x})$	–	matrix of shape functions at a spatial point \mathbf{x}
ρ	–	density
\mathbf{g}	–	gravity
$\dot{\mathbf{g}}$	–	gravity rate
t	–	parametric time
\mathbf{t}	–	surface tractions prescribed on the part S_t
$\boldsymbol{\sigma}$	–	stress corresponding to the displacement \mathbf{d}
c	–	cohesion
ϕ	–	friction angle

1. Introduction

Slope stability can be defined as a condition in which the body forces generated by gravity together with the load at the top (crest) and internal forces in the massif are in equilibrium. Instability occurs if this condition is not met. Instability may arise as a result of the mechanism developed along a continuous zone, often called a slip surface.

Various approaches to the solution of the slope stability problem have been classified into four groups [5]:

- 1) the limit equilibrium method;
- 2) the slip line method;
- 3) the finite element method;
- 4) a combination of the above 3 groups.

A traditionally slope stability problem was analysed by means of the limit equilibrium method (method of slices by Fellenius, Bishop, Janbu, Morgenstern and Price, Spencer). Description of these methods can easily be found in the literature (e.g. [3–5]). Limit equilibrium methods are still under development. The closed-form solutions satisfying both equilibrium of moments and forces in 2D [11] and 3D [12] were proposed recently.

To assess the level of safety of a slope (natural or cut), shear stresses acting in the soil body are compared with the shear strength (ultimate shear stress) on a priori assumed surface and the parameter called the factor of safety is calculated:

$$F_s = \frac{\text{shear strength of soil}}{\text{shear stress required for equilibrium}} \quad (1)$$

The limit equilibrium methods mentioned above suffer from substantial drawbacks:

- they do not take into account the history of slope formation, i.e. stress-strain (loading) history;
- they assume a given shear resistance along a priori assumed slip line (most often circular);
- the methods provide no information as to the magnitudes of strains within the slope nor any indication about how they may vary along the slip surface;

- as a consequence, there is no guarantee that the shear resistance will take the peak or residual value simultaneously on the whole slip surface which is the assumption of all limit equilibrium methods;
- a rigid-plastic constitutive model with the Mohr-Coulomb limit state surface is commonly used in analyses;
- as a consequence, failure occurs only if the stress path reaches the limit state surface whereas in some real cases, it may occur before reaching the failure condition.

Numerical methods for solving boundary value problems offer much more powerful tools for analysing slope stability [1, 6]. With the finite element method slope, stability may be analysed by making use of constitutive relations and the procedure called the shear strength reduction. Determination of the factor of safety consists in successive decreasing of strength parameters with respect to their initial values. A failure criterion met along an arbitrary continuous line indicates the loss of stability which is close to reality.

Moreover, as noted in [15], the limit equilibrium method is of an approximate and arbitrary nature and the results obtained from this method are neither upper bounds nor lower bounds on the true collapse loads. The finite element method can be used to calculate upper and lower bound solutions for slope stability, though some special approach is necessary [15]. This attempt delivers evaluations for the collapse load calculated in limit analysis.

In the paper, two alternative methods of finite element stability analysis are presented. In the first, the strength characteristics of the soil mass are held constant, and the gravitational loading on the slope system is increased until failure is initiated by a well-defined mechanism. In the second approach, the gravity loading on the slope system is held constant, while the strength parameters of the soils are gradually decreased until a well-defined failure mechanism develops. The first method is called the gravity increase method [8, 14] while the second is the well known shear strength reduction method [1, 3, 6, 8–10, 14, 15]. The results from these two approaches are compared with the results of the modified Bishop's limit equilibrium method.

2. Force equilibrium in the non-linear finite element method

The response of soil slope subjected to gravitational loading is treated as a general materially non-linear elliptic boundary value problem. The load is applied in incremental steps. In the n^{th} step, the equilibrium between internal and external forces within the soil body is searched, which due to the non-linearity of the soil model, means that the residual forces meet the requirement:

$$\mathbf{r}_n = \mathbf{f}_{\text{int}}(\mathbf{d}^{(n)}) - \mathbf{f}_{\text{ext}}(\mathbf{d}^{(n)}) = 0 \quad (2)$$

where:

$$\mathbf{f}_{\text{int}}(\mathbf{d}^{(n)}) = \int_V \mathbf{B}^T(\mathbf{x}) \boldsymbol{\sigma}(\mathbf{B}(\mathbf{x}) \mathbf{d}^{(n)}) dV \quad (3)$$

$$\mathbf{f}_{\text{ext}}(\mathbf{d}^{(n)}) = \int_{S_f} \mathbf{N}^T(\mathbf{x}) \mathbf{t}^{(n)} dS + \int_V \rho \mathbf{N}^T(\mathbf{x}) \mathbf{g}^{(n)} dV \quad (4)$$

- $\mathbf{d}^{(n)}$ – displacement vector at n^{th} step,
- $\mathbf{B}(\mathbf{x})$ – strain-displacement matrix at a spatial point \mathbf{x} ,
- $\mathbf{N}(\mathbf{x})$ – matrix of shape functions at a spatial point \mathbf{x} ,
- ρ – density,
- \mathbf{g} – gravity,
- \mathbf{t} – surface tractions prescribed on the part S_r ,
- $\boldsymbol{\sigma}$ – stress corresponding to the displacement $\mathbf{d}^{(n)}$.

The slope is stable with respect to the applied loads as long as equilibrium can be achieved between the internal and external forces, than a solution to equation (2) exists. When this balance can no longer be achieved due to increased gravity loading and achieving soil strength, the slope becomes unstable, since the equilibrium solution satisfying equation (2) no longer exists.

3. Gravity increase (GI) method

The analysis of stability by the gravity increase method assumes the external forces increase due to increasing gravity \mathbf{g} and the equilibrium solution satisfying equation (2) can no longer be obtained. Monotonically increasing gravity brings external forces on the edge of stability when the strength of the soil is reached.

Gravity increases according to the formula:

$$\mathbf{g} = \dot{\mathbf{g}} \cdot t \quad (5)$$

where:

- $\dot{\mathbf{g}}$ – a prescribed vector specifying the direction of gravity loading and its rate of increase with time, and t is a parametric time variable.

Prescribed in this manner, gravitational acceleration vector $g(t)$ increases and the limit analysis problem reduces simply to finding the largest time $t = t_{\text{limit}}$ for which a global equilibrium solution of equation (2) exists. The limiting acceleration due to gravity in the system is then:

$$\mathbf{g}_{\text{limit}} = \dot{\mathbf{g}} \cdot t_{\text{limit}} \quad (6)$$

The time t_{limit} is not a known a priori. It is approached asymptotically. For values of $t > t_{\text{limit}}$ solution of equation (2) does not exist.

Since gravitational loading induces slope failure, the gravity-based factor of safety against slope failure is given by:

$$F_{s\,gi} = \frac{g_{\text{limit}}}{g_{\text{actual}}} \quad (7)$$

where:

- g_{actual} – representative actual acceleration due to gravity in the slope analysed, i.e. 9.81 m/s².

The value of the safety factor is greater than unity for a stable slope. The higher the value of safety factor, the more stable the slope is.

It has been found in [8] that a good measure of slope safety is to associate g_{limit} with the abrupt increase of acoustic emission rate or a dramatic increase in the nodal displacement within the elements. Nevertheless, in this paper nonconvergence of the FEM solution and displacement variation in the slope body is adopted.

4. Shear strength reduction (SSR) method

In this technique, the basic continuum equilibrium problem and the corresponding finite element formulation for each stage of analysis is the same as for the gravity increase method. A series of trial factors of safety are used to adjust the cohesion, c , and the friction angle, ϕ , of soil as follows:

$$c_{\text{trial}} = \frac{1}{F} c \quad (8a)$$

$$\phi_{\text{trial}} = \arctan\left(\frac{1}{F} \tan \phi\right) \quad (8b)$$

The adjusted cohesion and friction angle of the soil layers are re-inputted in the model for equilibrium analysis. The factor of safety is sought when the specific adjusted cohesion and friction angle make the slope unstable.

In general, the shear strength parameters of the soil can be reduced by utilizing a monotonically decreasing time function to govern the shear strength properties of the soil mass. A typical shear strength parameter X for the soil mass is governed in time as follows:

$$X(t) = X_{\text{base}} \cdot f(t) \quad (9)$$

where:

X_{base} – the actual strength parameter and t is again a parametric time variable (pseudo-time).

In such a problem, gravity loading is applied to the soil mass and remains unchanged after the stability analysis is launched. The initially high values of soil parameters determining its strength decrease monotonically until solution of equation (2) can no longer be found. Thus, the problem again concerns finding the maximum value of parametric time $t = t_{\text{limit}}$ for which the boundary value problem is on the verge of failure. In fact, the shear strength reduction method is a repeatedly solved problem of statics with varying parameters of soils in a model.

The sought time corresponds to the safety factor for the strength reduction method:

$$F_{sr} = \frac{X_{\text{base}}}{X(t_{\text{limit}})} = \frac{1}{f(t_{\text{limit}})} \quad (10)$$

5. Numerical analyses

5.1. Assumptions

The stability analyses have been performed for a slope with the crest loaded with 90 kPa placed 5 m away from the edge of the slope. The slope is made of homogeneous clay. The geometry of the slope comprises four heights $H = 6, 12, 20, 40$ m and two angles of inclination $\alpha = 30^\circ$ and 45° (Fig. 1).

There were two sets of material parameters assumed for the analyses with the Mohr-Coulomb elastic – perfectly plastic model. Values of elastic modulus $E = 30$ MPa, Poisson's ratio $\nu = 0.3$, density $\rho = 2000$ kg/m³ are common for both sets. Strength parameters differ for inclinations 30° and 45° . For the 30° slope, cohesion is 10 kPa and the friction angle is 25° whereas for the 45° slope, cohesion is 30 kPa and the friction angle 30° . In both cases, non-associated flow rule has been assumed with a dilatancy angle $\psi = 0^\circ$.

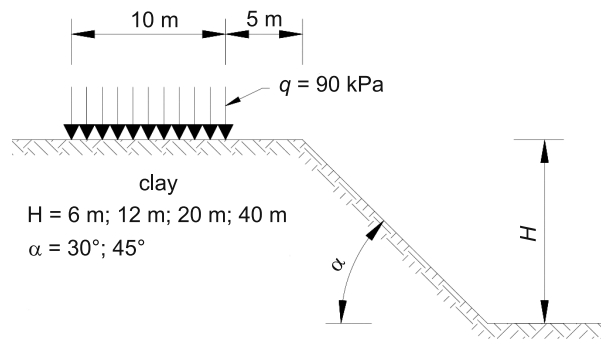


Fig. 1. Shape of slope under analysis

The analyses have been performed with the FEM program Z_Soil [16]. A family of 2D isoparametric elements with 1st order interpolation function is implemented in the program.

To simulate incompressible and highly dilatant plastic media, the Enhanced Assumed Strain method (EAS) has been used in the program.

5.2. Results

Analyses of slope stability have been performed by both shear strength reduction and gravity increase methods. The results have been compared with the results of the limit equilibrium analysis by the modified Bishop's method.

The results of computations by the shear strength reduction method are presented in Fig. 2. Concentrations of shear strain (the second invariant of strain deviator) forming shear bands can be seen. These are incremental values that occur in the last stage of each analysis. At this stage, further reductions of the soil strength give rise to the failure mechanism and divergence in computations.

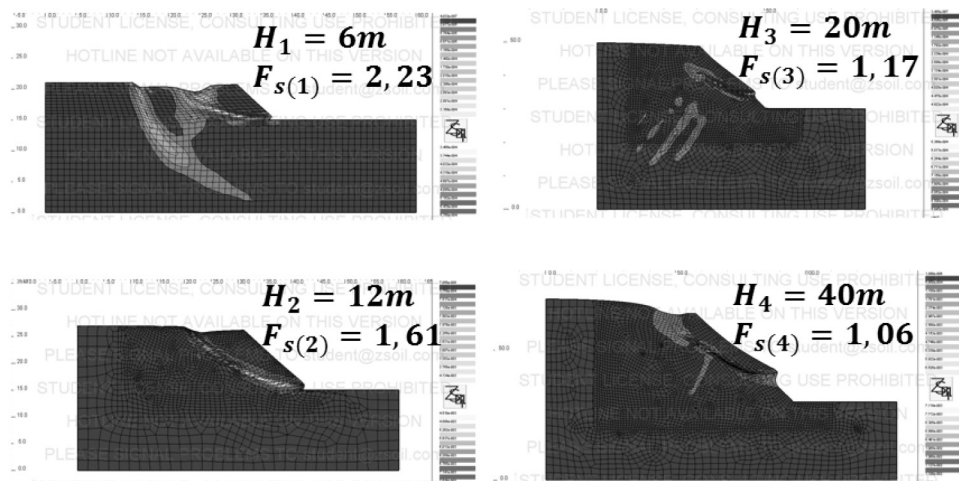


Fig. 2. Deformed models of slope inclined at 45° showing failure mechanisms in the shear strength reduction method

In all cases, the failure mechanisms are well defined. For the 6 m slope, two simultaneous mechanisms are predicted; one starting at the toe, the other deep in the base. The higher the slope is, the higher the failure zone starts on its surface.

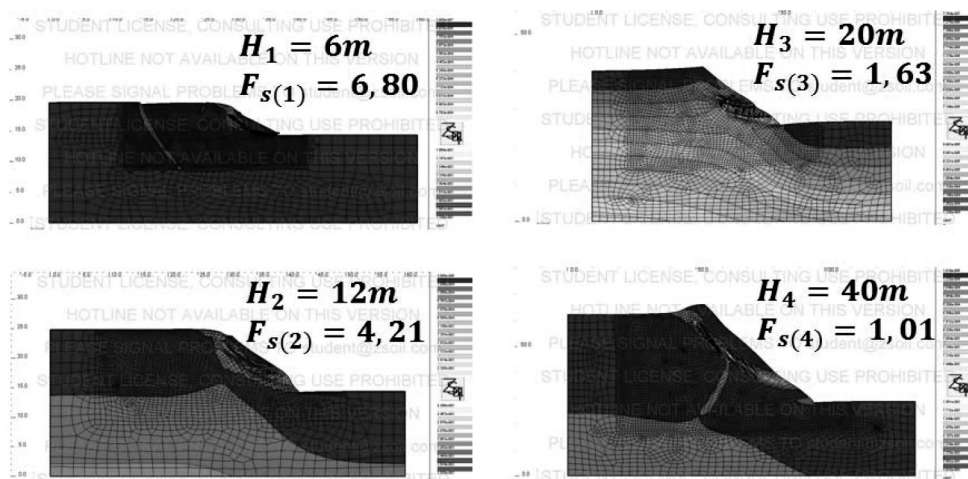


Fig. 3. Deformed models of slope inclined at 45° showing failure mechanisms in the gravity increase method

Results of computations by the gravity increase method for the 45° slope are presented in Fig. 3. Values of the factor of safety are significantly larger than in the shear strength reduction method for slopes up to 20 m. In the case of the 40 m slope, both methods predict virtually identical factors of safety.

As in the case of the shear strength reduction method, two failure zones occur in the 6 m slope. In the 20 m slope, the failure mechanism predicted by the increase gravity method is not unique. There are two failure zones starting at the toe and at one-third of the slope's height.

The results of computations by Bishop's method are close to the results achieved by the shear strength reduction method. For all slope's heights, Bishop's method yields somewhat higher results than shear strength reduction method, but it can be admitted that for homogeneous slopes, the values of the factor of safety predicted by both methods are in good agreement. These findings are comparable to the results reported in, for example [6, 8, 14].

The gravity increase method yields significantly larger factors of safety than the shear strength reduction method. Such results were expected since the traditional Mohr-Coulomb failure criterion has been used in the analysis. This criterion is a linear function of stresses. In such a case, in the absence of additional loads, with increasing gravity, the mean stresses in the soil increase faster than the shear stresses. The rate of strength gain in soil under increasing gravity loading, exceeds the rate of shear stress increase, and the slope does not develop a failure mechanism.

Such a case is depicted in Fig. 4, where a slope of sand inclined at 33° has been analysed until an increase of gravity upto 20 g. The friction angle for sand has been assumed at 35°. It is well known that such a slope is at the verge of stability. The shear strength reduction method yields the factor of safety $F_s = 1.09$ whereas the increase gravity method does not reveal failure mechanism even for a gravity field of 20 g ($F_s = 20$).

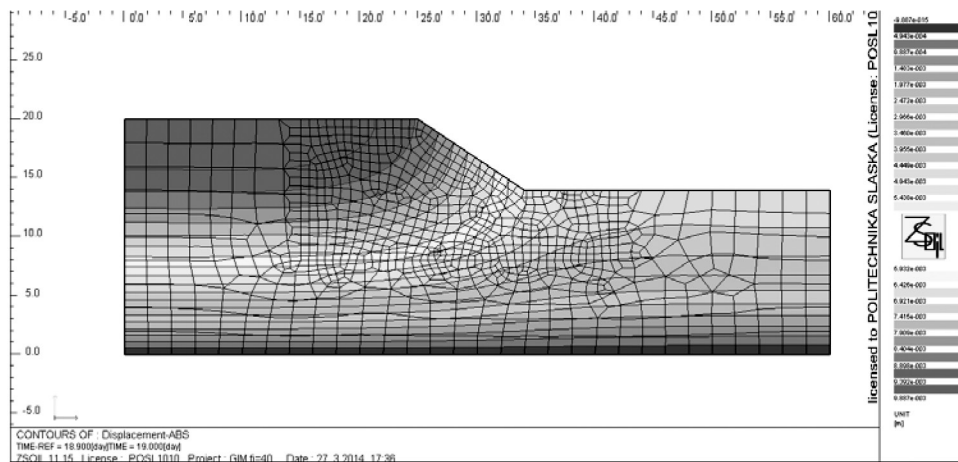


Fig. 4. Displacements of sandy slope inclined at 33° without failure mechanisms in gravity increase method at gravity field increased 20 times

In the problem considered, an additional load of 90 kPa on the crest of the slope is present. In addition, the slope is not comprised of purely frictional material. The cohesive part of the strength is not influenced by the mean stress. Since shear stresses due to gravity and external loading increase faster than the strength in the superficial zone, slip zones develop near the surface of the slope for all heights.

Factors of safety computed with all methods for both repose angles of 30° and 45° are presented in Table 1.

Table 1

Comparison of factors of safety computed by different methods

Height of a slope H [m]	Factor of safety F_s					
	repose angle 45°			repose angle 30°		
	Bishop's method	Shear Strength Reduction	Gravity Increase	Bishop's method	Shear Strength Reduction	Gravity Increase
6	2.33	2.23	6.80	1.67	1.47	10.61
12	1.69	1.61	4.21	1.41	1.30	3.36
20	1.39	1.17	1.63	1.27	1.11	2.01
40	1.11	1.06	1.01	1.09	1.01	1.01

For small height of slope, the strength reduction method produces stability factors smaller (and thus more conservative) than the gravity-loading method of analysis. At larger slope height, both methods tend to give stability factors and failure mechanisms that are somewhat closer to each other.

6. Summary

Overcoming a set of drawbacks that feature the limit equilibrium method, the finite element method came into widespread use within engineering practice. The shear strength reduction method is currently the most frequently used method of analyzing slope stability by the finite element method. Nevertheless, the gravity increase method is also applied in stability analysis.

The criterion that is most often used for judging the slope failure is nonconvergence of the FEM solution, but there are other possible criteria including the formation of a critical failure surface, displacement variation in the slope body, acoustic emission event rate or negative second order work in a closed area within a slope [2, 7, 13]. In the paper, the first of them has been used for both shear strength reduction and gravity increase methods.

From the results obtained from the analyses, it follows that the application of the traditional Mohr-Coulomb failure criterion in the gravity increase method leads to a significant overestimation of a factor of safety in comparison with the shear strength reduction method in the case of relatively low slopes. The discrepancy between the values of the factor of safety for higher slopes (over 20 m) obtained from both methods become smaller.

Once again, the good agreement between factors of safety computed by the shear strength reduction method and the modified Bishop's method has been shown. Such results are well known from the literature [1, 10, 15]. However, it must be remembered that this is valid only for homogeneous slopes.

The present study uses only the simple elastic – perfectly plastic Mohr-Coulomb model. Since many of soil the deposits exhibit softening behaviour, other more advanced models which also take into account this aspect should be considered in stability calculations. Such

an analysis should be of special interest in the case of rock slopes. Some efforts have already been put into using a simple brittle damage model in gravity increase FEM slope stability analysis [8].

References

- [1] Alkasawneh W., Malkawi A.I.H., Nusairat J.H., Albataineh N., *A comparative study of various commercially available programs in slope stability analysis*, Computers and Geotechnics 35, 2008, 428-435.
- [2] Darve F., Laouafa F., *Instabilities in granular materials and application to landslides*, Mech. Cohes-Frict. Mater., 5, 2000, 627-652.
- [3] Duncan J.M., *State of the art: limit equilibrium and finite element analysis of slopes*, Journal of Geotechnical Engineering, Vol. 122, No. 7, 1996, 577-596.
- [4] Duncan J.M., Wright S.G., *Soil Strength and Slope Stability*, J. Wiley & Sons Inc., Hoboken, New Jersey, 2005.
- [5] Espinoza R.D., Repetto P.C., Muhunthan B., *General framework for stability analysis of slopes*, Géotechnique, Vol. 42, No. 4, 603-615.
- [6] Griffiths D.V., Lane P.A., *Slope stability analysis by finite elements*, Géotechnique, Vol. 49, No. 3, 1999, 387-403.
- [7] Laouafa F., Darve F., *Modelling of slope failure by a material instability mechanism*, Comp. and Geotech., 29, 2002, 301-325.
- [8] Li L.C., Tang C.A., Zhu W.C., Liang Z.Z., *Numerical analysis of slope stability based on the gravity increase method*, Computers and Geotechnics, 36, 2009, 1246-1258.
- [9] Nakamura A., Cai F., Ugai K., *Embankment basal stability analysis using shear strength reduction finite element method*, 10th Int. Symp. on landslides and engineered slopes, CRC Press, Boca Raton, 2008, 851-856.
- [10] Matsui T., San K.-C., *Finite element slope stability analysis by shear strength reduction technique*, Soil and Foundations, Vol. 32, No. 1, 1992, 59-70.
- [11] Pantelidis L., D.V. Griffiths D.V., *Stability of earth slopes. Part I: two-dimensional analysis in closed-form*, Int. J. Numer. Anal. Meth. Geomech., 37, 2013, 1969-1986.
- [12] Pantelidis L., D.V. Griffiths D.V., *Stability of earth slopes. Part II: three dimensional analysis in closed-form*, Int. J. Numer. Anal. Meth. Geomech., 37, 2013, 1987-2004.
- [13] Sternik K., *Slope stability analysis based on Hill's condition*, Proc. XVIII Scientific Conf. Computer Methods in Design and Anal. of Hydrotechnical Structures Korbielów 2006 (in Polish), 113-126.
- [14] Swan C.C., Seo Y.-K., *Limit state analysis of earthen slopes using dual continuum/ FEM approaches*, Int. J. Numer. Anal. Meth. Geomech., 23, 1999, 1359-1371.
- [15] Yu H.S., Salgado R., Sloan S. W., Kim J.M., *Limit Analysis Versus Limit Equilibrium for Slope Stability*, J. Geotech. Geoenv. Engng., Vol. 124, No. 1, 1998, 1-11.
- [16] Zimmermann Th., Truty A., Urbański A., Podleś K., *Z_Soil.PC 2010 3D user manual, Theory, Tutorials and Benchmarks, Data Preparation*, Elmpress Int. & Zace Services Ltd, Switzerland 2010.

CEZARY TOŚ*

SUPERVISED CLASSIFICATION OF LASER SCANNING DATA IN THE ASSESSMENT OF TECHNICAL CONDITIONS OF MASONRY CONSTRUCTIONS

KLASYFIKACJA NADZOROWANA DANYCH SKANINGOWYCH W OCENIE STANU TECHNICZNEGO KONSTRUKCJI MUROWYCH

Abstract

In the paper is presented the application of supervised classification to determine the technical conditions of masonry structures. The supervised classification of the registered intensity of laser beam reflection and images from a digital camera are tested to detect dampness, salt stamps and vegetation cover on the surface of the retaining wall of levees. The analyses are referred to two clouds of points obtained with the use of two types of laser scanners which are using different wavelengths. In both cases, the intensity of reflections improved the results of supervised classification.

Keywords: monitoring of structure, laser scanning, laser reflection intensity, image processing, supervised classification

Streszczenie

W artykule przetestowano możliwości wykorzystania klasyfikacji nadzorowanej w ocenie stanu technicznego konstrukcji murowej. Przeprowadzono analizy wykorzystujące zdjęcia wykonywane przez skaner oraz rejestrowaną intensywność odbicia promienia laserowego do wykrywania zawilgoczeń, wykwitów solnych oraz pokrycia roślinnego fragmentu muru oporowego wałów przeciwpowodziowych. Opracowywane chmury punktów pochodziły z dwóch typów skanerów laserowych pracujących na różnych długościach fali. W obydwu przypadkach wykorzystanie intensywności odbicia promienia laserowego w klasyfikacji nadzorowanej obrazów spowodowało nieznaczne polepszenie wykrywania ww. zjawisk na powierzchni muru.

Słowa kluczowe: monitoring konstrukcji, skaning laserowy, intensywność odbicia promienia laserowego, klasyfikacja nadzorowana obrazów

* Ph.D. Cezary Toś, Institute of Geotechnics, Faculty of Environmental Engineering, Cracow University of Technology.

1. Introduction

The evaluation of the technical condition of the constructions includes the recognition of damage in wastages as well as the changes of the constructional element's geometry. Moreover, unfavourable phenomena on the surface of the object such as dampness and the occurrence of vegetation cover and salt stains, which are evidence of lack of the construction's resistance to water, are being inventoried [1, 2].

The usefulness of laser scanning in terms of examining the geometry of building constructions is unquestionable and has been described thoroughly in literature [3, 4]. The evaluation of the remaining factors which influence the technical condition of building construction requires the individual approach. The traditional way of inventorying these phenomena is based on the visual and organoleptic evaluation of the surface's condition, supported by expert experience. The visual evaluation can be conducted on the basis of the pictures of the object taken with the use of the scanning device. The disadvantage of this solution lies in the influence of the disturbing factors like surface illumination or an unclean surface. In connection with this, the question emerges: if taking into consideration the additional information carried by the measured laser beam intensity of reflection would improve the quality of classifying these phenomena. In this paper, these data have been analyzed by means of using the supervised classification method. Researches embraced the fragment of the stone retaining wall of the Vistula boulevards in Krakow. The object of the analysis included clouds of points obtained with the use of two laser scanners, i.e. phase based FARO FOCUS^{3D} as well as pulse based TOPCON GTS 1500.

2. The application of the recorded intensity of laser beam reflection in the detection of unfavourable phenomena

The inventory of dampness, salt stains and vegetation cover on the surface of masonry structure is conducted in situ or on the basis of visual analysis of pictures of the object. This analysis can be automated by using the procedures of supervised classification applied in remote sensing.

The purpose of the research embraced comparing the results of classification of the fragment of the stone retaining wall of the Vistula boulevards in two cases. The analysis of the first case was based merely on three spectral bands (red, green and blue) derived from the photo taken with the scanner's in-built camera. In the second case, the set of bands was supplemented with the band of intensity of reflection.

The laser beam, which is incident on the surface of the object, undergoes scatter and absorption, which results in the fact that only part of the signal is recorded. The impact of various factors on the intensity of reflection have been examined by many authors [5–8]. What is essential in the proper classification of dampness, salt stains and vegetation cover is color, humidity and the structure of the object's surface. Disturbing factors include: distance, incidence angle of the beam on the surface and less significantly, surface illumination. In the conducted research, the impact of the latter was reduced by means of choosing the test field in a shaded place (homogeneous illumination) (Fig. 1) as well as applying the so-called normalized intensity in the calculation. This value is recorded in 8 bits [0–255] for each

point of the cloud and it takes into account the influence of the distance on the object [5]. The influence of the incidence angle of the laser beam on the surface of the object can be eliminated only under laboratory conditions.



Fig. 1. Object of research

The separate issue is the wavelength of the scanners. The usage of the scanner with visible wavelengths (380–780 nm) seems to be ineffective in the classification when photos from the digital camera are used as well. Therefore, the information which carries the intensity of reflection is strongly correlated with the proper band from photo. In connection with that, the application of near infrared or mid infrared lasers (780–5000 nm) appears to be more beneficial. The important factor is the principle of operation of the scanner – phase based or pulse based. By taking this information into consideration, two scanners, FARO FOCUS^{3D} which uses the wavelength 785 nm and GTS 1500 TOPCON with laser working on the wavelength 1535 nm, were applied (Fig. 2).



Fig. 2. Scanner FARO FOCUS 3D and TOPCON GTS 1500

A wide spectrum of methods of classification could have been applied in the research, nevertheless, the pixel-based classification was used. This was due to the fact that it is impossible to define the shape of texture and the proximity of those phenomena initially,

which information is taken into consideration in the object-oriented classification. The methods which apply hard classifiers were chosen from among the supervised classification methods due to the simplicity of the result's interpretation. From among three of them (*Pieped*, *Mindist*, *Maxlike*) the Maximum likelihood classification method (*Maxlike*) based on the Bayesian classifier produces the best results.

3. The results of the classification of images from the FARO scanner

The colors were put on the cloud of points obtained from the FARO scanner by means of using photos taken with the device's in-built camera. The obtained image was separated to create 3 byte binary images representing the bands: red, green, blue (R,G,B). Furthermore, the image of the intensity of the laser beam reflection was prepared (INT). The laser in FARO scanner works with the wavelength 785 nm, i.e. just beyond the red light border. Nevertheless, it transpires that the image of the intensity of reflection (INT) is considerably less correlated with the red band (R) than the green (G) and blue (B) bands. Coefficients of determination R^2 are as follows: 0.84, 0.97 and 0.93 (Fig. 3).

The coefficient of determination for multiple regression which describes the level of a linear relationship between the dependent value from the intensity (INT) band and the independent variables from the R,G,B bands is 0.93.

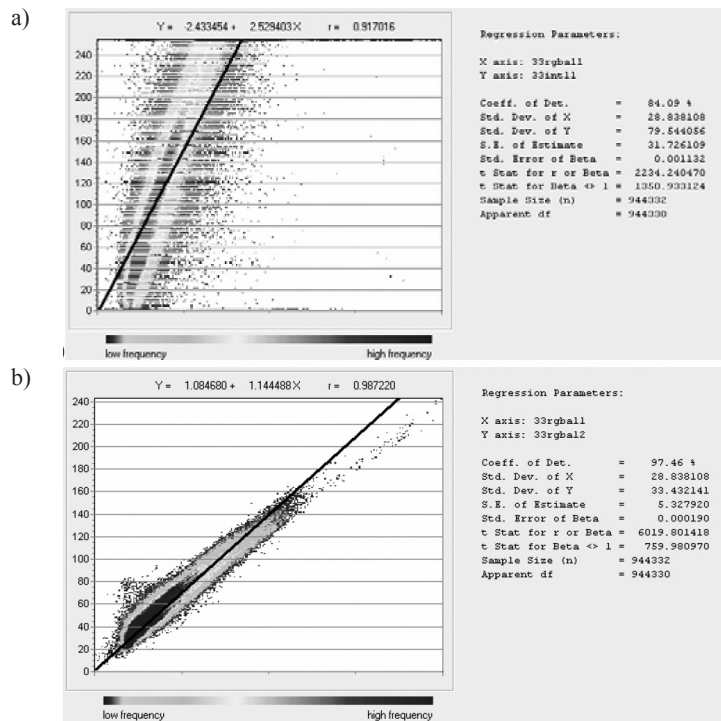


Fig. 3. The results of regression analysis between bands: a) red-intensity, b) red-green for FARO scanner

Three classes were defined for the purpose of the analysis:

- salt,
- dampness,
- vegetation cover.

The class which is defined as the fourth (norm) concerned the area in which any of the above mentioned phenomena occurred. Despite the fact that many attempts have been made to define the training polygons (Fig. 4), not all signatures of classes proved to be fully separable. Jeffreys-Matusita distance for pairwise of signatures oscillated between 0.56 and 1.95 (tab. 1, 2). The optimal value of J.M.-distance is 1.8–2.0 [9, 10]. This results from the poor quality of photos taken with the use of this scanner. Poor separability of signatures has a considerable impact on the final results of the classification.



Fig. 4. Training polygons (white – salt, light grey – vegetation cover, dark grey – dampness, black-norm)

Table 1

J.M. distance for pairwise of signatures for 3 bands: R, G, B – scanner FARO

Classes	vegetation cover	salt	norm
Dampness	1.12	1.22	1.28
Vegetation cover		1.74	1.80
Salt			0.56
The average distance for pairwise of signatures 1.29			

Table 2

J.M distance for pairwise of signatures for 4 bands: R. G. B. INT – scanner FARO

Classes	vegetation cover	salt	norm
Dampness	1.23	1.81	1.53
Vegetation cover		1.92	1.95
Salt			0.58
The average distance for pairwise of signatures 1.51			

However, it should be emphasized that there was a considerable improvement in the signatures of separability for all pairs of classes after the band of the intensity of reflection was incorporated into the analysis. Therefore, making use of this band makes sense due to the fact that it carries additional information about the object.

The classification was conducted twice, by applying the Maximum likelihood classification method (maxlike) with the use of 3 bands R, G, B (Fig. 6) as well as, independently, the use of 4 bands R, G, B, INT (Fig. 7). In both cases, the occurrence of 5% of the unclassified pixels was allowed. In order to verify the obtained results, the unfavorable phenomena were inventoried manually, based on the high resolution photo from the digital camera – Nikon D5100 (Fig. 5). The impact of the incorporation of the band of intensity into the analysis is visible through the change in Cramer’s V coefficient which illustrates the strong correlation between results of supervised classification and manual inventory, as well as the Kappa index of agreement, KIA, which determines the comparability of pictures [11, 12] (tab. 3).

Table 3

Coefficients: Cramer’s V and Kappa index of agreement (KIA) between results of supervised classification and the manual inventory

Coefficient	Classification R, G, B,	Classification R, G, B, INT
Cramer’s V	0.5098	0.5120
Overall Kappa	0.5130	0.5137
Kappa for Norm	0.6037	0.5349
Kappa for Salt	0.5729	0.5941
Kappa for Vegetation cover	0.2082	0.2415
Kappa for Dampness	0.6184	0.6995



Fig. 5. Manual inventory (white – salt, light grey-vegetation cover, dark grey – dampness)



Fig. 6. The results of the supervised classification with the use of bands: R, G, B



Fig. 7. The results of the supervised classification with the use of bands: R, G, B and INT

These coefficients indicate the moderate correlation and comparability of the results of the analyses with the manual inventory. The introduction of the band of intensity resulted in a slight increase of both coefficients. Moreover, there was an improvement in the coefficients of agreement for classes which related to the occurrence of unfavourable phenomena.

4. The results of the classification of images from the Topcon scanner

The algorithm of proceedings which was presented in the previous chapter was repeated for the cloud of points obtained with the use of the scanner TOPCON GLS 1500. According to the expectations, the coefficient of correlation of the band of intensity (INT) with relation to the red (R) band is lower than it was in the case of FARO scanner and is 0.73 (Fig. 8a). The

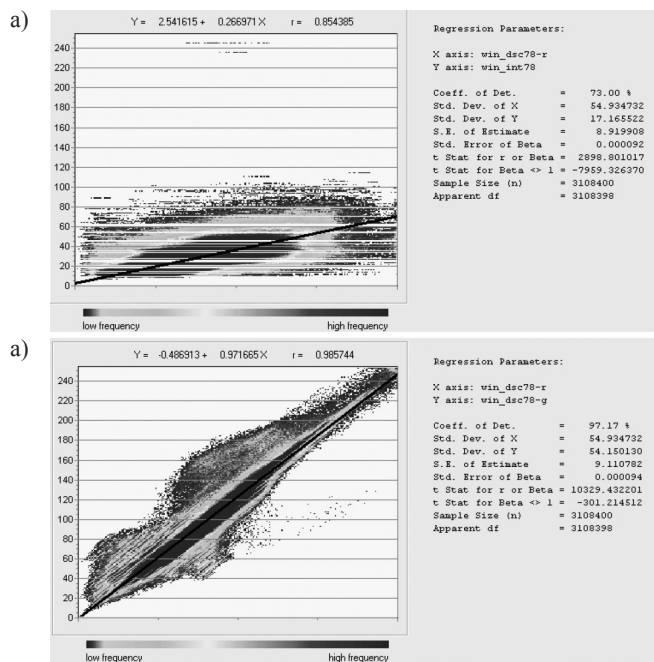


Fig. 8. The results of regression analysis between bands: a) red-intensity b) red – green for TOPCON scanner

relationship between the green and blue bands and the red band remains on the same level, which is as follows: 0.97 (Fig. 8b) and 0.93. Nevertheless, it has to be emphasized that those measurements were taken at a different time and in different weather conditions.

The coefficient of determination for the multiple regression between the dependent value from intensity (INT) band and the independent variables from the R,G,B bands is 0.83.

The JM-distance for the pairwise of signatures was also determined for bands R, G, B and R, G, B, INT (tab. 4, 5).

Table 4

J.M. distance for pairwise of signatures for 3 bands: R, G, B – scanner TOPCON

Classes	Vegetation cover	Salt	Norm
Dampness	1.56	1.98	1.81
Vegetation cover		1.99	1.82
Salt			0.46
The average distance for pairwise of signatures 1.60			

Table 5

J.M. distance for pairwise of signatures for 4 bands: R, G, B, INT – scanner TOPCON

Classes	Vegetation cover	Salt	Norm
Dampness	1.57	1.98	1.83
Vegetation cover		1.99	1.85
Salt			0.7
The average distance for pairwise of signatures 1.65			

It should be noted that as a result of better illumination, a different camera and, simultaneously, better contrast of the photos, the JM-distance for pairwise of signatures for all classes has been improved significantly with regard to the FARO scanner. The fact that the spectral set was supplemented with intensity could not cause any significant improvement in very good coefficients. The exception is the pair of classes *Salt-Norm*, the coefficient of which increased from 0.46 to 0.7.

The results of the supervised classification for bands R, G, B (Fig. 10) and R, G, B, INT (Fig. 11) have been compared with a previously conducted manual inventory (Fig. 9). The introduction of the additional band of intensity to the analysis has not significantly changed the Cramer's V and KIA coefficients for the whole image. Nevertheless, there has been a slight improvement in coefficients KIA for individual classes which concerned the unfavourable phenomena (tab. 6).

Coefficients: Cramer's V and Kappa index of agreement (KIA) between results of supervised classification and the manual inventory

Coefficient	Classification R, G, B,	Classification R, G, B, INT
Cramer's V	0.5520	0.5582
Overall Kappa	0.5726	0.5869
Kappa for Norm	0.5937	0.5667
Kappa for Salt	0.3586	0.3773
Kappa for Vegetation cover	0.4170	0.4206
Kappa for Dampness	0.7063	0.7362

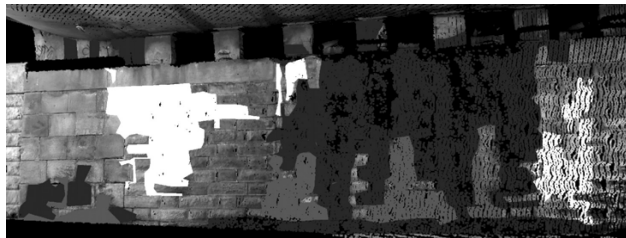


Fig. 9. Manual inventory (white – salt, light grey – vegetation cover, dark grey – dampness)



Fig. 10. The results of the supervised classification with the use of bands: R, G, B.



Fig. 11. The results of the supervised classification with the use of bands: R, G, B and INT

5. Conclusions

On the basis of the previously conducted research, it is possible to formulate the following conclusions:

- All unfavourable phenomena, for instance, salt, vegetation cover as well as dampness, which occur on the surface of the object, can be inventoried by means of using data from the scanner and the supervised classification method. However, in case of masonry structure, its results indicate a moderate correspondence with a reality.
- The results of the classification are highly dependent on the quality of the photos taken with the use of the device's in-built camera.
- The introduction of the intensity of the laser beam reflection as an additional band expands the separability of the pairs of classes in the supervised classification. Nevertheless, it does not improve the results of this classification considerably. This results from the influence of the disturbing factors, like an unclean surface of the object, incidence angle of the beam on the surface and surface illumination. These factors cannot be eliminated in field research.
- The intensity of reflection carries additional information about the object. However, it is not correlated with the bands R, G, B from the photos. It suggests a need for research on algorithms dedicated to this type of data.

Prezentowane wyniki badań, zrealizowane w ramach tematu nr Ś-2/242/DS/2012, zostały sfinansowane z dotacji na naukę przyznanej przez Ministerstwo.

References

- [1] Kucharska-Stasiak E., *Metody pomiaru zużycia obiektów budowlanych*, Przegląd budowlany 2/95, Warszawa 1995.
- [2] Dębowski J., *Determination issue of the technical usage degree in prefabricated concrete slabs*, Technical Transactions vol. 4-A/2007, Cracow University of Technology Press, Cracow 2007, 28-34.
- [3] Kamiński W., Bojarowski K., Dumalski A., Mroczkowski K., Trystuła J., *Possibilities of using laser scanner Scanstation from LEICA to research deformation of building structures*, Technical Transactions vol. 2-Ś/2008, Wydawnictwo Politechniki Krakowskiej, Kraków 2008, 139-147.
- [4] Maciaszek J., *Laser scanning as a new technology in the rendering and visualisation of historic salt caverns*, Mineral Resources Management, vol. 24, Part. 3/2, Cracow 2008, 197-210.
- [5] Pesci A., Teza G., *Effects of surface irregularities on intensity data from laser scanning: an experimental approach*, Annals of Geophysics, Vol. 51, No. 5/6, Roma 2008.
- [6] Voegtle T., Schwab I., Landes T., *Influence of different materials on the measurements of terrestrial laser scanner*, The International Archives of the Photogrammetry, Remote Sensing and Spatial Information Sciences, Vol. 37, Part B5, 2008.

- [7] Soudarisanane S., van Ree J., Bucksch A., Lindenberg R., *Error budget of terrestrial laser scanning: influence of the incidence angle on the scan quality*, Proceedings 3DNordOst, Berlin 2007.
- [8] Żaczek-Peplińska J., Falaciński D., *Evaluation of possibilities to apply laser scanning for assessment of conditions of concrete*, Reports on geodesy, No. 1, Warszawa 2011, 537-544.
- [9] Richards J.A., *Remote Sensing Digital Image Analysis*, Springer-Verlag, Berlin 1993.
- [10] Ott, L., Larson R.F., Mendenhall W., *Statistics: A Tool for the Social Sciences*, Duxbury Press, Boston 1983.
- [11] Rosenfield, G.H., Fitzpatric-Lins K., *A Coefficient of Agreement as a Measure of Thematic Classification Accuracy*, Photogrammetric Engineering and Remote Sensing, 52, 1986, 223-227
- [12] Carstensen, L.W., *A Measure of Similarity for Cellular Maps*, The American Cartographer, 14, 1987, 345-358.

BOGUSŁAW ZAJĄC*

THERMAL ASPECTS OF FILLING GAPS AND LOSS IN CONCRETE PAVEMENT REPAIR

ASPEKT TERMICZNY WYPEŁNIANIA SZCZELIN I UBYTKÓW PRZY NAPRAWIE NAWIERZCHNI BETONOWYCH

Abstract

The paper summarizes the thermal aspect of bonding between engineering materials of different coefficients of thermal expansion. In such connections, there are thermal stresses generated. They may cause relevant decay of the mechanical properties of the bond under normal service temperatures. The experimental results show relevant influence of the temperature on bond performance, especially on durability of bonding in relation to the work under elevated variable temperature. The right selection of materials allows for increasing durability of connections. Mechanical properties of polyurethanes are stable in a wide temperature range over their glass transition temperature (occurring below -30°C), in opposite to epoxy resins, which glass transition temperature can be located in the range of environmental temperatures.

Keywords: durability, bonding, elevated temperature, adhesive layer

Streszczenie

W pracy przedstawiono zagadnienia połączeń materiałów konstrukcyjnych o różnych współczynnikach rozszerzalności termicznej. W przypadku takich połączeń generowane są naprężenia termiczne. Mogą one spowodować istotne zmiany właściwości mechanicznych połączenia w normalnych temperaturach pracy. Wyniki doświadczalne wykazują istotny wpływ temperatury na wytrzymałość połączenia, zwłaszcza w aspekcie jego pracy w zmiennych temperaturach. Odpowiedni dobór materiałów, pozwala na zwiększenie trwałości połączenia. Właściwości mechaniczne poliuretanów są stabilne w szerokim zakresie temperatur powyżej ich temperatury szklenia (występującej poniżej -30°C), co jest w opozycji do żywic epoksydowych, których temperatura szklenia może występować w zakresie temperatur środowiskowych

Słowa kluczowe: trwałość, klejenie, podwyższona temperatura, warstwa kleju

* Ph.D. Bogusław Zajęc, Institute of Structural Mechanics, Faculty of Civil Engineering, Cracow University of Technology.

Symbols

- Φ – diameter
- A – surface area
- l – length
- T – temperature
- T_g – glass transition temperature
- ρ – density
- α – thermal expansion coefficient
- σ – normal stress
- E – Young's modulus
- G – shear modulus

1. Introduction

Knowledge about the decrease of mechanical properties of bonding interface at elevated temperature is very limited and leads someone for better understanding, especially in the aspect of long term durability [1]. Epoxy resins, which are usually implemented in civil engineering constructions, change their mechanical properties above a glass transition temperature T_g , changing from a rigid material to a rubber like material. It was investigated by Leone et al. [2]. For epoxy adhesives, the shear stress distribution along the whole bond length represents exponential character with quick decaying. The effective bond length is

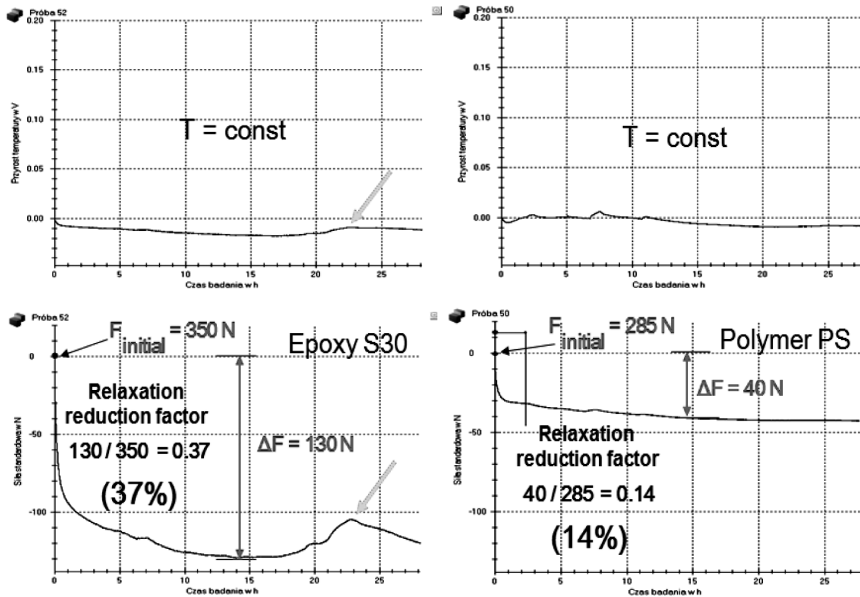


Fig. 1. Dynamic mechanical analysis (DMA) results obtained at the excitation frequency of 1 Hz for polyurethane PM – after [5]

also relatively low in the case of barely deformable and stiff interface materials [3]. In such cases, the bonding system is not fully exploited because of a low deformability interface. The same rules are also present for adhesives used in metal structures [4].

Epoxy resins, commonly using in strengthening systems, have limited exploitation temperature [5], because of their glass transition temperature (mostly $T_g = 35\div 70^\circ\text{C}$), thus covering fire protection is need. On the other hand, polyurethanes are almost stable at elevated temperatures up to 100°C (Fig. 1) [6], because their glass transition temperature is below the normal exploitation temperature range, thus allow for obtaining of better results in practical applications of civil engineering [7].

Advantageous mechanical properties of polyurethanes are due to their slightly larger ultimate deformations and the ability for decreasing of stress concentrations. The Flexible Joint Method, developed at the Cracow University of Technology, is based on polyurethane polymers using as adhesives layers in bonding of different engineering materials and FRP composites to concrete and masonry substrates [8].

Thermal stresses in a boundary area are depended on the coefficients of thermal expansion (CTE) and the Young modulus of an adhesive and of bonded materials. For materials with high value of Young's modulus, the change of a service temperature generates the significant stress increase and the cyclical circadian period has a great influence on durability of bonding. The knowledge of all parameters influencing the mechanical behaviour at the interface between different materials allows for an efficient numerical analysis [9] and designing [10].

2. Experimental

2.1. Measurement of the linear coefficient of thermal expansion

The coefficient of thermal expansion (CTE) was measured on cylindrical specimens of the diameter $\Phi = 28$ mm and the total length $L = 120$ mm. They were tested in a thermal chamber under stable temperature levels: room temperature (23°C), 40°C , 60°C , 80°C and 100°C for the period required to reach the stabilised elongation value ΔL . A displacement was measured using a WA-20 HBM Inductive Standard Displacement Transducer connected to a digital bridge QUANTUM MX840. The voltage temperature sensor was also connected to the bridge. The WA-20 transducer generated on sample the additional force equal $F = 1,2$ [N]. Coefficients of thermal expansion determined during the test for different materials are presented in Table 1 with their characteristics.

Table 1

Basic mechanical properties of presented polyurethanes determined during laboratory static tests at room temperature, according to ISO 527-1 [11]

Material	Young's modulus [MPa]	Tensile strength [MPa]	Elongation [%]	Coefficient of thermal expansion (CTE) [$10^{-6}/^\circ\text{C}$]
EPOXY S30	12800	28	0,22	30
PT	600	18	10	130
PS	8	2,2	45	158

Material	Young's modulus [MPa]	Tensile strength [MPa]	Elongation [%]	Coefficient of thermal expansion (CTE) [$10^{-6}/^{\circ}\text{C}$]
PST	6	2.5	110	140
PM	4	1.4	140	150
PSM	2.5	1.6	150	169

2.2. Measurement of basic mechanical properties

Basic mechanical properties in tension and compression were measured at room temperature according to EN ISO 527-1 [11], using an universal testing machine ZWICK 1455 and a digital extensometer. The obtained results for the tested materials are presented in Table 1.

2.3. Measurement in the absence of the deformation possibility

The basic experiment carried out for epoxy and polymer PS cylindrical samples, with the diameter of $\Phi = 28$ mm and the total length $L = 120$ mm, consisted of two parts. The first one was performed at the constant room temperature (23°C) with the constant initial load of 350 N for epoxy and of 285 N for polymer PS, generated by the universal testing machine. During the test, the traverse position was locked and relaxation was measuring for 28 hours. The obtained results are presented in Fig. 2.

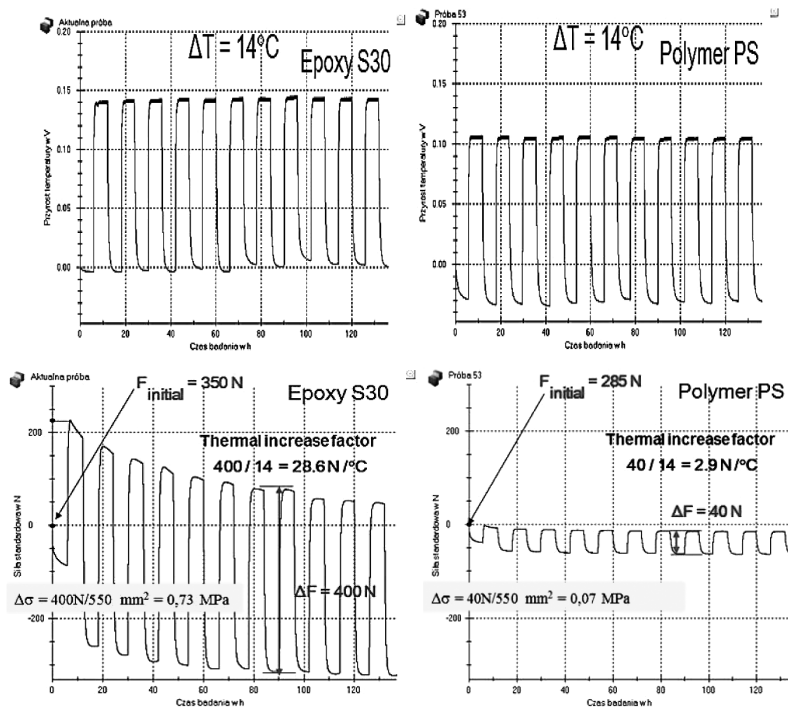


Fig. 2. The behavior of the material in the gap with the absence of the possibility of deformation

The great amount of the relaxation force decrease was observed during the first hour and then was started to be stable. After 15 hours, the drop of force for epoxy was 130 N (37% of the initial value) and for polymer PS was 40 N (14% of initial value). The epoxy material sample was very sensitive to temperature changes. It was observed during the test that a slight increase of the room temperature generated increase of the stress in the specimen (green arrow in Fig. 2).

The second part of the experiment was developed in the temperature chamber. The specimens of the same size (like in the first part) were investigated in the same way as previously – the constant initial load of 350 N for epoxy and 285 N for polymer PS and with the locked testing machine position. The samples were alternately heated and cooled in cycles of temperature level changing from room temperature (23°C) to 37°C (increase of $\Delta T = 14^\circ\text{C}$). The duration of each cycle was six hours and the whole test was 130 hours. Changes of temperature and of the force generated by the thermally working epoxy and polymer PS specimens are presented in Fig. 3.

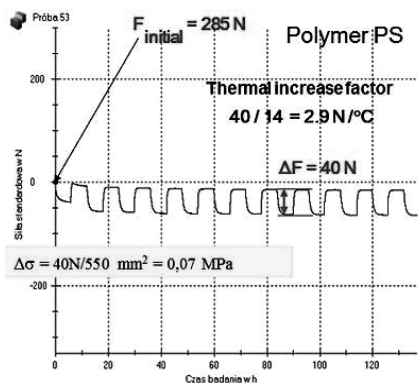


Fig. 3. Change of the force generated by temperature cycles: $\Delta T = 14^\circ\text{C}$; in 6 hours intervals with blocking of the specimen thermal elongation

The presented results indicate that epoxy resin generates 10 times higher level of the force (and stress in a real structure) than polymer PS under changes of temperature. The level of the additional stress forced by epoxy under the temperature increase of $\Delta T = 14^\circ\text{C}$ is equal to 0.73 MPa. It is a quite huge value in comparison to the tensile strength of the low strength concrete ($f_{\text{ctk},0.05} = 1.3 \text{ MPa}$ for C16/20) especially, when the temperature increase is double (the real temperature increase value in winter-summer season cycles). Such material, filling gaps (cracks) in a concrete structure, can cause additional damages initiated by thermal stress. On the other hand, polymer PS applied in a cracked structure will not generate such dangerous level of thermal stress. It has to be mentioned that the specimens of the cylindrical shape were constrained only in the direction of the uniaxial test with possibility of free deformation around cylinders. It is not typical for the real application, thus the obtained stress level is lower than expected in real cracks, where filling material is constrained around its volume.

2.4. Thermal stress factor

The thermal stress factor described by equation 1 is a measure allowing compared deformation of various materials under temperature changes, which is especially important in the case of a stiff bond joining different engineering materials. Temperature changes are responsible for the formation of thermal stress and they have a great influence for durability of the bond of materials of different CTE for long time period. Such effect is important not only in the situation of filling gaps (cracks) but also for the surface repair, where covering of old structure with new repair material exist. A better way of bonding in such conditions is using materials with similar CTE for stiff connections or using the highly deformable material (e.g. polyurethanes), generating low thermal stress as the interface between joined materials of the different thermal behaviour. The highly deformable material will compensate difference in elongation of materials with different CTE in bonding area and will not generate high amount of thermal stress.

$$E\alpha = \frac{\Delta\sigma}{\Delta T} \quad (1)$$

where:

- E – Young's modulus [N/mm²],
- α – thermal expansion coefficient [1/°C],
- $\Delta\sigma$ – change of stress [N/mm²],
- ΔT – change of temperature [°C].

Comparison of crucial parameters for two epoxy resins and five polyurethanes is presented in Fig. 4 and Fig. 5. The thermal stress factor is an indicator of the thermal stress level, which can be used in the choosing of proper material for the interface construction.

The polymer PS has a very low thermal stress factor in comparison to other engineering materials, as described in Fig. 6. Materials of the high Young's modulus have significantly higher value of the thermal stress factor in comparison to polyurethanes. They can generate the high level of thermal stress in a bond under normal exploitation temperatures. The calculated thermal stress values, for the increase of the service temperature of about 30°C, are presented in Fig. 7, using the thermal stress factors from Fig. 6. It is obvious that lack of free deformation possibility generates quite huge level of thermal stress in stiff materials.

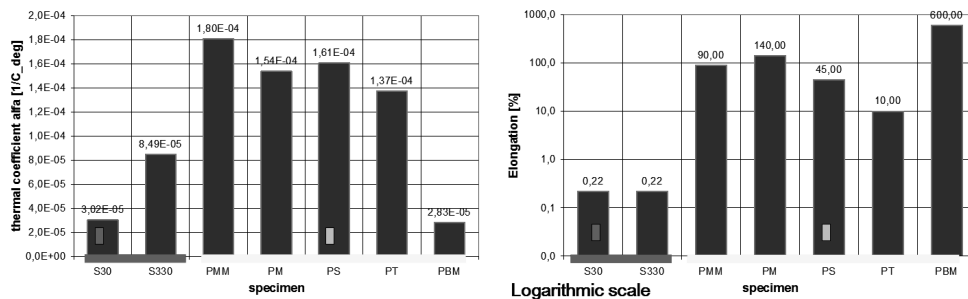


Fig. 4. Comparison of thermal coefficients of expansion and ultimate elongations of epoxy resins and polyurethanes (in logarithmic scale)

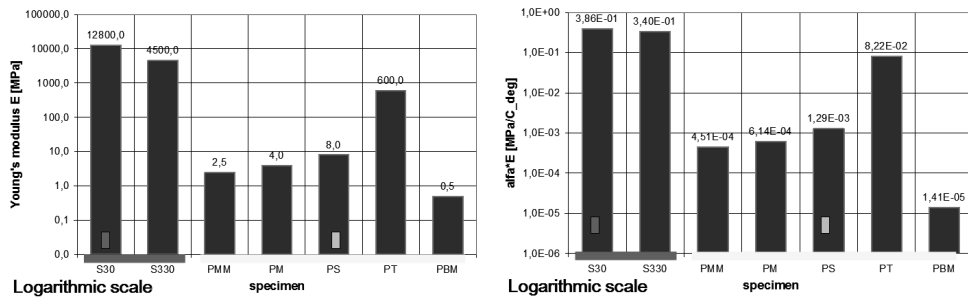


Fig. 5. Comparison of stiffness module (E) and thermal stress factors ($E \cdot \alpha$) of epoxy resins and polyurethanes (in logarithmic scale)

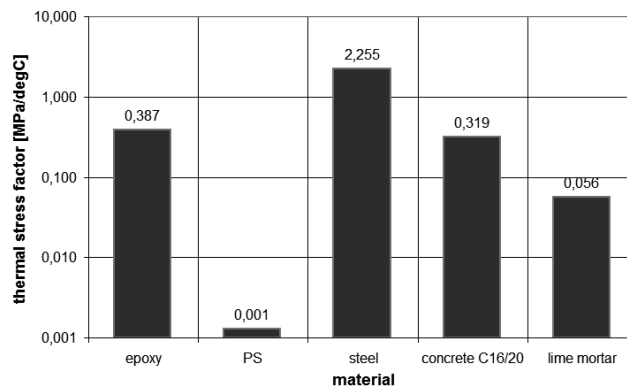


Fig. 6. Distribution of the thermal stress factor ($E \cdot \alpha$) per 1°C in logarithmic scale

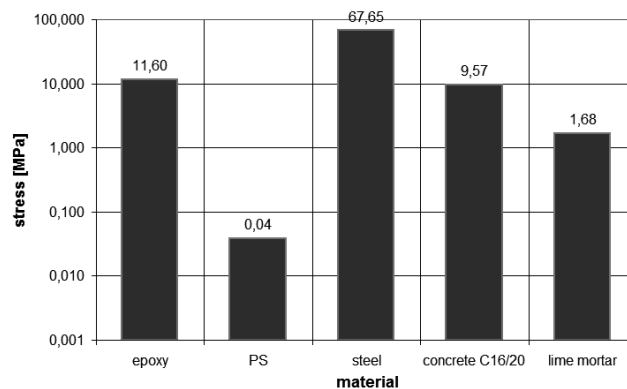


Fig. 7. Thermal stress ($\Delta \sigma$) calculated for 30°C change in logarithmic scale

In real applications, the most important aspect is the difference in stress between joined materials, responsible for the generating of shear stress in the interface.

For a stiff connection between an old concrete (e.g. C16/20) and a repair epoxy cover (e.g. S30), the calculated difference in stress is about 2 MPa under the temperature increase of 30°C (Fig. 7). Such high level of stress is responsible for the detachment of epoxy cover, observed in an engineering practice. A typical failure mode is cohesive detachment in concrete. It is also caused by the influence of low deformability of the joined materials (the ultimate elongation of concrete is about 0.2% and of epoxy is up to 2%). If the polymer PS is applied as a filament of gaps or a cover of concrete, it does not generate the high stress level and additionally its high deformability (the ultimate elongation of polymer PS is about 45%) protects such flexible cover against detachment. This aspect is also advantage in the case of the long time durability behaviour.

3. Conclusions

The study showed that:

- the epoxy resin S30 has the coefficient of thermal expansion of about 3 times higher than concrete, while polymer PS has it about 15 times higher;
- at the service temperature range of $-20\div 70^{\circ}\text{C}$, polyurethanes operate above their glass transition temperature, while epoxy resins operate generally below their glass transition temperature, but they may achieve this temperature even in the temperature range of $35\div 65^{\circ}\text{C}$;
- the relaxation value of the epoxy resin S30 is more than twice of the polyurethane PS;
- the change in temperature results in higher stress magnitude in the case of the epoxy S30 than in the case of the polymer PS;
- for the thermal analysis, it is essential to fill a crack with the material of the low thermal stress factor, expressed by the Young's modulus multiplied by the coefficient of thermal elongation ($E\alpha$);
- the epoxy S30 has the thermal stress factor 300 times higher than the polymer PS;
- repairing cracked structure subjected to a large temperature gradient, it is more appropriate to use the polymer PS as it generates lower stress than the epoxy S30;
- applying of the flexible bonding is more advantageous than the stiff one, if a structure is subjected to thermal influences;

Symbols: **PS, PT, PM, PSM, PST** (and others, not mentioned in this paper) are names of two component polyurethanes applied in the Flexible Joint Method, developed in the Institute of Structural Mechanics of the Cracow University of Technology. Various applied in civil engineering technologies based on the Flexible Joint Method are protected by patents PL207028 (B1), PL214295 (B1) and PL215827 (B1).

References

- [1] Valluzzi M.R., Oliveira D., Caratelli A., Castori G., Corradi M., de Felice G., Garbin E., Garcia D., Garmendia L., Grande E., Ianniruberto U., Kwiecień A., Leone M., Lignola

- G.P., Lourenço P.B., Malena M., Micelli F., Panizza M., Papanicolaou C.G., Prota A., Sacco E., Triantafyllou T.C., Viskovic A., Zając B., Zuccarino G., *Round Robin Test for Composite-To-Brick Shear Bond Characterization*. Materials and Structures, 45 (2012), 1761-1791.
- [2] Leone M., Matthys S., Aiello M.A., *Effect of elevated service temperature on bond between FRP EBR systems and concrete*, Elsevier, Composites: Part B 40, 2009, 85-93.
- [3] Fitton M.D., Broughton J.G., *Variable modulus adhesives: an approach to optimized joint performance*, Int. Journal of Adhesion and Adhesives 25, 2005, 329-336
- [4] Piekarczyk M., *Zastosowanie technologii klejenia w metalowych konstrukcjach budowlanych*, Wydawnictwo Politechniki Krakowskiej, Kraków 2013.
- [5] Klamer E.L., Hordijk D.A., Kleinman C.S., *Debonding of CFRP laminates externally bonded to concrete specimens at low and high temperatures*, Third International Conference on FRP Composites in Civil Engineering (CICE 2006), Miami 2006, Florida, USA.
- [6] Falborski T., Kwiecień A., Strankowski M., Piszczyk Ł., Jankowski R., *The influence of temperature on properties of the polymer flexible joint used for strengthening historical masonries*, Structural Analysis of Historical Constrictions, Jerzy Jasieńko (ed.), DWE, Wrocław 2012, 816-822.
- [7] Kwiecień A., *Polimerowe złącza podatne w konstrukcjach murowych i betonowych*, Monografia nr 414, Wydawnictwo Politechniki Krakowskiej, Seria Inżynieria Lądowa, ISSN 0860-097X, Kraków 2012.
- [8] Kwiecień A., *Praca kotew stalowych wklejonych w mur zabytkowy na sztywnych i podatnych warstwach adhezyjnych*, IX Konferencja Naukowo-Techniczna „Rew-Inż 2011”, Kraków 2011.
- [9] Truty A., *Szywność gruntów w zakresie małych odkształceń. Aspekty modelowania numerycznego*, Czasopismo Techniczne z. 20. Środowisko z. 3-Ś.
- [10] Grodecki M., Truty A., Urbański A.: *Modelowanie numeryczne ścianek szczelnych*, Kwartalnik AGH Górnictwo i Geoinżynieria, r. 27, z. 3-4, 2003, 297-303
- [11] EN ISO 527-1 (1993) *Plastics-determination of tensile properties-Part 1: General principles*.

JANINA ZACZEK-PEPLINSKA, PAWEŁ POPIELSKI*

UTILISATION OF TERRESTRIAL LASER SCANNING
FOR VERIFICATION OF GEOMETRY OF NUMERICAL
MODELS OF HYDROTECHNICAL STRUCTURES
USING THE EXAMPLE OF A SECTION
OF THE CONCRETE BESKO DAM

WYKORZYSTANIE NAZIEMNEGO SKANINGU
LASEROWEGO DO WERYFIKACJI GEOMETRII
NUMERYCZNYCH MODELI OBIEKTÓW
HYDROTECHNICZNYCH NA PRZYKŁADZIE SEKCJI
ZAPORY BETONOWEJ BESKO

Abstract

The paper presents results of utilisation of terrestrial laser scanning for verification of geometry of the numerical model of behaviour of Besko Dam, created on the basis of design data. Results of inventory measurements, performed in the period 2009–2011 with the use of laser scanning techniques are also presented. Changes in geometry of numerical models were introduced on the basis of performed measurements. Analysis, which aimed at determination whether the observed changes in shape influence the forecasting of behaviour of the structure. It has been stated that the applied technology of measurements is a useful tool for verification the model geometry, and, therefore, for checking the model correctness and increasing the reliability of obtained results.

Keywords:

Streszczenie

W pracy przedstawiono wyniki wykorzystania naziemnego skaningu laserowego do weryfikacji geometrii numerycznych modeli zapory betonowej. Porównano geometrię modelu numerycznego zachowania zapory Besko wykonanego na podstawie danych projektowych oraz wyniki przeprowadzonych w latach 2009–2011 pomiarów inwentaryzacyjnych z użyciem techniki skanowania laserowego. Na podstawie wykonanych pomiarów wykonano zmiany w geometrii modeli numerycznych i analizowano czy zaobserwowane zmiany kształtu mają istotny wpływ na prognozowane zachowanie się budowli. Stwierdzono, że wykorzystana technologia pomiaru jest dobrym narzędziem do weryfikacji geometrii modelu, a co za tym idzie, kontroli poprawności jego wykonania i zwiększeniu zaufania do otrzymanych wyników obliczeń.

Słowa kluczowe:

* Ph.D. Janina Zaczek-Peplinska, Ph.D. Paweł Popielski, Faculty of Geodesy and Cartography, Warsaw University of Technology, Department of Engineering Geodesy and Topographic Surveys.

1. Introduction

In order to determine displacements of the designed or existing hydrotechnical structure numerical calculations based on the FEM method are often applied [6]. The method assumed for calculations should model, to the required extent, real processes which considerably influence the final result; it should also allow for utilisation of the recent knowledge concerning processes of material parameter changes. Such a method should allow for modelling various variants of construction of the structure, as well as for consideration of basic factors, which influence the analysed process (such as generation of initial tensions, modelling of stages of construction, variations in groundwater level and resulting changes in loads).

FEM allows for estimation of forces and displacements in the foundation and in the designed or existing structure. Depending on the structure geometry, variations in natural conditions and expected accuracy, numerical simulation may be performed using the 2D or the 3D model. Analysis of interactions between the structure and the ground foundation should accompany the entire investment cycle and the structure utilization.

Verification of the developed numerical model, based on measurements of displacements of the real structure, is the most important confirmation that an adequate model has been assumed, which restores the real timetable of implementation (assumption the correct loads) and material parameters. It serves for gaining experiences which improve procedures of verification of material parameters (small deformations range) or modification of parameters determined for another range of deformations. Following the authors' opinion, abandonment of the model verification when measurements of displacements are accessible, should be considered as malpractice. If the model verification concerning the compliance between calculated and real displacements does not allow for confirmation the correctness of values of internal forces which were assumed for the structure dimensioning. As the authors suggest, results of calculations should be the basis for formulating conditions of implementation of the structure monitoring, including the determination of expected values of displacements in particular stages of construction, as well as permissible deviations, considered as alert values. This is extremely important in the course of implementation and exploitation of hydrotechnical structures.

2. Terrestrial laser scanning

Difficult field conditions, which usually occur in places where dams are located, determine the selection of specialised equipment and appropriate technique of surveys. The advantage of the modern technology, such as terrestrial laser scanning, is the possibility to perform many observations in a short time, what, together with the simplicity of maintenance, allows for decreasing the number of a surveying team members. Close proximity of water results in occurrence of local microclimatic conditions, which not always support implementation of observations with the expected accuracy.

Scanners may be divided into phase and pulse devices. The range of measurements is closely related with this division: phase solutions are dedicated for short distances (at present up to 200 m), whilst pulse devices allow for measuring structures located further from the measuring station (even up to several kilometres). Depending on the measuring

distance, close-, medium- and far- range scanners are distinguished. This results in the next characteristic feature, i.e. the measurement accuracy. Depending on the mode of distance measurements (phase or pulse) and the instrument type and model, the accuracy falls within the range between several millimetres and more than ten centimetres.

It is difficult to determine the accuracy of laser scanning since it is influenced, among others, by the following factors:

- distance between scanned objects and the scanner,
- atmospheric conditions,
- accuracy of determination of tie points for particular scans,
- accuracy of connection with the external co-ordinate system,
- angle of incidence of the laser beam onto the surface,
- type and colour of the reflecting surface,
- wavelength,
- object geometry, which may result in the multipath effect,
- ambient illumination,
- instrumental errors.

The final effect of laser scanning are not co-ordinates of specified points, but the geometric model, matched with the obtained cloud of points. Position errors of particular points vary and they include:

- errors in the scanning system (errors in determination of angles),
- distance errors,
- calibration errors.

The final object geometry is created with the use of an algorithm, which is based on the least square method. This results in the accuracy which may be several times higher than in the case of individual measurements and which depends on the appropriate density of measuring on the success of the scanned object.

Resolution is one of the parameters which influence the accuracy. The angular and distance resolution is distinguished. The angular resolution is the ability of the scanner to distinguish two objects, which are located in adjacent measuring directions. It depends on the scanning density and the size of the laser footprint; it decreases together with the increase of the distance between the instrument and the measured object. The scanning density is defined as the distance between two neighbouring, measured points. The higher it is, the higher is also the accuracy of projection of shapes of scanned objects. The size of the laser footprint also influence the measuring accuracy, what may be particularly visible at the edges of scanned objects. The laser beam, when it reaches the edge of the object is partially reflected from its surface; other parts of the beam are reflected by a part of a neighbouring surface or by another object. As a result points which create the discussed edge, will have the incorrectly calculated co-ordinates – it is, so-called, “the edge effect” [4].

With respect to hydrotechnical structures, laser scanning may be applied in such tasks, as [Zaczek-Peplinska, Adamek, Popielski, 2009]:

- the structure inventory – the structure inventory at particular stages of implementation (comparison of constructed elements with the design), post-completion inventory, inventory after overhauls, periodical measurements in the period of exploitation,
- verification of relations existing between variations in water level in the reservoir and variations of the structure geometry,
- evaluation of the structure technical conditions.

The basic limitation concerning utilisation of laser scanning is the high price of devices, which should be increased by the costs of maintenance and adjustment. In the future, the price decrease together with the increase of popularity of laser scanning may be expected due to the increase of the number of scanners available on the market. Probably the technological development will result in widening of the scope of its applications.

3. Geometry of the dam – numerical model versus scanning results

One of the most important elements of the process of creation of the numerical model of behaviour of an engineering structure is the correct projection of its shape. Forecasting its operations, displacements and possible breakdowns and catastrophes is important due to security reasons; this particularly concerns water dams. In the case when spatial information is acquired for a structure of uncomplicated construction, successful utilisation of measurements performed by means of an electronic tacheometer is possible. However, in the case of higher complexity and volumes, such measurements could turn to be too labour-intensive and ineffective. Costs of such measurements and the necessity to involve a several-member team are also the reasons that utilisation of terrestrial laser scanning turns to be much more efficient.

Measurements performed with the use of a laser scanner may be used not only at the stage of the model development, but also in order to verify the model correctness or timeliness.

The usefulness of application of laser scanning results for verification of the geometry of numerical models of behaviour was evaluated on the basis of experimental measurements of the Besko Dam; they were performed on 8–9 June, 2009 by the team of specialists from the Faculty of Geodesy and Cartography of the Warsaw University of Technology (Department of Engineering Geodesy and Topographic Surveys) and Leica Geosystems Polska. Measurements were performed with the use of the Leica ScanStation 2 scanner (Fig. 1a), results of measurements of the Besko Dam are presented in Fig. 1b.



Fig. 1. Measurements of the Besko Dam. a) Leica Scanstation 2 scanner during surveys, b) results of surveys of the dam from the downstream face – results of combination of 5 clouds (about 155 million points)

The geometry of the numerical model [1, 2] of the concrete structure was developed on the basis of intersections originating from the archived design documentation. After completion of the construction of the dam results of post-completion inventory were not attached to the documentation of the post-completion approval and they are not available at the moment. The numerical model considers positions of internal galleries (Fig. 2a) and location of view-finders and benchmarks used for the surveying control of the dam. Using the available software tools the grid of finite elements was generated (Fig. 2b). The controlled points (vie-finders, benchmarks, points of the fixed straight line) correspond to the nodes of the FEM grid. Numerical analyses for the structures de-scribed below were done using the HYDRO-GEO software which is now under development at the Warsaw University of Technology. On the account of the available material parameters, the elastic-plastic soil model was adopted on the basis of the Coulomb-Mohr plasticity criterion. The calculations were performed as a two dimensional task in the plain state of strain. The model was digitized using six-node isoparametric triangular elements of second-order shape function. The analysis was done in the so-called effective stresses. The total number of elements equals to 1213 and the number of nodes – 2566.

The model developed in this way, which considers the dam geometry (developed on the basis of archived documentation) was divided into elements and then it was amended with material parameters and initial, boundary conditions (such as initial tensions and water levels in the reservoir).

The model of the segment 9 of Besko Dam was used for the further elaboration.

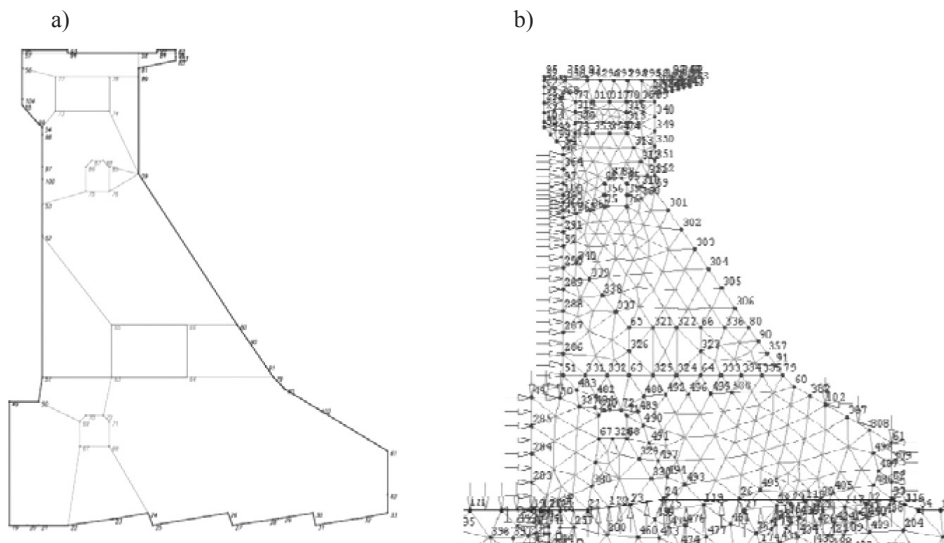


Fig. 2 a) geometry of the section of the dam, assumed for the model (without the background),
b) a fragment of a grid of nodes

Acquisition of measuring data by means of laser scanning is extremely fast and it is performed almost automatically. There is no need to orientate the scanner or to set it over particular, fixed points of the measuring network. However, conventional measurements cover the points which serve for connection and georeference the scans. Therefore, the accuracy of the model obtained from the cloud of points does not depend on technical functionality of

a scanning device only, but also on the measurement accuracy and processing of the results of measuring the angular-linear network. The next stage, which influences the accuracy of the final product, is registration (connection) of scanned points and transformation of those points to the common co-ordinate system. The last stages of data processing were performed using the Leica Cyclone 7.0 software package.

Clouds of points, obtained from measurements of the Besko Dam were connected in the process of registration, basing on fixed points of the control geodetic network of the structure. Besides registration of all five clouds of points, they were also georeferenced. The accuracy of performed transformation (the mean absolute error) was equal to 0.003 m. Finally, more than 155 million points were obtained in the common, local co-ordinate system.

4. Verification of the geometric model

A two-dimensional intersection of the segment 9 was analysed in the process of verification of geometry of the numerical model of the Besko Dam. The Leica Cyclone software package allows for creation of intersections of the cloud of points. It is performed by locating the cutting plane (cutplane) in an arbitrary location and setting its thickness (Set Slice Thickness). Before creating verifying intersections, the registered cloud of points was reduced by the function Edit Object → Reduce Point Cloud, what resulted in the number of points decreased to 25%. For the analysed section 3 intersections were created – in the centre and at the edges; then they were averaged (Fig. 3), the width of cutting was equal to 0.10 m.

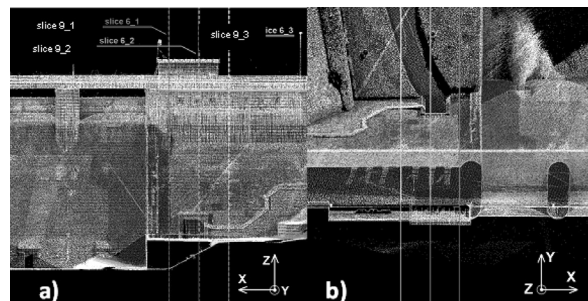


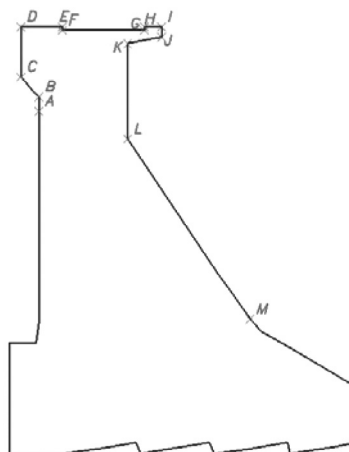
Fig. 3. Location of performed intersections: a) view from the downstream face, b) view from the top

As a result, 3 two-dimensional clouds of points were obtained, which presented the intersections – from the downstream face to the ground level and from the upstream face to the water mirror level, covering the crown – which described the external shape of the dam outline.

In order to verify the geometry applied for creation of the numerical model of the behaviour of the dam, the best fitting straight lines should be matched with points obtained as a result of the intersection. The number of those lines was assumed in accordance with the outline presented in Fig. 2a.

Matching was performed using the least square method for each of three intersections. 12 straight lines were matched into each intersection; their crossings pointed to location of corner points of a figure which described the shape of the intersection of the segment 9 (Fig. 4).

Fig. 4. Characteristic points of geometry of the segment 9 of the dam



In order to achieve the most representative shape for the entire section of the dam, co-ordinates of characteristic points, obtained from three intersections, were averaged. Table 1 presents co-ordinates of the common points and their differences.

Table 1

Coordinates of common points and their differences

Archived model			Averaged intersection			Difference		Distance between points [m]
Nr	X [m]	Y [m]	Nr	X [m]	Y [m]	dX [m]	dY [m]	
A	97.852	18.000	A	98.270	18.000	0.418	0.000	0.418
54	97.852	18.900	B	98.295	19.778	0.443	0.878	0.984
55	96.152	20.700	C	97.005	20.967	0.853	0.267	0.894
95	96.152	25.200	D	97.081	25.398	0.929	0.198	0.950
93	100.002	25.200	E	100.259	25.334	0.257	0.134	0.290
94	100.002	24.900	F	100.373	25.220	0.371	0.320	0.490
84	107.622	24.900	G	107.339	25.215	-0.283	0.315	0.423
92	107.622	25.200	H	107.445	25.322	-0.177	0.122	0.215
82	109.202	25.200	I	108.854	25.366	-0.348	0.166	0.385
83	109.202	24.300	J	108.828	24.274	-0.374	-0.026	0.375
81	106.052	23.700	K	105.950	23.777	-0.102	0.077	0.128
59	106.052	15.130	L	106.052	15.130	0.000	0.000	0.000
M	117.294	-1.000	M	117.436	-1.000	0.142	0.000	0.142
A'	97.852	-1.000	A'	98.003	-1.000	0.151	0.000	0.151

The calculated standard errors of position of points not still exceeded 2.5 mm (2.5 cm) having regard the following steps: measuring angles and distances (scanning), the registration of scans, the transformation to the local co-ordinate system of object model, approximation of characteristics straights which obtained from the intersection of clouds of points.

5. Correction of geometry of the numerical model

Changes concerning the shape of the modelled intersection of the dam were introduced according to three variants, with diversified methods of matching points into the scanned model, and, as a result, with differences in distribution of nodal points and small differences in the final geometry. In the variant I the intersection area was decreased by 1.2%, what resulted in the decrease of the volume of this segment of the dam and its mass – by approximately 208 tones. In the case of variants II and III this reduction equalled to 1.8%, i.e. approximately 309 tones, from the initial mass of the segment equalled to 17578 tones. The volume was calculated on the basis of the intersection area and the designed width of the segment 9. This paper discusses results for the variant III, for which the biggest corrections were introduced, comparing to the archived (the primary) model. Figure 5 presents visualisation of changes introduced to the model.

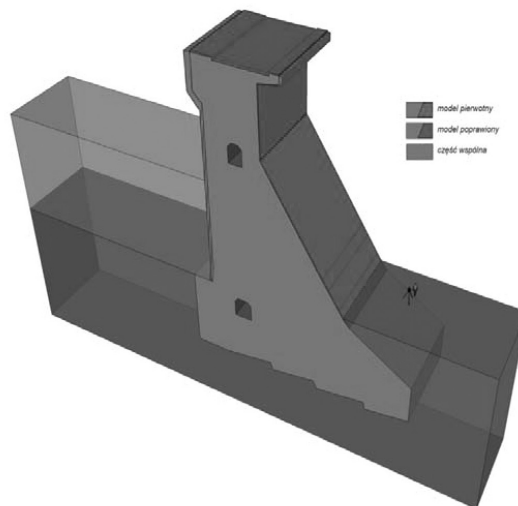


Fig. 5. Visualization of the segment 9 of the dam with differences between the model based on designed data and the model based on laser scanning results

Matching the nodal points to the new model of the intersection geometry consisted of shifting breaking points to new locations, determined on the basis of data from scanning; the node 59 corresponding to point *L* was assumed as the “fixing point”. It was justified by the best matching the shape of the downstream wall of both intersections. Nodes located between breaking points were projected on the straight lines, which created the intersections; proportional distances between them were maintained.

Corrected co-ordinates of points were reintroduced to the HYDRO-GEO package. Computations were performed similarly to computations performed for the archived model [Popielski, Zaczek-Peplinska 2007], i.e. in three stages: stage I – generation of initial stresses in the subsoil, stage II – modelling the dam construction (“the dry reservoir stage”), stage III introduction of loads resulting from filling the reservoir with water. Recalculation of the model was to answer the question whether performed correction of the geometry and reduction of the mass of the segment (Table 2) would result in considerable changes in displacements of selected nodes.

Table 2

Differences between the archived model and the corrected model

Variant	Area. [m²]	Difference	Difference [%]
Archived	647.3	–	–
Updated	635.9	11.4	1.8
	Volume [m³]	Difference	Difference [%]
Archived	7767.4	–	–
Updated	7631.0	136.4	1.8
	Mass [t]	Difference	Difference [%]
Archived	17578	–	–
updated	17269	309	1.8

6. Changes of displacements of common points as a result of introduced correction of the geometric model

Five points were selected to compare changes of displacements of nodal points. Two of them – points 89 and 90 – are the points, which locations are identical with the location of view finders, used for control surveys. Remaining three points: 301, 302 and 303 result from the division of the intersection into elements; for those points the highest increments of displacements per the dam height unit were stated for various upper water mirror levels [Zaczek-Peplinska, Popielski, 2008]. It was to allow for achieving the possibly biggest displacements and their differences.

For the stage III of computations the upper water mirror level was assumed as 336.99 m above the sea level. The level of 310.00 m above the sea was assumed on the downstream face as the ordinate of the water mirror level. Displacements resulting from changes in water level in the reservoir, for the archived and updated models were computed. Computed horizontal displacements of the models and their differences are presented in Table 3.

Horizontal displacements of the model and their differences with pointing to the maximum values

Horizontal displacements				
Point	Stage	Archived [m]	Corrected [m]	Differences [mm]
89	I	0.0000	0.0000	0.0
	II	-0.0032	-0.0029	-0.3
	III	0.0032	0.0039	-0.7
90	I	0.0000	0.0000	0.0
	II	-0.0006	-0.0005	-0.1
	III	0.0041	0.0043	-0.2
301	I	0.0000	0.0000	0.0
	II	-0.0019	-0.0017	-0.2
	III	0.0037	0.0041	-0.4
302	I	0.0000	0.0000	0.0
	II	-0.0017	-0.0015	-0.2
	III	0.0037	0.0041	-0.4
303	I	0.0000	0.0000	0.0
	II	-0.0015	-0.0013	-0.2
	III	0.0038	0.0042	-0.4

7. Final remarks

During the backward analysis, high differences (from surveying perspective) in the shapes of intersection of the segment 9, between the geometry of the archived model and the model obtained from laser scanning were observed. The computed difference of the mass between these models seems to be important. However, it should be considered that the model was created on the basis of the archived, primary design of the dam, which differs from the real conditions. The mass difference of the segment equalled to approximately 2% (309 tones), for the total mass of the segment equal to 17578 tones.

Differences in computed displacements of control nodes between the archived and updated model were close to 1mm in one case only, what is equal to 20% of the displacement forecasted for that node.

On the basis of performed research works, it may be stated that:

- The type and accuracy of the final product, obtained in the process of processing data from laser scanning are appropriate for verification and support of creation the geometry of numerical models of behaviour of building structures. The obtained differences between models are important – in the case of the mass of the structure, it corresponds to approximately 309 tones. The model created on the basis of archived materials may not correspond to the real shape of the structure.
- Measurements performed by means of the laser scanner are economically justified and require less involvement of an operator than in the case of utilisation of other methods, what results in limited risk of mistakes.
- Laser scanning may be successfully utilised for verification of models of behaviour, in particular in the case of structures of complicated shapes, or which are difficult for measurements with the use of conventional methods.
- Data acquired from laser scanning measurements better restore the real geometry of the measured objects. The obtained cloud of points may be the basis for further analyses, creation of three– and two-dimensional models, creation animated images and visualisation.
- The obtained results proved, that in the case of massive, concrete hydrotechnical structures and analyses of displacements caused variations in water level in the reservoir, the accuracy of determination of the dam geometry of 1% approximately, is sufficient.
- It should be analysed, how the measured differences in the dam geometry influence the computed values if displacements caused by thermal loads.

The authors acknowledge Mr. Adam Dąbrowski, M.Sc. Eng. and Mr. Dominik Oracki, M.Sc. Eng. for the basic processing of laser scanning results with the use of Leica Cyclone 7.0 software package and for preparation of some illustrations.

References

- [1] Dłużewski J., Gajewski T., Tomaszewicz A., Boros-Meinike D., *Resistance analysis of the concrete segment on order to detect possible damages and confirm the forecast of displacements using the example of the segment 8 of the Besko Dam*, IMGW OTKZ, Warszawa 1995.
- [2] Dłużewski J., Gajewski T., Tomaszewicz A., Boros-Meinike D., *Displacement and resistance analysis of the segment 8 of the Besko dam in order to interpret measured displacements*, IMGW OTKZ, Warszawa 1996.
- [3] Kaspar M., Pospisil J., Stroner M., Kremen T., Tejkal M., *Laser scanning in civil engineering and land surveying*, Hradec Kralove, Republika Czeska: Vega s.r.o., 2004.
- [4] Pawleta M., Igielska A., *Accuracy analysis of selected models of terrestrial scanners of Zoller_Frohlich GmbH*, Praca dyplomowa magisterska, Akademia Górniczo-Hutnicza, Kraków 2009.
- [5] Popielski P., Zaczek-Peplinska J., *Utilisation of numerical models in exploitation of dams*, Materiały XII Międzynarodowej Konferencji Technicznej Kontroli Zapór, Stare Jabłonki 2007, 241-255.
- [6] Zienkiewicz O.C, Taylor R.L., *The Finite Element Method. Fifth edition*, Butterworth-Heinemann 2000.

- [7] Zaczek-Peplinska J., Kubisz W., *Possibilities to utilise laser scanning for acquisition of data and verification of the numerical model of a dam*, materiały niepublikowane, Warszawa 2009.
- [8] Zaczek-Peplinska J., Popielski P., *Location of control points of a dam on the basis of modelled gradients of displacement increments*, rozdział w monografii: *Bezpieczeństwo zapór – bezpieczeństwo ludności i środowiska*, Instytut Meteorologii i Gospodarki Wodnej, Warszawa 2009.

CONTENTS

Chełmecki J., Kwiecień A., Zając B.: The inertance function in dynamic diagnosis of undamaged and damaged structures	3
Grodecki M.: Influence of a surcharge line load on cantilever sheet pile wall behavior	13
Iwanejko R.: Risk calendar as a supplement of a basic risk analysis in a water supply system	21
Kacprzak G., Kravchenko P., Smolak W.: Comparison of CPRF modeling studies results to theoretical ones in soil with a low bearing capacity	33
Kacprzak G., Stefański Ł., Pietrzykowski P., Transformational functions for displacement columns performed in cohesive low-bearing-capacity soils.....	43
Kanty P.: Research on the influence of the applied stone column formation method on the consolidation time of the surrounding soil	49
Kisiel P., Kwiecień A.: Numerical analysis of a polymer flexible joint in a tensile test	63
Mirosław-Świątek D., Merkel M., Giżyński W.: Application of the filtration numerical model for the assessment of the effectiveness cut off walls in levees.....	73
Popielski P., Kowalczyk S., Mieszkowski R., Chadaj M., Krysiak M., Smoliński B.: The application of geophysical methods and numerical modeling for the evaluation of embankment technical conditions.....	83
Puzdrowska M.: Application of numerical methods in the design and analysis of fish pass efficiency	99
Słowikowski D., Kacprzak G.: Implementation of low pressure injection for soil reinforcement and sealing – selected application	111
Sternik K.: Comparison of slope stability predictions by gravity increase and shear strength reduction methods	121
Toś C.: Supervised classification of laser scanning data in the assessment of technical conditions of masonry constructions	131
Zając B.: Thermal aspects of filling gaps and loss in concrete pavement repair.....	143
Zaczek-Peplinska J., Popielski P.: Utilisation of terrestrial laser scanning for verification of geometry of numerical models of hydrotechnical structures using the example of a section of the concrete Besko Dam.....	153

TREŚĆ

Chełmecki J., Kwiecień A., Zając B.: Funkcja inertancji w diagnostyce konstrukcji nieuszkodzonych i uszkodzonych	3
Grodecki M.: Wpływ obciążeń liniowych na pracę ścianki szczelnej niekotwionej ...	13
Iwanejko R.: Kalendarz ryzyka jako uzupełnienie podstawowych analiz uszkodzalności sieci wodociągowej	21
Kacprzak G., Kravchenko P., Smolak W.: Porównanie wyników badań modelowych fundamentu płytowo-palowego posadowionego na podłożu słabonośnym z wynikami teoretycznymi	33

Kacprzak G., Stefański Ł., Pietrzykowski P.: Funkcje transformacyjne dla kolumn przemieszczeniowych wykonywanych w spoistych gruntach słabonośnych	43
Kanty P.: Badania wpływu technologii formowania kolumny kamiennej na czas konsolidacji jej otoczenia	49
Kisiel P., Kwiecień A.: Analiza numeryczna polimerowych złączy podatnych poddanych rozciąganiu	63
Mirosław-Świątek D., Merkel M., Giżyński W.: Zastosowanie numerycznego modelu filtracji do oceny efektywności przesłon hydroizolacyjnych w wałach przeciwpowodziowych	73
Popielski P., Kowalczyk S., Mieszkowski R., Chadaj M., Krysiak M., Smoliński B.: Zastosowanie metod geofizycznych i modelowania numerycznego do oceny stanu technicznego wałów przeciwpowodziowych	83
Puzdrowska M.: Zastosowanie metod numerycznych w projektowaniu i analizie sprawności przepławki dla ryb	99
Słowikowski D., Kacprzak G.: Zastosowanie iniekcji niskociśnieniowej do wzmocnienia oraz uszczelnienia podłoża gruntowego – wybrana realizacja	111
Sternik K.: Porównanie prognoz stateczności skarpy metodami rosnącej grawitacji i redukcji wytrzymałości	121
Toś C.: Klasyfikacja nadzorowana danych skaningowych w ocenie stanu technicznego konstrukcji murowych	131
Zajac B.: Aspekt termiczny wypełniania szczelin i ubytków przy naprawie nawierzchni betonowych	143
Zaczek-Peplinska J., Popielski P.: Wykorzystanie naziemnego skaningu laserowego do weryfikacji geometrii numerycznych modeli obiektów hydrotechnicznych na przykładzie sekcji zapory betonowej Besko	153